




Review on high efficiency and high precision compliant polishing method

Huiming Feng¹ · Linbin Huang^{1,2} · Peizhi Huang^{1,2} · Jiaming Liu^{1,2} · Xiangbo He^{1,2} · Yunfeng Peng^{1,2} 

Received: 4 December 2023 / Accepted: 3 March 2024 / Published online: 1 April 2024
© The Author(s), under exclusive licence to Springer-Verlag London Ltd., part of Springer Nature 2024

Abstract

Complex precision components are integral to many sectors, straddling both military and civilian applications. These include aerospace telescopes, infrared thermal imaging systems, artificial intelligence, semiconductor chip lithography, medical imaging apparatus, and avant-garde communication technologies. These intricate precision components have become vital elements of the aforementioned optical systems, characterized by a wide range of extensive requirements totaling in the tens of millions. Within the realm of computer controlled optical surfacing (CCOS), high-efficiency bonnet polishing (BP) and high-precision magnetorheological finishing (MRF) are two compliant polishing methods with distinct advantages, extensively applied to ultra-precision machining of complex curved surface components. However, the bonnet polishing tool is prone to wear, the tool influence function is unstable, and the control process is complicated. The material removal efficiency of MRF is low; it easily introduces mid-spatial frequency (MSF) errors, and improving the performance of the magnetorheological fluid (MR fluid) is challenging. Therefore, summarizing these two techniques is essential to enhance the application of compliant polishing methods. The paper begins by examining the unique strengths of both technologies and then explores the potential for their integrated application. The paper then provides a detailed introduction to the origin, principles, equipment, and applications of BP. Next, the paper outlines the research progress of key technologies, including modeling of the tool influence function (TIF), management of MSF errors, and the wear of the bonnet tool within the realm of BP technology. Following that, the development history, technical principles, equipment, types, and compound methods of MRF are presented. Then, the research progress of several key technologies, such as modeling of TIF, controlling MSF error, and the preparation of MR fluid in the field of MRF technology, are reviewed. Lastly, the paper provides a summary and outlook for the two technologies, such as further in-depth study of the material removal mechanism and the suppression method of the edge effect in BP, a further in-depth study of methods to improve the material removal rate, and MSF error suppression methods in MRF.

Keywords Compliant polishing · Bonnet polishing · Magnetorheological finishing · Technological development · Complex components

1 Introduction

In recent years, the swift advancement of science and technology has led to the widespread application of optical components in various domains, as depicted in Fig. 1. These

applications include space telescopes, infrared thermal imaging, artificial intelligence, semiconductor chip production, medical imaging devices, cutting-edge communication technologies, and both military and civilian sectors, signifying an extensive upstream and downstream market size.

Surface accuracy and surface roughness are critical factors that prevent degradation in resolution, contrast, depth of field, and aberrations—thereby preserving the overall performance of an optical system. Low spatial frequency (LSF) errors contribute to imaging aberrations, while MSF errors can lead to small-angle scattering, flare, and reduced resolution, resulting in blurred images. High spatial frequency (HSF) errors, on the other hand, induce large-angle

✉ Yunfeng Peng
pengyf@xmu.edu.cn

¹ Department of Mechanical and Electrical Engineering, School of Aerospace Engineering, Xiamen University, Xiamen 361005, China

² Shenzhen Research Institute of Xiamen University, Shenzhen 518057, China

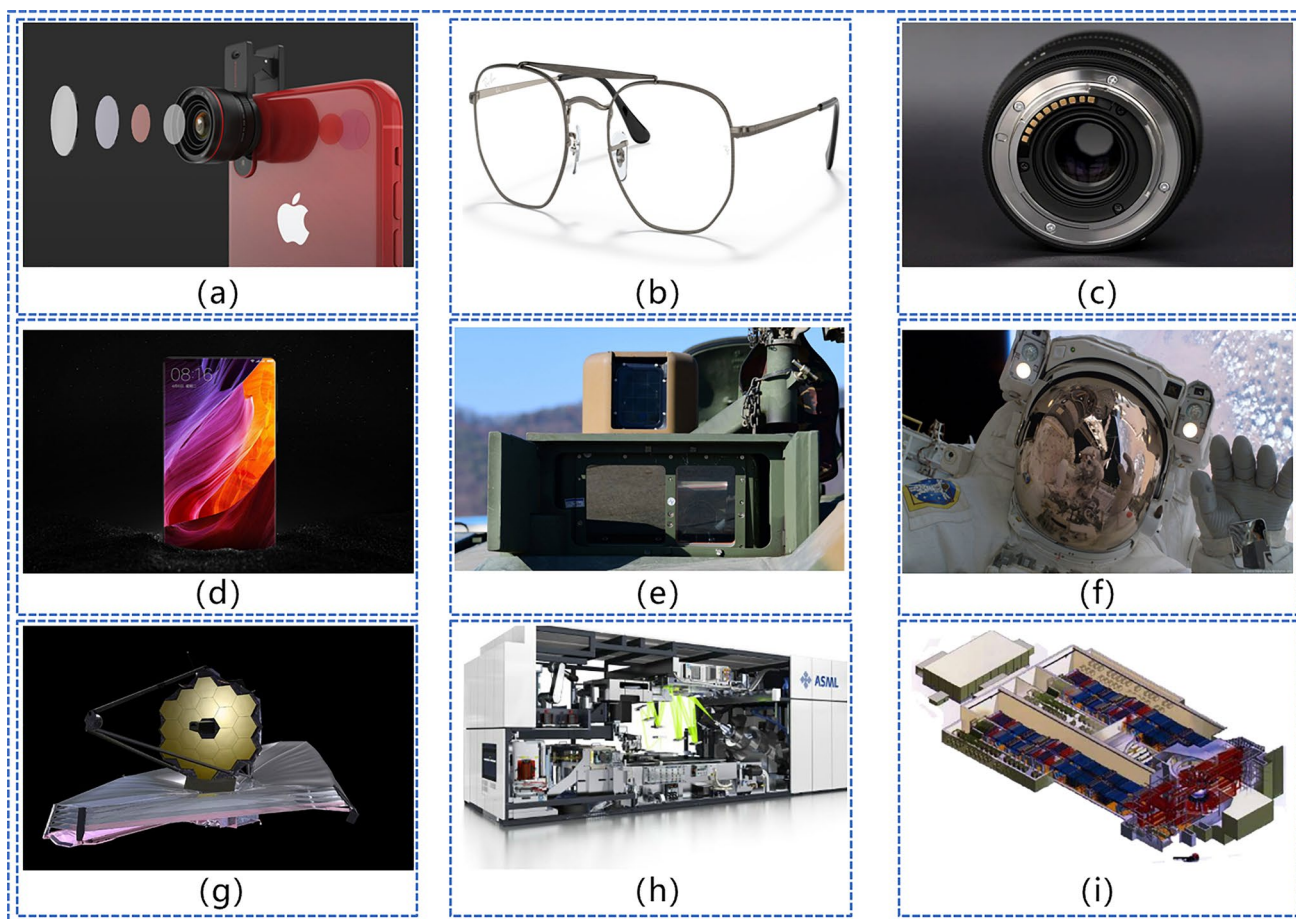


Fig. 1 Applications of optical components. **a** Cell phone lens. **b** Eyeglass lenses. **c** Camera lens. **d** Cell phone screen. **e** Ranging device for tanks. **f** Astronaut's helmet. **g** James Webb telescope. **h** NXE-3300 Extreme Ultraviolet Lithography. **i** US NIF laser fusion device

scattering and energy loss [1]. The optical manufacturing process imparts surface processing marks that form surface shape errors and causes subsurface damage (SSD) within the material, beneath the surface up to several tens of microns. Such damage, which is difficult to detect, directly compromises the component's service life, long-term stability, coating quality, imaging fidelity, and essential performance indicators like the laser damage threshold. Regarding the US National Ignition Fusion (NIF) project as a case study [2, 3], more than 30,000 optical components are required for its primary laser fusion device, including approximately 7360 large-aperture optics, such as windows, lenses, and large vessel plates [4, 5]. The mentioned components also include raster paths. China has launched the “Shengguang” series of laser fusion optical projects. The constructed Shengguang III high-power laser device necessitates the use of almost 10,000 ultra-high-precision optical components [6, 7]. The European Extremely Large Telescope (E-ELT) in Chile is equipped with a 39.3-m-diameter primary mirror, comprised of 798 hexagonal aspherical lenses [8, 9]. The James Webb Space Telescope (JWST) features a primary

mirror with a diagonal length of 6.5 m and is composed of 18 hexagonal submirrors, encompassing an area more than five times larger than that of the Hubble Space Telescope (HST) [10, 11]. The Twinscan NXE3100 extreme ultraviolet lithography system, developed by ASML, utilizes an off-axis six-mirror reflective structure, achieving a lithographic resolution of 27 nm [12, 13].

Currently, the predominant methods of computer-controlled optical surfacing (CCOS) include small tool polishing (STP) [14], stressed lap polishing (SLP) [15], magnetorheological finishing (MRF) [16], fluid jet polishing (FJP) [17], magnetorheological jet polishing (MJP) [18], ion beam figuring (IBF) [19], and bonnet polishing (BP) [20, 21]. Table 1 provides a systematic comparison of the primary technical characteristics of these mainstream CCOS technologies [20].

The table indicates that the mainstream subaperture flexible polishing machining techniques, BP and MRF, offer significant advantages. Despite their high machining surface accuracy and stable TIF, IBF and MJP have low material removal rates. In contrast, BP and MRF outperform in

Table 1 Comparison of the main features of the current mainstream CCOS polishing technologies [20]

	STP	SLP	IBF	MRF	FJP	MJP	BP
Large caliber adaptability	Good	Good	Average	Good	Mediocre	Mediocre	Very good
Aspheric adaptability	Poor	Better	Very good	Very good	Very good	Very good	Very good
Material removal efficiency	Low	Higher	Very low	Low	Low	Low	High
Accuracy of machined surfaces	Poor	Mediocre	Very good	Very good	Average	Very good	Good
Subsurface damage	Lot	Fewer	No	No	Very few	Few	Fewer
TIF stability	Mediocre	Mediocre	Very good	Very good	Average	Good	Better
Legacy of MSF	Few	Average	Average	Few	Average	Average	Few
Technical cost	Low	Higher	Very high	High	High	High	Average
Comprehensive evaluation	Average	good	Better	Very good	Better	Better	Excellent

all aspects and have greater commercial availability. The significant advantages of BP technology include precision processing, enhanced spatial accessibility, and an expanded processing range with a defined and controllable “Gaussian-like” TIF. The air pressure can be adjusted to alter the removal efficiency and surface quality of optical components. By adjusting the air pressure inside the bonnet, it is possible to adapt to different shapes of optical components and overcome the limitations of the STP and the challenges posed by curved surfaces [20–22]. The notable benefits of MRF technology can be attributed to the circulating renewable MR fluid that undergoes a phase change reaction under the influence of an external energy field. This characteristic ensures that the compliant ribbon never wears out, thereby maintaining the TIF stability. Furthermore, the compliant ribbon can be tailored to fit any curved optical surface, allowing for control of the edge TIF without introducing apparent subsurface damage [23–26].

In the existing literature reviews, Zhu et al. [27] systematically explicated the connotation of compliant polishing, discussing in detail the principles, methods, and material removal characteristics of four compliant polishing methods: BP, MRF, FJP, and IBF. However, they lacked a summation and generalization of several key technologies of the processes. Shen et al. [28] systematically introduced the principles, equipment, compound polishing methods, and applications of BP, MRF, etc., but lacked a systematic presentation of the key technologies. Wu et al. [29] summarized and generalized BP from the perspective of key technologies, but the literature they covered was limited and lacked a summary on the topic of wear of the bonnet tool, which is not comprehensive enough. Wang et al. [30] made a detailed summary and generalization on the basic aspects such as principles and tools, and key technologies like TIF and MR Fluid, but their reports still lacked a systematic and comprehensive coverage concerning the MRF field, particularly in controlling on MSF and polishing paths. Therefore, it is very necessary to systematically summarize the compliant polishing methods BP and MRF, as they possess irreplaceable

advantages and are very suitable for industrial production. This helps researchers to quickly understand and master the theoretical foundations and current research status of BP and MRF, and to explore research ideas further.

This paper first introduces the significant advantages of BP and MRF technologies and then presents the potential for their combined production. Next, the origin, principle, equipment, and application of BP are introduced in detail, followed by a discussion of advancements in key BP technologies. Following that, the development history, technical principle, equipment, types of MRF, and composite polishing methods of MRF are presented. Then, the advancements in several key technologies, for example, the modeling of TIF, error control in MSF, and MR fluid preparation in the field of MRF technology, are reviewed. Finally, the two technologies are forecasted and summarized. The subsequent focus of the BP and MRF was noted, such as the further in-depth study of the material removal mechanism and the suppression method of the edge effect in BP, further in-depth study of methods to improve the material removal rate, and MSF error suppression methods in MRF.

2 Basic introduction to BP

2.1 History of BP

In 2000, Walker et al. [31] initially introduced the BP technology, presenting its underlying principles, advantages, and key technologies, which included the algorithm for computing dwell time and the modeling method for TIF. In 2001, the precession polishing method was introduced, accompanied by a detailed account of its reliability [32, 33]. In 2003, Walker et al. [34] achieved an ultra-smooth surface with an Ra value of 0.5 nm on BK7 glass, showcasing the significant potential of BP technology. Subsequently, several academic institutions, including University College London [35, 36], Huddersfield University [37, 38], Xiamen University [20–22], and Harbin Institute of Technology [39, 40],

have initiated research on BP technology. And more units have begun to study BP technology.

2.2 Principle of BP

As shown in Fig. 2a, BP tools are flexible spherical bonnet coated with polishing pads. When the bonnet is filled with air, it ensures that the polishing head matches the surface shape of the components, prevents slipping or idling, and enhances the polishing efficiency and surface quality. Different sizes of polishing tools for BP can be chosen based on the size of the workpiece, effectively ensuring processing efficiency [20, 31]. Figure 2b illustrates the typical polishing process using BP. The machine tool uses the flexible BP head to apply pressure to the workpiece, transferring it to the abrasive particles between the polishing head and the workpiece, leading to the removal of the workpiece material through friction and scraping by the abrasive particles.

Bonnet precession (BP) is commonly achieved through a process known as “precession polishing” [32, 33], demonstrated in Fig. 3a. During precession polishing, the spindle

consistently rotates while maintaining contact with the polished component at the normal angle (A axis), forming an arch referred to as the precession angle. Bonnet precession polishing transforms the “D”-shaped TIF produced by traditional vertical and inclined motion polishing into a regulated “Gaussian-like” TIF, enhancing the control over the surface shape. Varied TIFs can be created by altering the processing parameters, including BP pressure, downward pressure, feed angle, and spindle speed, thereby enhancing the spatial range of processing and theoretically eradicating the processing blind zone. Furthermore, precession polishing densifies the polishing texture through additional A-axis rotation, enhancing machining efficiency, reducing surface corrugation errors, and improving machining quality. The scratches resulting from different polishing modes are depicted in Fig. 3b.

In summary, BP technology represents an exceptional processing method with significant market potential, characterized by the following advantages [39, 40, 43]:

(a) Versatile adaptability: BP technology is exceptionally adaptable to a variety of workpieces with diverse surface

Fig. 2 Introduction to BP technology. **a** Physical drawing of the BP tool [20]. **b** The typical polishing screen of BP [41]

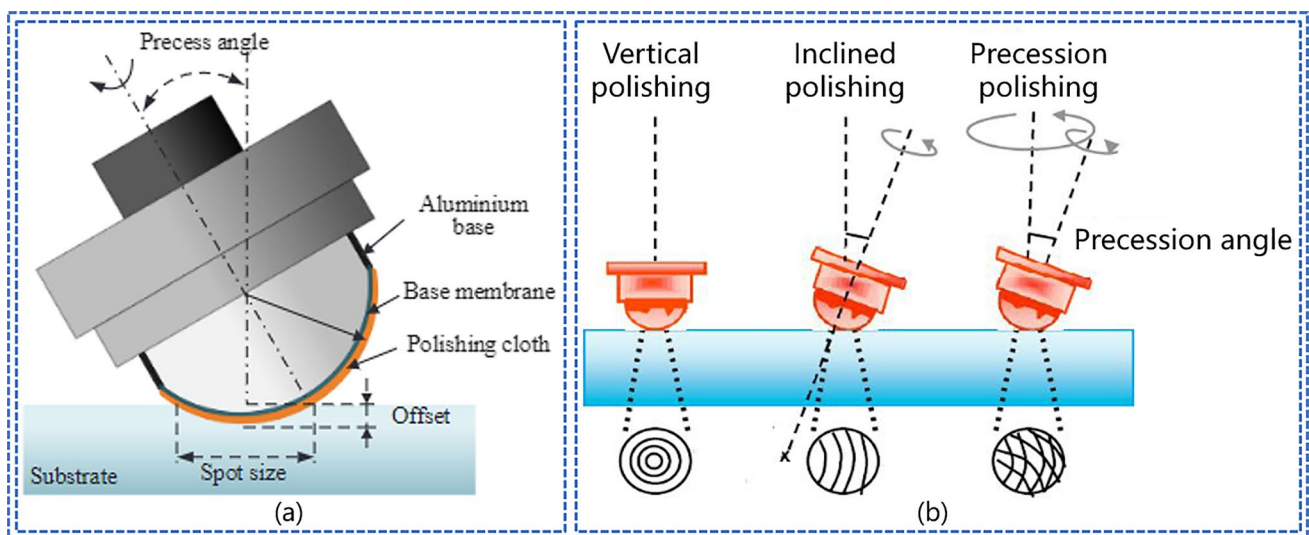
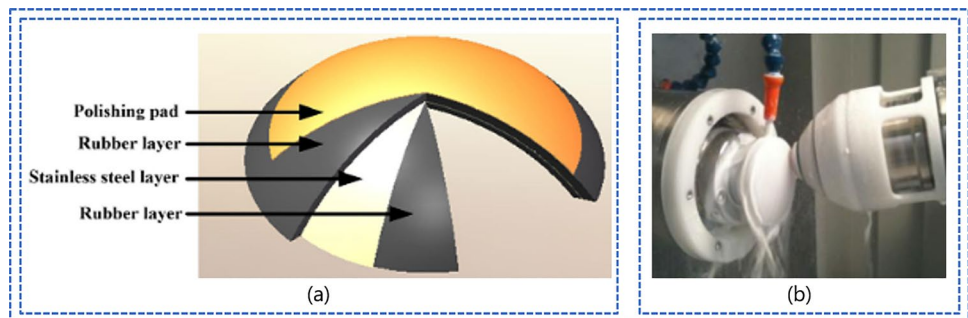


Fig. 3 BP principle. **a** The principle of precession polishing [42]. **b** Different polishing modes obtain surface texture [20]

geometries. It is particularly effective in handling aspheric surfaces or freeform surfaces, where it can conform to the workpiece's surface deformations. This capability allows it to overcome the limitations of traditional single point turning (SPT) and challenges associated with poor adhesion on aspheric surfaces.

(b) High polishing efficiency: BP distinguishes itself from other aspheric polishing methods through its high efficiency in polishing. This feature renders it especially suitable for the rapid polishing of large-scale astronomical telescopes, where time efficiency is crucial.

(c) Cost-effectiveness: The development and implementation costs associated with BP technology are relatively low compared to other advanced polishing methods. This cost-effectiveness makes it an attractive option for a wide range of applications.

(d) Scalability for various workpiece sizes: BP technology is capable of processing a broad spectrum of workpieces, ranging in size. This scalability is facilitated by the selection of appropriate polishing heads, tailored to the specific requirements of the workpiece.

2.3 Equipment of BP

2.3.1 Machines

Walker et al. [39, 44] developed the first commercial BP machine in the world, IRP200, with a maximum freeform surface size of 200 mm × 200 mm. The machine's appearance and internal structure are depicted in Fig. 4a, b, respectively. This development was followed by a series of smaller BP machines, including IRP20, IRP100, IRP2000, and IRP2400. In China, Gao et al. [45] at HIT were the first researchers to develop an experimental machine for BP, as depicted in Fig. 4c. The machine is controlled by CNC; it features six axes for machining optical workpieces with a maximum diameter of 200 mm. Subsequently, Ji et al. [46] developed a bonnet precession polishing platform assisted by a robot, which is based on a six-axis industrial robot. This is depicted in Fig. 4d. Despite successful development of experimental prototypes by researchers at HIT and ZJUT, these cannot be strictly considered as machine tools or full-fledged machining equipment. Guo et al. [47] at Xiamen University initiated the study of BP technology and produced the BP-2MK460 BP machine (shown in Fig. 4e). The HomoTech Company [48] in Xiamen, China, developed the HBP130 (shown in Fig. 4f), the first commercial BP machine to be commercialized in China. The commercialization of domestic BP machines signifies the transition of BP technology from scientific research to market production. It also extends BP's unique advantages to fields beyond optical processing.

2.3.2 Bonnet tool

The performance of the bonnet tool significantly impacts the quality of the polishing process. The rigidity of the polishing tool should not be excessive. Excessive rigidity would result in a traditional rigid tool polishing—losing the unique advantages of the bonnet polishing, such as good adaptability to aspheres. The flexibility of the polishing tool should not be too low. Otherwise, a tool with overly soft structure will decrease the certainty of the polishing process. Zeeko Ltd. [49] predominantly employs a BP tool featuring a ball-shaped, flexible laminate core structure (as depicted in Fig. 5a), presumably composed of Kevlar, possessing rigidity and flexibility. Specialized polishing cloths or pads embedded with abrasives can be affixed to the layer to polish optical surfaces, often used in conjunction with a polishing solution or water. Gao et al. [50, 51] enhanced the structure of the bonnet tool (as depicted in Fig. 5b) by incorporating fiber cloth material for the reinforcing layer, a 0.8-mm-thick polyurethane polishing pad for the polishing layer, and a 1–2-mm-thick rubber bonnet layer. Walker et al. [52, 53] developed the grolishing bonnet tool (as depicted in Fig. 5c), designed to mitigate MSF errors through the inclusion of metal rings, diamond pellets, and other materials affixed to the bonnet's surface. Beaucamp et al. [54, 55] introduced the shape adaptive grinding (SAG) process, which involves adhering a hard layer of particles, such as diamond, onto the polishing tool, as illustrated in Fig. 5d. The SAG process is applicable for the precision machining of challenging materials like ceramics and cemented carbide, enabling ductile mode grinding to attain a superior surface finish. Wang et al. [56, 57] developed and constructed a semi-rigid bonnet tool (refer to Fig. 5e) comprising a rubber layer, a stainless steel layer for increased stiffness, another rubber layer, and a polishing pad, in that specific sequence. The semi-rigid tool not only efficiently polishes aspheric optics but also reduces their characteristics after the grinding process. Kong et al. [58] designed a silicone bonnet tool adapted to the OptoTech ASP 200CNC-B as well as another tool with comparable functionality to the sub-bore polishing tool. LP66 polyurethane is a commonly used material for polishing pads, polyurethane is classified as a block copolymer, and polyurethane polishing pads contain a solid polishing agent that enhances the polishing process. Zhu et al. [59] proposed a non-contact polishing process (refer to Fig. 5f) utilizing non-Newtonian fluids (polymer and starch) in place of polishing pads to mitigate the impact of pad wear on polishing consistency. They achieved a 3.9-nm Ra finish on nickel.

2.3.3 Bonnet dressing tool

To maintain precise control over material removal and polishing efficiency despite bonnet wear and deformation

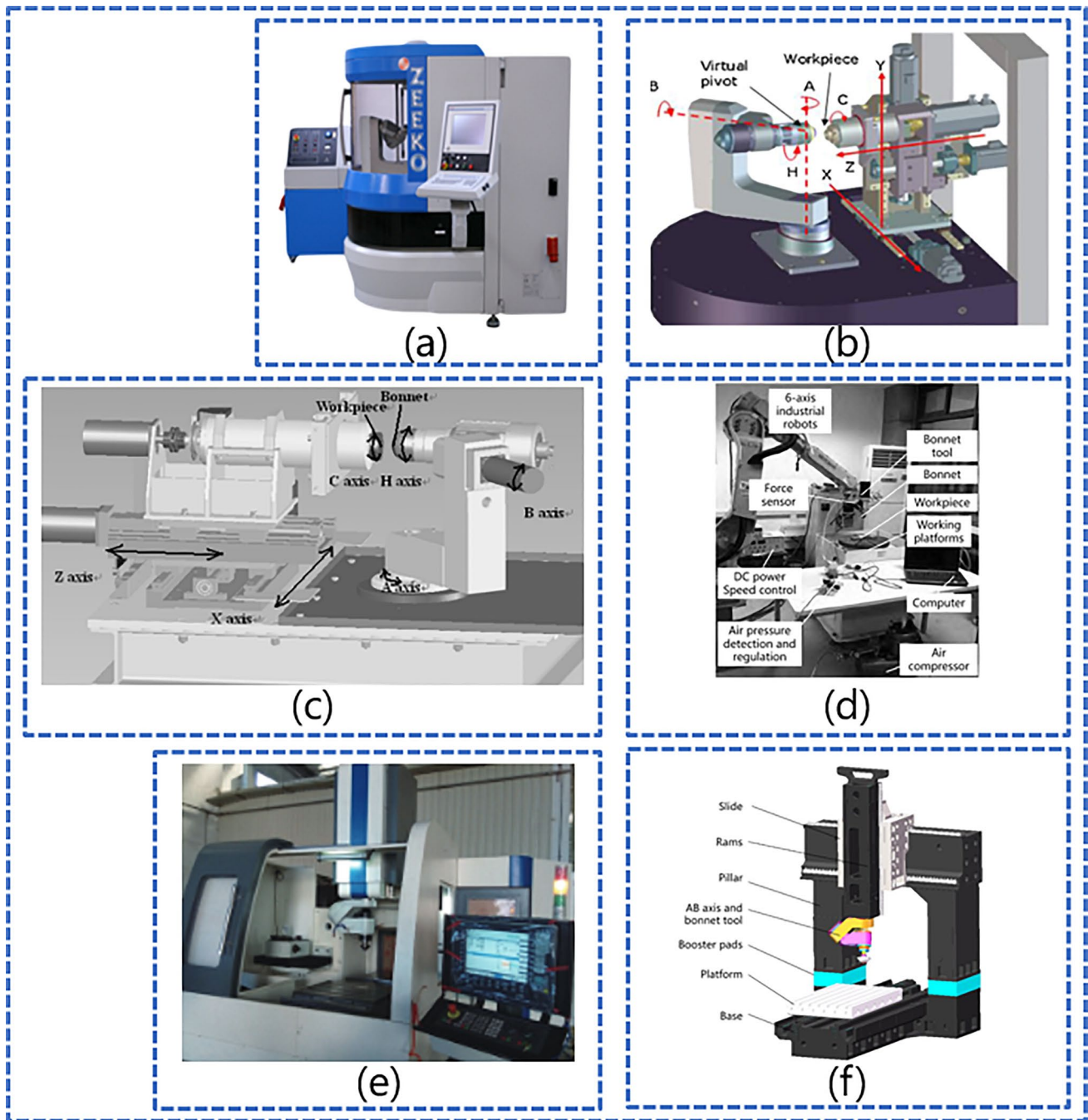


Fig. 4 BP machines. **a** IRP200 from Zeeko [46]. **b** The internal structure of the IRP200 7-axis machine [41]. **c** BP test machine developed by Harbin Institute of Technology [45]. **d** Robot-assisted bonnet pre-

cession polishing platform produced by Zhejiang University of Technology [46]. **e** BP-2MK460 BP machine from Xiamen University [47]. **f** HBP130 BP machine made by HomoTech Company [48]

during use, it is essential to periodically refurbish the bonnet tool to ensure its surface form accuracy. Utilizing the machine tool's motion allows for the design of an online dressing device that solely imparts rotational motion to the dressing wheel. When multiple processes, such as polishing and dressing, are combined on a single machine tool in mass production, it leads to a notable increase in non-processing

time, thus affecting the machining efficiency. Consequently, the development of dedicated offline dressing devices is imperative. Pan et al. [21] designed online dressing and offline dressing tools for the bonnet tool. The structural composition is shown in Fig. 6a, b, and the dressing process is shown in Fig. 6c, d, respectively.

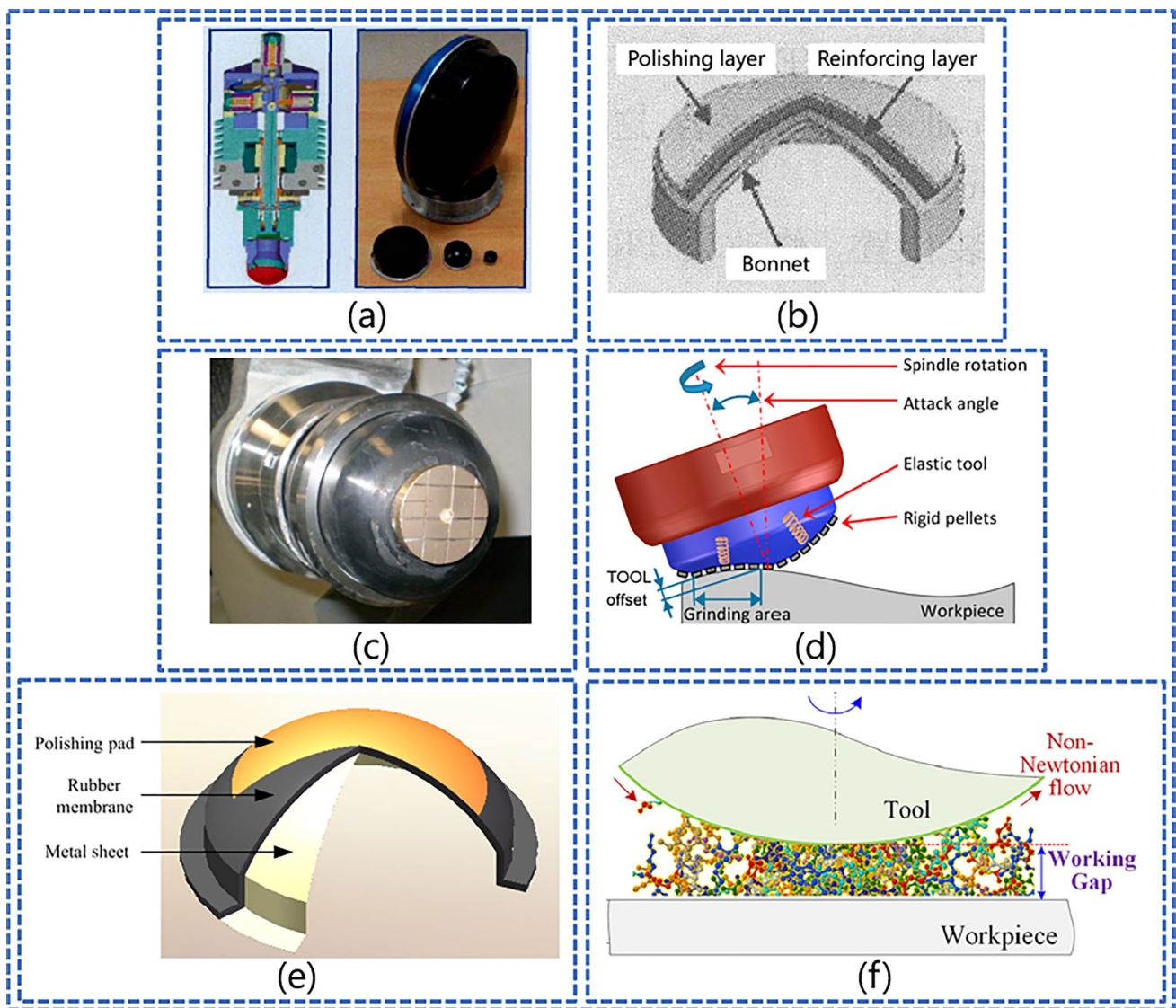


Fig. 5 Various bonnet tools: **a** bonnet tool produced by Zeeko Ltd. [49]. **b** Structure of bonnet tool improved by Gao et al. [50]. **c** Grinding tool created by Zeeko Ltd. [52]. **d** Principle of SAG [54]. **e**

Semirigid bonnet tool from Wang et al. [57]. **f** The principle of non-contact polishing process using non-Newtonian fluids proposed by Zhu et al. [59]

2.4 Application of BP

The application field of BP can be categorized into optical components, medical treatment, semiconductor, and industrial parts. For optical mirror processing, BP can be utilized throughout the entire polishing process to swiftly eliminate SSD and effectively manage surface accuracy. In medical treatment and semiconductor fields, BP primarily serves to reduce the surface roughness of components expediently.

2.4.1 Optical

In the field of optical lenses, multiple European Extremely Large Telescope (E-ELT) subscopes were polished using

the BP technique. Walker et al. [35, 36, 52] use a variety of polishing tools and a multi-stage process. These were combined with active control algorithms to model the TIF for the ultimate machining of ESO-compliant hexagonal samples. Walker et al. [62] reported several challenges encountered during the early-stage fabrication of a 500-mm-diameter f/1 ellipsoidal mirror for the UK’s technology development for Extremely Large Telescopes project, which had repercussions on the subsequent processing of the E-ELT.

2.4.2 Non-optical

In the field of industrial processing, Beaucamp et al. [56, 63] utilized a 7-axis CNC polishing machine to develop a forming

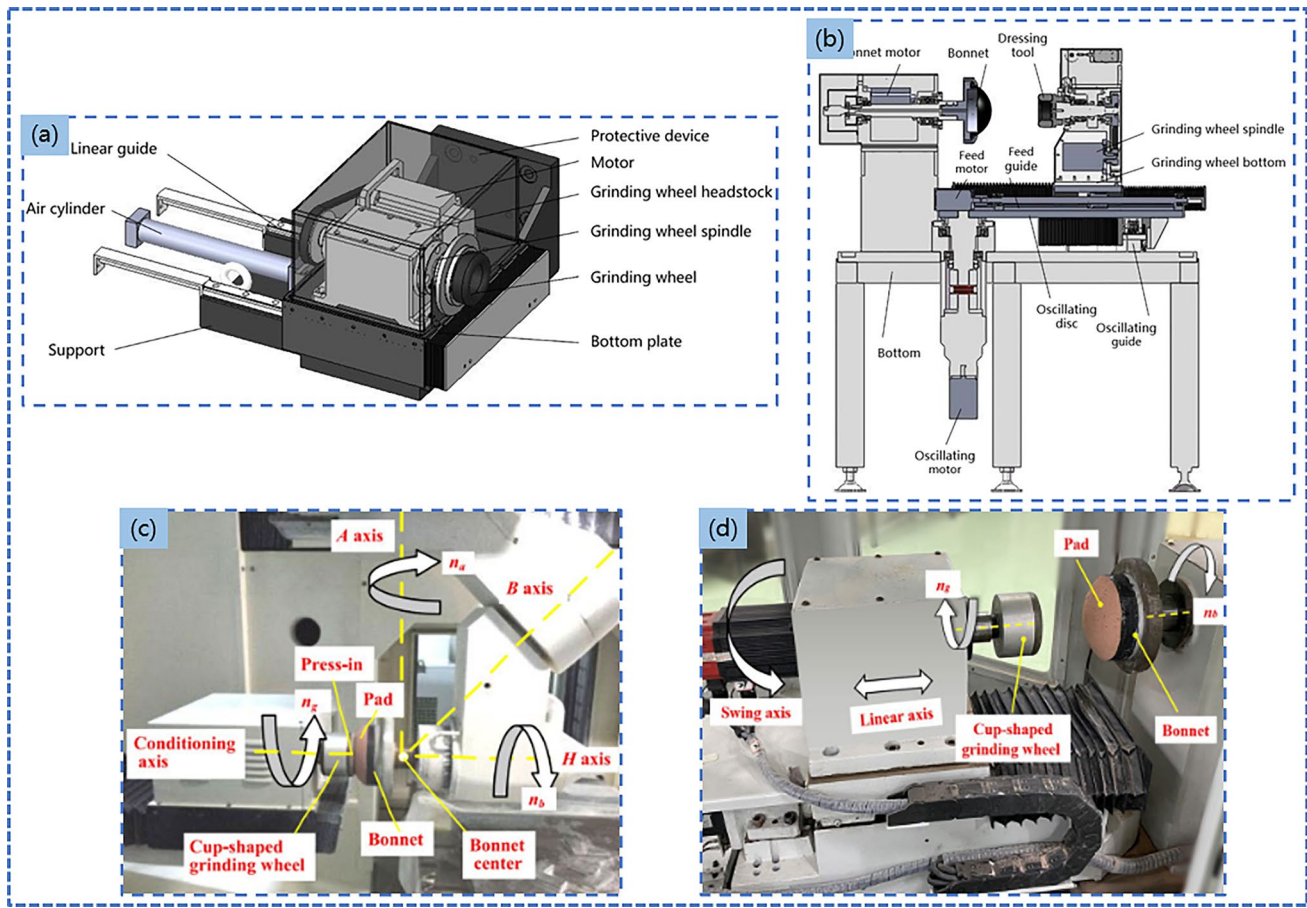


Fig. 6 Bonnet dressing tool. **a** Online dressing tool [21]. **b** Offline dressing tool [21]. **c** The process of online dressing [60]. **d** The process of offline dressing [61]

process and compensation software aimed at achieving BP for aspheric and free-form molds. Additionally, they combined jet polishing with BP to enable ultra-precision polishing of the surfaces of diamond-turned X-ray-formed molds on the same 7-axis CNC platform. Cheung et al. [64] utilized BP to construct structured surfaces. A surface topography simulation model and hence a model-based simulation system for the modeling and simulation of the generation of structure surfaces by using CCUP have been established and verified through a series of simulation and practical polishing experiments.

In the medical field, Zeeko Ltd. [65] performed initial polishing experiments on the prosthetic knee joint component, developed the polishing trajectory for the knee joint using NURBS curves, and ultimately attained a smooth surface with a roughness average (Ra) of 18 nm. Zeng et al. [37, 38] subsequently conducted a study to examine the influence of process parameters on the polishing force and material removal in bonnet-polished, medical-grade cobalt-chromium alloy joints. The study aimed to enhance the surface quality of the bearing surfaces for two types of prostheses and extend their service life.

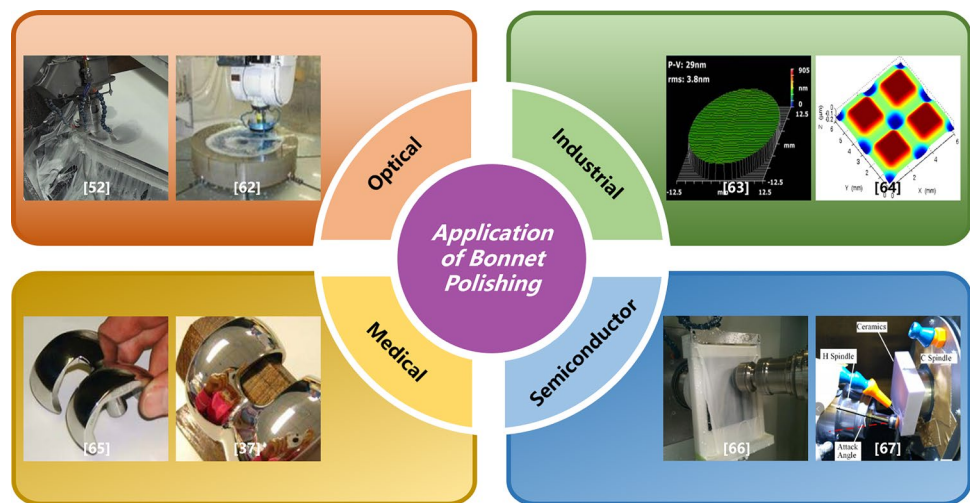
In applications in the semiconductor industry, traditional chemical–mechanical polishing techniques are inadequate for meeting the requirements of next-generation photomask blank finishing. Beaucamp et al. [66] employed BP techniques for error correction subsequent to the chemical polishing of EUV blank mask plates, achieving an improvement in PV to 50–100 nm. Zhu et al. [67] performed BP experiments on brittle ceramics, revealing that the combination of lower material hardness and higher tensile strength facilitates the expansion of the plastic removal zone, thereby enhancing the manufacturability of brittle ceramics. Figure 7 illustrates several applications utilizing BP.

3 Key techniques of BP

3.1 Modeling of TIF

Polishing and grinding exhibit distinct mechanisms of material removal [68–70]. During grinding, the mechanism

Fig. 7 Application examples of BP



is explicit: brittle materials develop median and lateral cracks under the abrasive’s compression and friction. As lateral cracks propagate and abrasives continue to exert pressure and friction, large chunks of material detach, potentially resulting in swarf larger than the abrasive particles themselves, making it challenging to achieve a smooth surface on brittle materials. In contrast, polishing involves a composite of two mechanisms: firstly, the continuous pressure of abrasives under the normal force provided by a soft polishing tool induces crack formation, leading to material removal; secondly, abrasives exert pressure under the shear force of the polishing fluid flow, creating cracks, while the vertical load borne by the workpiece surface mitigates crack formation. Due to the smaller size of abrasives and the gentle load applied in the polishing process, it is employed to smooth surfaces roughened by grinding and to eliminate subsurface damage introduced by grinding.

Due to the less-defined mechanisms of material removal in polishing, multiple statistical methods for quantifying the amount of material removed have emerged in the polishing process. The TIF represents the volume of material

removed per unit time. The shape of TIF dictates the spatial processing range of the BP tool, while the accuracy of TIF influences the surface quality and face shape error of the polished component. Material removal, as described by the Preston equation $dz/dt = kpv$, is contingent on pressure, velocity, and a comprehensive coefficient. Table 2 displays the research findings of various scholars on the TIF.

In the early development of the bonnet polishing (BP) technique, Walker et al. [75, 76] pioneered the measurement of the polishing spot contour and introduced the tool influence function (TIF) concept. Kim et al. [71] enhanced this by simulating the static TIF using Preston’s equations and comparing it with empirical measurements, achieving notable modeling accuracy (shown in Fig. 8a). In 2009, they further advanced this work by developing a range of TIFs for different sizes and optimizing dwell time and tool profiles through a comprehensive non-sequential algorithm, significantly improving surface error correction efficiency [77]. However, Jin et al. [78] made an investigation into the impact of process parameters on TIF overlooked the unique feeding process of BP. Meanwhile, Wang et al. [79, 80] used the finite element method to compare dynamic and static TIF

Table 2 Research on the BP TIF

Author	TIF
Kim [71]	$\Delta z = \kappa P_{\tau} (\exp(-\frac{\lambda^2}{2\sigma^2}))^{\Psi} [(V_{TRx} + V_{TFx})^2 + (V_{TRY} + V_{TFy})^2]^{1/2} \Delta t$
Wang et al. [20]	$sTIF_{continuous} = k \cdot \eta \cdot p_{max} \left[\exp\left(-\frac{(x^2+y^2)}{2\sigma^2}\right) \right]^{\Psi} \cdot \int_0^T \sqrt{(\omega_1 R \sin \alpha - l \sin \alpha - y \cos \alpha - \omega_2 y)^2 + (\omega_1 \cos \alpha + \omega_2 l)^2} x^2 dt$
Cao et al. [72]	$Vol_{mmr} = N_{ac} Vol'_p = \frac{2\eta K_{ac} V_c t V_r(x,y) P(x,y)}{H_w \tan \alpha} \left(\frac{R_q}{\sigma_z}\right)^{1/2}$
Pan et al. [73]	$RR = k \cdot \mu(n) \cdot P \cdot V \cdot t$ $\mu(n) = 1.21c^{-13}(n)^4 - 7.06c^{-10}(n)^3 + 1.55c^{-06}(n)^2 - 1.58c^{-03}(n) + 9.48e^{-01}$
Shi et al. [74]	$\rho = E_0 \int_d^{\infty} \frac{(z-d)^{\frac{3}{2}}}{3.03 \times 10^{-6} \sqrt{2\pi}} \exp\left[-\frac{z^2}{2 \times (3.03 \times 10^{-6})^2}\right] dz \cdot Ut.$

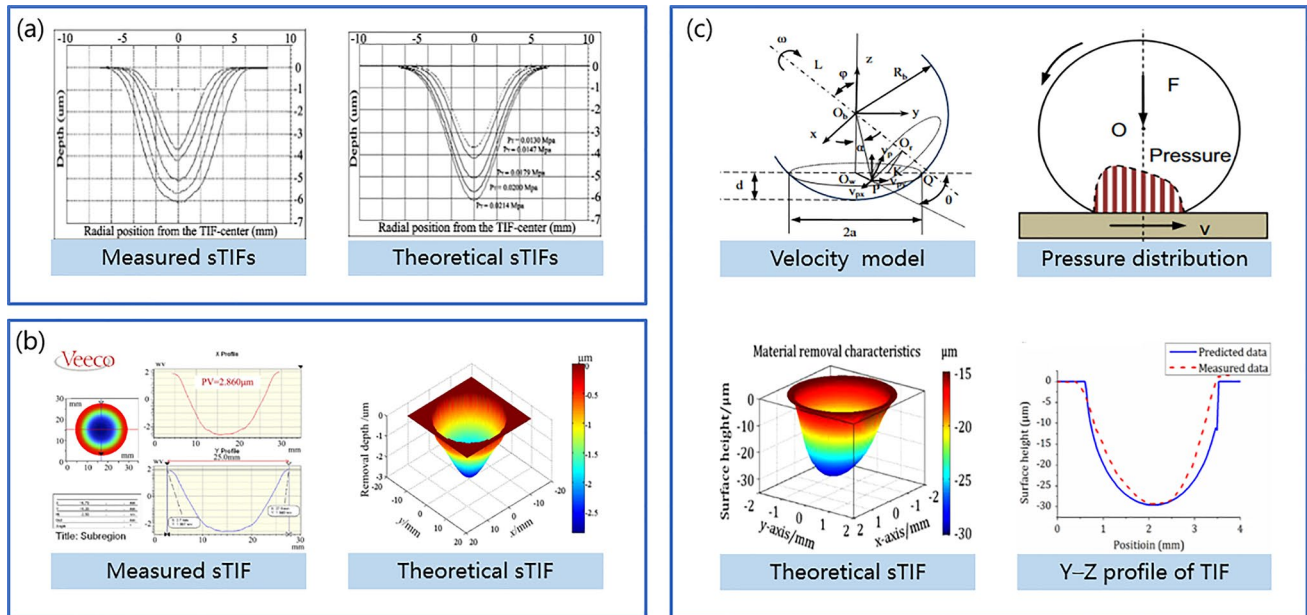


Fig. 8 a Comparison of measured BP sTIFs and theoretical sTIFs [71]. b Comparison of measured BP sTIF and theoretical Stif [79]. c Velocity model and pressure distribution of bonnet precession polishing [72]

errors, contributing to a broader understanding of TIF across different motion models. The measured TIF and simulated TIF are shown in Fig. 8b.

The limitations of existing research lie in the focus on traditional process coefficients, often neglecting factors like the friction coefficient and bonnet wear. Addressing this gap, Cao et al. [72] proposed a multi-scale model for computer-controlled BP (shown in Fig. 8c), refining the TIF model to predict material removal more accurately. Pan et al. [73] examined the constraints of the current TIFs and introduced a corrective approach for TIF utilizing the interfacial friction coefficient. Shi et al. [74] introduced a microanalytical model based on microcontact and tribological theories to comprehend these parameters, respectively. Future research should extend beyond conventional factors, considering aspects like tool wear, slurry properties, and lubrication in TIF modeling. This approach promises to bolster the reliability of the polishing process.

Additionally, with regard to the dynamic TIF, Wang et al. formulated the dynamic TIF of BP, introduced a corrective approach for stress in the static contact area, and identified a displacement of the lowest point of the dynamic TIF in the opposite direction of the polishing head movement, as derived from the static TIF [80]. Wan et al. [81] found that an excessively large feed rate results in a notable discrepancy between the actual TIF and the theoretically derived TIF. Zhong et al. [82] explored the impact of surface curvature on the contact area between the bonnet and the component. Han et al. [83] introduced a Gaussian mixture model (GMM) to represent the TIF of a polishing tool. This enables

optimal feed scheduling within the machine tool's dynamic constraints, while optimizing its dynamic stresses through adaptive path spacing.

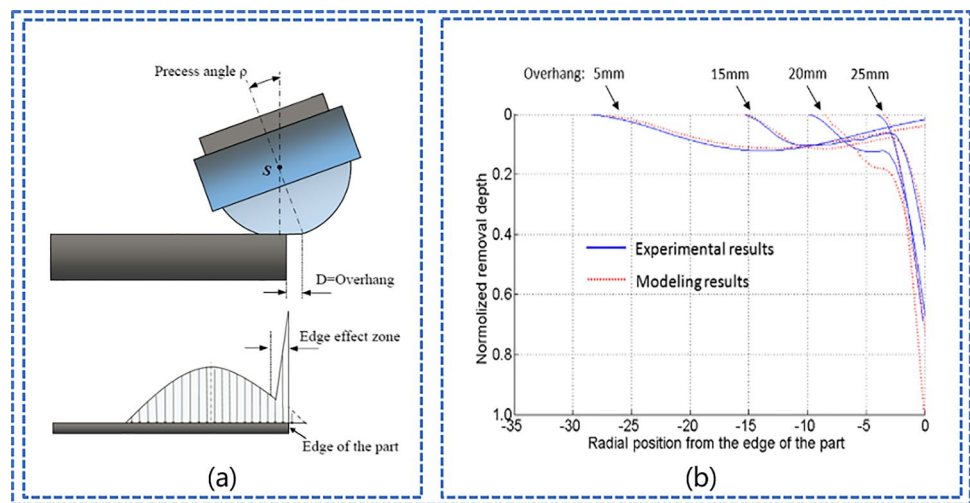
The center position of the dynamic TIF is shifted in the x and y directions, aligning it closer with the actual production scenario. As a result of the disparity between the dynamic and static TIF, the dwell time at the dwell point needs to be adjusted. Hence, the quantitative correlation between dynamic and static TIF should be examined and rectified in the dwell time algorithm.

3.2 Control on edge effect

Considering that BP involves contact polishing, warping may occur during the processing of the workpiece's edge area if the polishing head does not reach the edge, while the edge may collapse if it does, resulting in the “edge effect” [84]. Figure 9a illustrates the schematic of the overhang and the varied pressure distribution between the bonnet and the workpiece with different overhangs [85]. In Fig. 9b, the TIFs are depicted when the bonnet polishes the edge of the workpiece during the polishing of the components' edge [57]. The polishing force increases sharply due to the non-uniform distribution of the polished area, unlike when polishing the inside of the components. Consequently, there is a sharp increase in the material removed at the edge.

Controlling the edge effect is a challenging task. Walker et al. [86] introduced an active suppression process for mitigating edge effects, termed “Tool-Lift” (refer to Fig. 10a).

Fig. 9 **a** Conceptual sketch of the pressure distribution between the bonnet and the component [85]. **b** Phase map from turned-up edges after pre-polishing with R160 bonnet and 60-mm spot [35]



Tool-Lift involves actively lifting the polishing head prior to reaching the workpiece’s edge to minimize contact pressure and area, thereby decreasing material removal.

This technique is widely used to mitigate edge effects in BP. Wang et al. [87] discussed the utilization of Tool-Lift, edge filling material (depicted in Fig. 10b), and nodding polishing (displaying continuous precession angle changes during polishing, as illustrated in Fig. 10c). They found that using filling material at the edges offers more advantages in polishing small components. The component profiles obtained by filling material method and nodding polishing method are shown in Fig. 10e, f. Beaucamp et al. [35, 36] utilized various polishing heads and grading processes

such as grolishing, pitch-polishing, and compliant bonnets for both pre- and corrective polishing. These techniques were integrated with an algorithm specifically developed to proactively mitigate fringing effects, with the objective of accurately modeling the TIF. Following this integration, the hexagonal lenses underwent processing to ensure compliance with the ESO standards. The hexagonal lense polished with Tool-Lift method is shown in Fig. 10d. Li et al. [85] optimized the feed rate, tool offset, and precession angle resulting in achieving a 200-mm hexagonal component with a peak-to-valley (PV) surface deviation of 189 nm and a root mean square (RMS) surface roughness of 26 nm. Ke et al. [88] identified the ideal overhang ratio for the bonnet

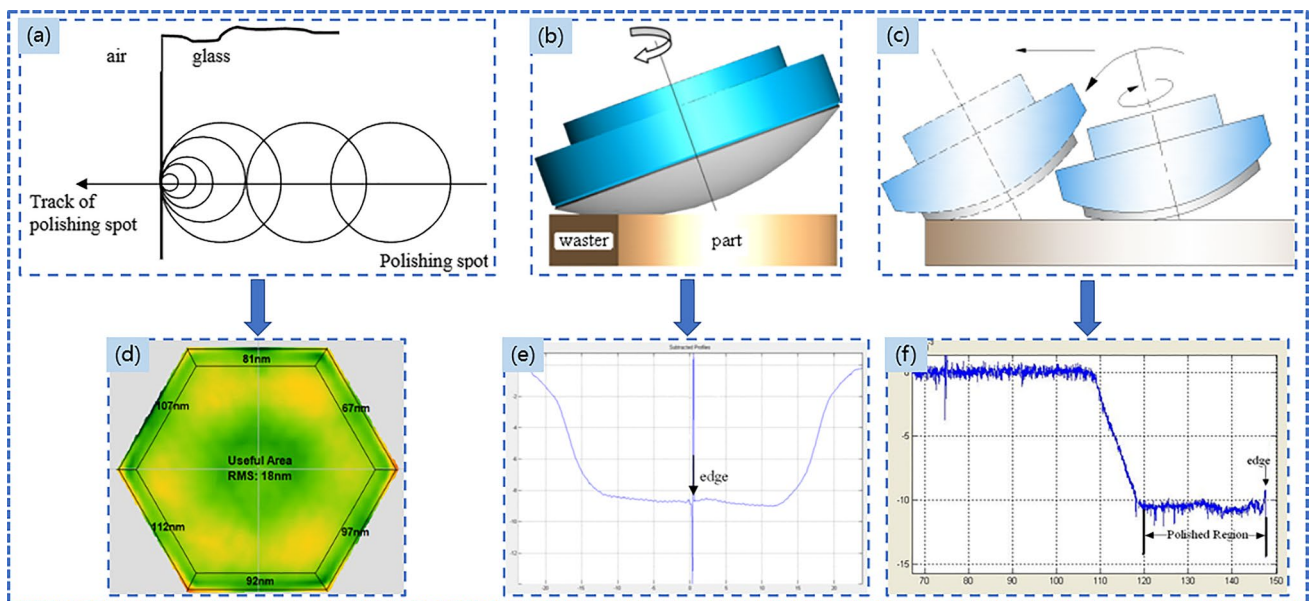


Fig. 10 **a** Principle of Tool-Lift method [86]. **b** Scheme of filling material around edges [87]. **c** Scheme of nodding polishing [87]. **d** Edge control result using Tool-Lift method [36]. **e** Profile obtained

from a Talysurf showing the combination of Zerodur surface and Zerodur waster [87]. **f** Result from Talysurf with nodding polish [87]

tool at the edge, where the TIF exhibits minimal width and maximum depth. This configuration facilitates rapid removal of warped features at the edge without causing damage to the bonnet tool. Currently, there is no effective method to manage the edge effect, with the prevailing approach being the Tool-Lift method. However, Yin et al. [89] introduced an edge control method utilizing the M-type STP TIF. The BP process can precisely generate M-type TIF when the precession angle is 0; therefore, it is imperative to expand this methodology to BP.

3.3 Control on MSF error

Polishing an optical component with a bonnet introduces a small ripple error on the element's surface, classified as a spatial frequency MSF error. This kind of error is also introduced to the component during its previous grinding process.

In 2011, Yu et al. [52, 53] discovered that LSF errors can be eradicated through subaperture polishing correction, while HSF errors can be eliminated using compliant polishing techniques. However, they found that addressing MSF errors was more challenging. To combat this, they designed a semi-rigid asphalt disk surface Grolishing bonnet tool, which mitigated MSF errors by attaching metal rings and diamond pellet pieces to the bonnet surface, as illustrated in Fig. 11. Despite its ability to suppress components' MSF, the grolishing tool bears a strong resemblance to the STP but exhibits lower polishing precision, ultimately compromising the surface's faceted accuracy during the retouching phase [90].

Wang [20] conducted an analysis to investigate the effects of air pressure, press offset, spindle speed, precession angle, and path interval on ripple error using orthogonal experimental analysis. The primary and secondary relationships of these factors on waviness error were determined to be path interval > press offset > air pressure > spindle speed > precession angle. He also conducted that the PV value increases sharply when the path

interval exceeds 4 mm. Zhong et al. [91] examined the impact of the number of precession steps on MSF error in bonnet precession polishing and achieved a smoother surface with reduced roughness and MSF error (shown in Fig. 12b). Huang et al. [92] studied the impact of polishing process parameters on the distribution of MSF error and observed that the error distribution was particularly influenced by spindle speed and feed speed. They successfully mitigated the IF error, resulting in a surface with an RMS of 1.6 nm (shown in Fig. 12c). Rao et al. [93] incorporated the Bessel function to isolate the bonnet radius, precession angle, and contact radius characteristics in the BP process. Their investigation revealed that the extent of scratch ripple bending in TIF is predominantly associated with optimizing the precession angle of the bonnet tool. By preventing the concentration of scratch direction, it is possible to alleviate the surface texture across a broad range of applications.

The method of improving component MSF without increasing the complexity of polishing path is summarized above—optimizing process parameters. Significantly enhancing the MSF characteristics of a component in the polishing process is challenging. The primary method for mitigating MSF errors involves enhancing the randomness and complexity of the polishing path, which will be the focus of the subsequent section.

3.4 Path planning

The polishing path has a profound impact on the face shape and MSF error of the optical component. A methodical and rational polishing path guarantees uniform polishing of all surface areas of the optical element by the tool, contributing to enhanced surface quality [94].

The two most classical polishing paths are the raster path (Fig. 13a) and the spiral path (Fig. 13b) [20]. These two paths are extensively utilized in practical production.

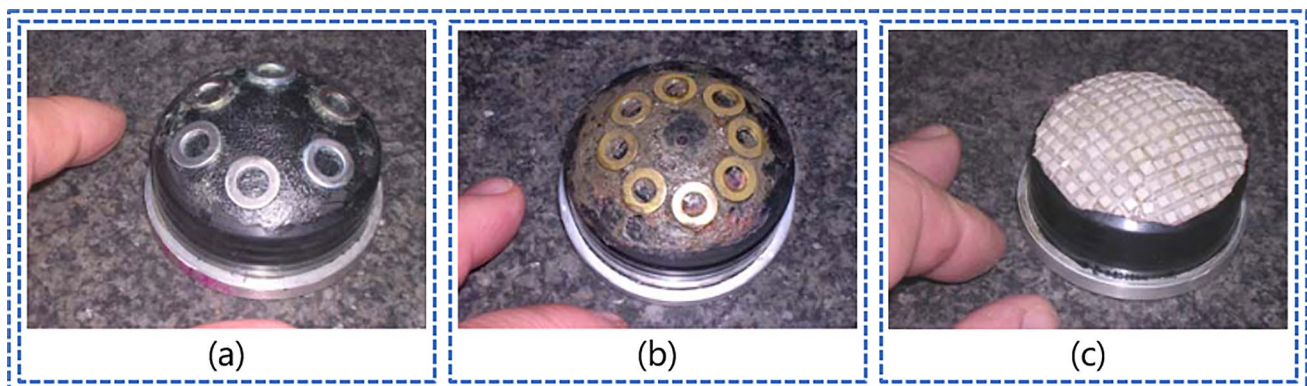


Fig. 11 Different grolishing tools [53]. **a** Stainless steel washers on 40-mm bonnet. **b** Brass washers on 40-mm bonnet. **c** 3 M Trizact™ on 40-mm bonnet

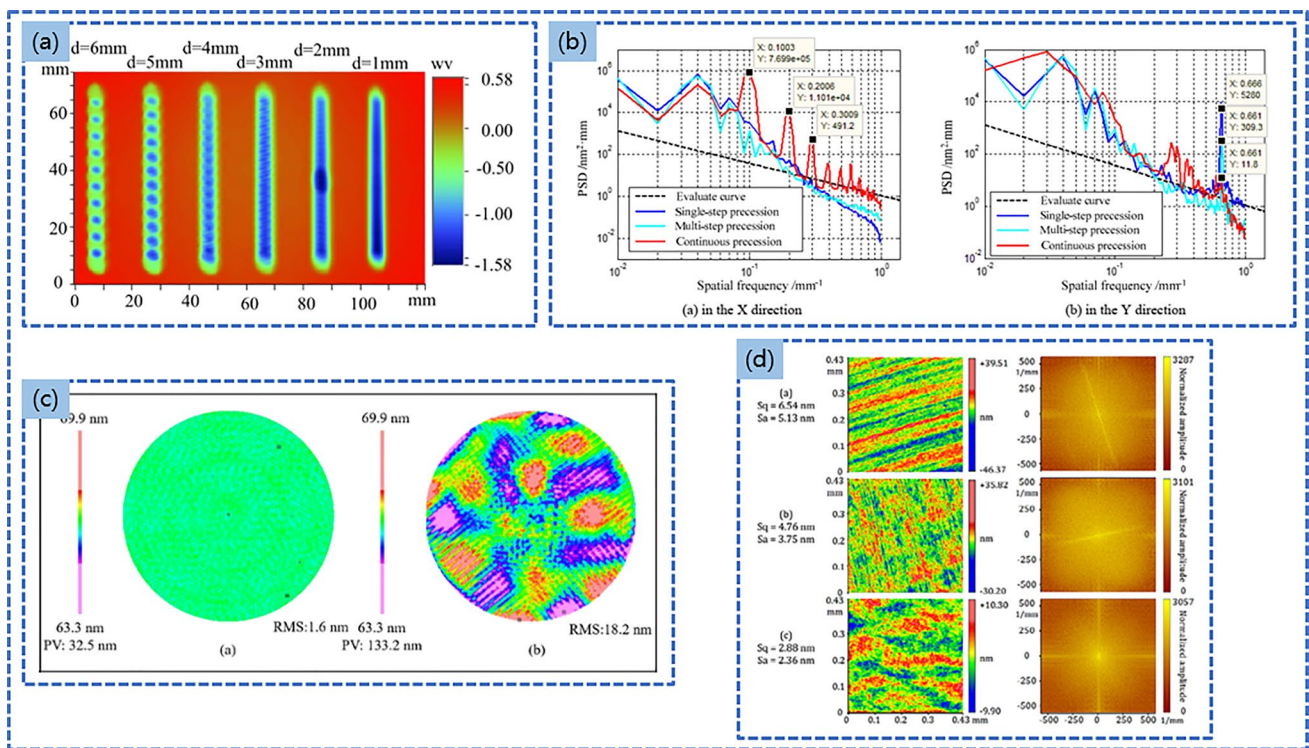


Fig. 12 **a** The processing results of the experiment to explore the influence of path internal on ripple error [20]. **b** Experimental PSD curves of single-step precession, multi-step precession, and continuous precession [91]. **c** Comparison of surface texture polished by

optimized parameters and an optimized parameters [92]. **d** Polishing result of surface topography and its spectrum in a resampled area with three sets of process parameters [93]

However, due to their regularity, they can introduce numerous ripple errors on the component surface. Cho et al. [95] incorporated the Lissajous graph (Fig. 13c) into the polishing path, resulting in a partial suppression of the ripple degree error. Pessoles [96] and Moumen [97] introduced the residual pendulum line (depicted in Fig. 13d) as part of the polishing path. While the Lissajous graph and cycloid line offer a notable improvement in complexity compared to raster paths and spirals, there is still a need for higher randomness in these four curves. Mizugaki et al. [98] introduced the Hilbert graph (depicted in Fig. 13e) into the polishing path and conducted experimental verification of its effectiveness in suppressing the MSF error. Tam et al. [99, 100] compared the Hilbert path with the Peano path (illustrated in Fig. 13f) and observed that the surface of the component polished by the Peano path exhibited lower PV value.

While many of the previously introduced paths retain some regularity, they must sufficiently aid in suppressing the ripple degree error. Walker et al. [101, 104] devised a pseudo-randomized polishing path (depicted in Fig. 13g) to enhance complexity and randomness, effectively reducing the ripple error (MSF error) on the component surface, thereby lowering the IF error and enhancing the power spectral density (PSD). Wang [20] presented a single-row

pseudo-random polishing path based on the maze path (as shown in Fig. 13h). He cooperated with the feed polishing, effectively suppressing the generation of MSF errors. Takizawa et al. [102] introduced a new circular pseudo-random path (illustrated in Fig. 13i) that exhibits smoother characteristics compared to the simple pseudo-random path and aids in suppressing the MSF error. Zhao [103] introduced a six-directional pseudo-random consecutive unicursal polishing path (illustrated in Fig. 13j). This approach provides multi-directional movement, increased randomness, smooth transitions, and continuity.

The proposed combination of the BP and MRF process in this article introduces a novel approach to polishing. Traditionally, in the pre-polishing stage, operators tend to limit the use of paths to raster and spiral paths. However, during the figuring and finishing stages, multiple iterations of component polishing are required, necessitating the continued use of these paths for minor material removal. This is followed by the adoption of more intricate paths for tasks such as homogenizing MSF. Notably, the current literature lacks reports on path planning at the edge when BP is utilized to address the edge effect. In essence, there is ample room for future enhancement of the polishing path generation mode to enable multi-functional capabilities.

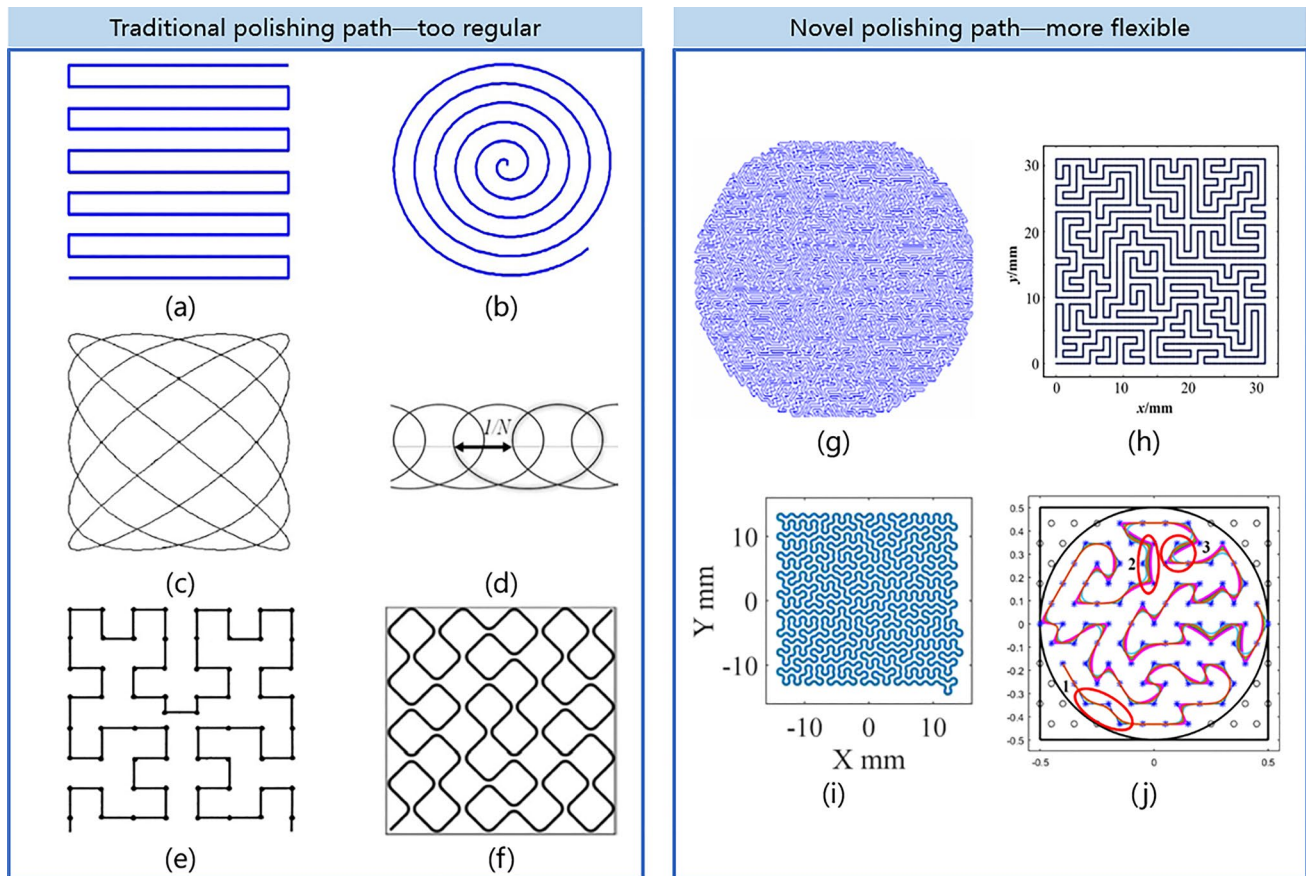


Fig. 13 Diverse polishing paths. **a** Raster path [20]. **b** Spiral path [20]. **c** Lissajous graphic path [95]. **d** Cycloid graphic path [96]. **e** Hilbert graphics path [98]. **f** Peano graphic paths [100]. **g** Pseudo-random

polishing path [101]. **h** Maze path [20]. **i** Circular pseudo-random path [102]. **j** Six-directional pseudorandom consecutive unicursal polishing path [103]

3.5 Compute of dwell time

Material removal during polishing can be conceptualized as the movement of the polishing head in a two-dimensional plane, allowing the process to be perceived as a two-dimensional convolution. The dwell time of the solution method can be partitioned into forward and reverse methods. The forward method, involving iterative algorithms and a prescribed set of dwell times to compute surface errors, iterates until achieving the desired surface type. On the other hand, the inverse method calculates the residual error between the current and final surfaces and determines the dwell time through inverse convolution of the residual error and TIF [105–108]. The iterative algorithm in the discretized model exhibits a generally slow convergence and may fail to converge due to oscillations in the calculation process. The Fourier transform method cannot process the TIF when it approaches zero, resulting in a negative dwell time. Although the linear system of equation algorithm can yield high accuracy, it requires enormous computational effort, leading to sluggish solution speed.

Wang et al. [109] optimized the algorithm for dwell time, as illustrated in Fig. 14a. They introduced an adaptive coefficient, ψ , to expedite the convergence speed during the solution process. The initial surface error, $PV = 1741.29$ nm, $RMS = 433.204$ nm, after two simulation steps reduced to $PV = 11.7$ nm, $RMS = 0.5$ nm, as depicted in Fig. 14b, c. Zhang et al. [110] took into account the machine's dynamic characteristics when determining the dwell time by constraining the range of machine motion speed variation between adjacent points and aimed to achieve lower RMS and PV values through the solution process. Lee [111] employed the Lucy-Richardson iterative algorithm for deconvolution, computed the convergence ratio, specified the machining allowance, and developed the optimized dwell time function. Zhao et al. [112] enhanced the grouped LSQR algorithm by implementing staggered grouping for dwell time calculation, resulting in the convergence of RMS and PV values to a lower range within three iterations.

The abovementioned literature has demonstrated that the existing dwell time algorithm exhibits high precision in the non-edge regions of the component. However, extensive

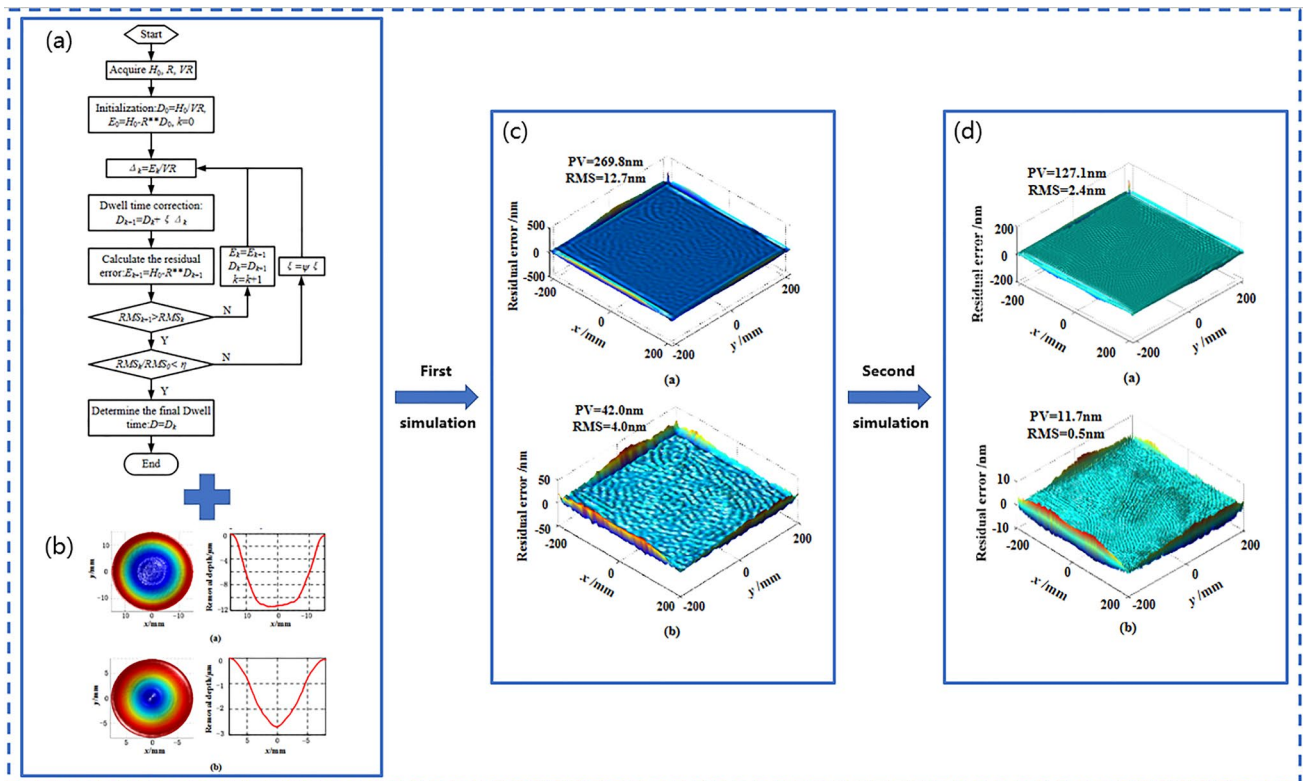


Fig. 14 Principle of self-adaptive iterative algorithm and its performance [109]. **a** Flow chart of the self-adaptive iterative algorithm. **b** Two measured TIFs were used in the simulation. **c** Surface residual

error after the first simulation process using the self-adaptive iterative algorithm. **d** Surface residual error after the second simulation process using the self-adaptive iterative algorithm

research is still needed to find an algorithm for correcting the dwell time at the component’s edge regions.

3.6 Wear of bonnet tool

Taking into account that BP is a type of contact polishing, the stability of the TIF and material removal during the polishing process will be affected by the wear of the polishing tool. Consequently, the surface accuracy of the optical element cannot be maintained.

Su et al. [113] established that wear of the polishing tool induces modifications in the surface microstructure and in the radius of curvature of the polishing head, potentially impacting the stability of the TIF. Park et al. [114] conducted a morphological analysis of polishing pads using SEM and demonstrated that randomly distributed micro-convexities in the polished contact area result in non-uniform surface roughness distribution, thereby leading to instability in material removal characteristics. Belkhir et al. [115] utilized SEM to analyze polishing pads at various polishing stages and demonstrated that abrasive particles and debris removal from the workpiece were the primary contributors to pad wear. Additionally, Yann et al. experimentally identified wear of polishing tools as one of the foremost reasons

for the instability of material removal characteristics. Yann et al. [116] experimentally pointed out that the wear of polishing tools is one of the most important reasons for the instability of the material removal characteristics. Zhong et al. [117, 118] investigated the removal characteristics of BP tools under varying wear conditions. They observed that the impact of different bonnet tool wear levels, as illustrated in Fig. 15a, b, on the stability of the removal characteristics escalates with the tool wear level. The reduction in friction coefficient due to tool wear is a primary factor leading to decreased removal efficiency. Shi et al. [119] incorporated the time-varying effects of polishing pad wear into their investigation of polishing mechanisms and material removal stability. They introduced novel models capable of addressing the decline in material removal caused by wear of the polishing tool. Zhang et al. [120] determined that the flexibility error and force state of the bonnet tool during processing were concurrently influenced by both short-term stress relaxation and long-term creep effects. The wear of polishing tools accumulates over time, necessitating a significant service period to collect wear samples. Consequently, conducting the wear experiment over an extended duration allows for obtaining a more precise correlation between the wear degree and the changes in TIF. By integrating this

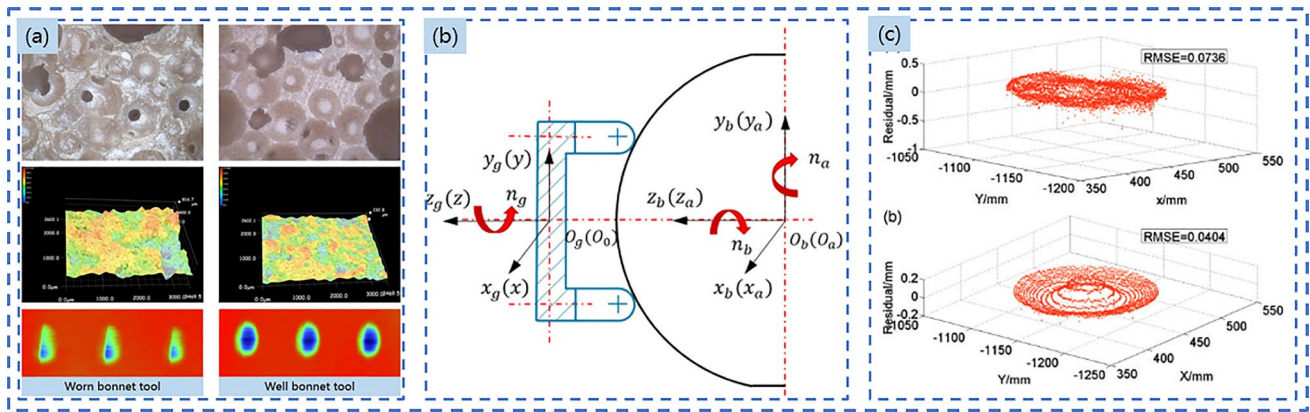


Fig. 15 **a** Conditions of worn bonnet tool and well bonnet tool [118]. **b** Schematic diagram of bonnet polishing tool dressing system [61]. **c** Comparison on the measurement result (RMSE) of bonnet tool before dressing and after dressing [122]

relationship with dynamic TIF, more precise prediction results can be achieved [121].

In the bonnet tool dressing, Wang et al. [122] proposed a dressing scheme using cup diamond wheel for bonnet tool, and then conducted the feasibility of the dressing scheme by analyzing the trajectory and the envelope of the diamond particles on the cup wheel; the dressing result is shown in Fig. 15c. Pan et al. [61] established the trajectory model of the dressing process using multi-body theory and developed an optimization method to optimize the process parameters. When polishing tools were dressed using the best process parameters, the surface quality of the polishing tools improved by 86.57% to 35.92 mm on average.

4 Basic introduction to MRF

4.1 History of MRF

The concept of MRF was first introduced and validated by Kordonski in 1986. The first prototype of MRF, depicted in Fig. 16a, was developed by Kordonski et al. [123] in 1992, and it had various limitations. In 1993, Kordonski and his colleagues were invited to the Center for Optics (COM) at the University of Rochester to conduct MRF research [124]. In 1995, the Center for Optics (COM) [125, 126] developed wheel-type MRF equipment, achieving a surface roughness of less than 1 nm. In 1996, Golini et al. [126–128] recognized the commercial potential of MRF and founded QED Technologies to initiate its commercialization. Subsequently, in 1998, the world's first commercial MRF machine, Q22, was launched at QED, paving the way for a series of MRF machines tailored for ultra-precision polishing of aspheric optics, including Q22-XE, Q22-X, Q22-XY, and Q22-400X (demonstrated in Fig. 16c).

In China, Zhang et al. [23–25] conducted the pioneering MRF research, developed a testing platform, and achieved surface roughness reductions to 1.55 nm and 1.47 nm for two types of components. Peng et al. [26, 129, 130] developed a prototype for wheel polishing, achieving a surface roughness of less than 1 nm, and demonstrated KDMRFs—MRF machine tools (displayed in Fig. 16d) to establish the standardization of the machinery.

4.2 Principle of MRF

MRF is a technology that utilizes the rheological properties of magnetorheological fluids under the influence of a magnetic field to polish workpieces, as illustrated in Fig. 17. A specific polishing gap exists between the workpiece and the polishing wheel. As the magnetorheological fluid enters the polishing gap via the circulation system, it transforms into a viscous-plastic Bingham fluid, characterized by increased hardness and viscosity, thereby forming a ribbon with a distinct shape. The abrasive particles within the magnetorheological fluid are not affected by the magnetic field, causing them to float to the top of the ribbon, creating a “flexible polishing mode.” The increased hardness and viscosity of the ribbon result in the formation of a ribbon with a specific shape. Furthermore, the abrasive particles in the magnetorheological fluid are unaffected by magnetic fields, allowing them to hover above the ribbon and form a flexible polishing mode [25, 26, 130].

MRF technology is an advanced optical fabrication method with the following advantages [25, 26, 130]:

1. High surface quality. The flexible polishing mold employs a unique shear action to adjust its cutting action, resulting in high surface quality. The workpiece's

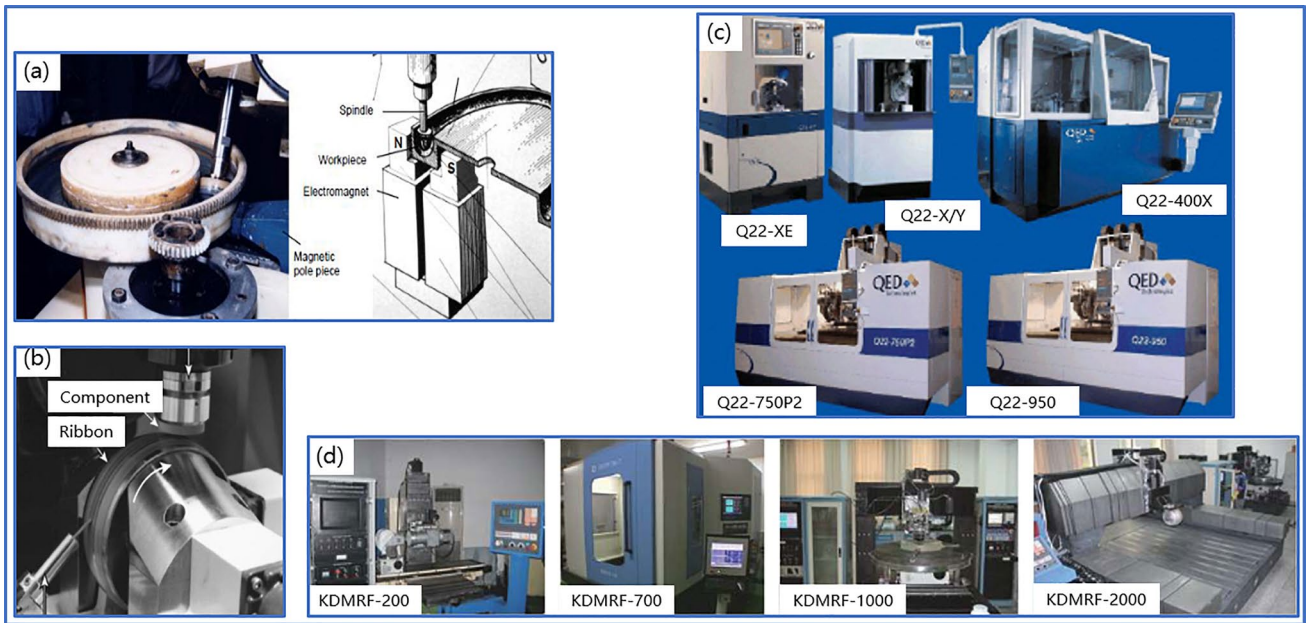


Fig. 16 Some MRF devices. **a** Prototype of MRF built in 1992 by Kordonski et al. [123]. **b** Wheel wheel-type MRF prototype was built in 1995 by COM [125]. **c** Q22 series MRF machines of QED [126]. **d** KDMRF series MRF machines built by NUDT [129]

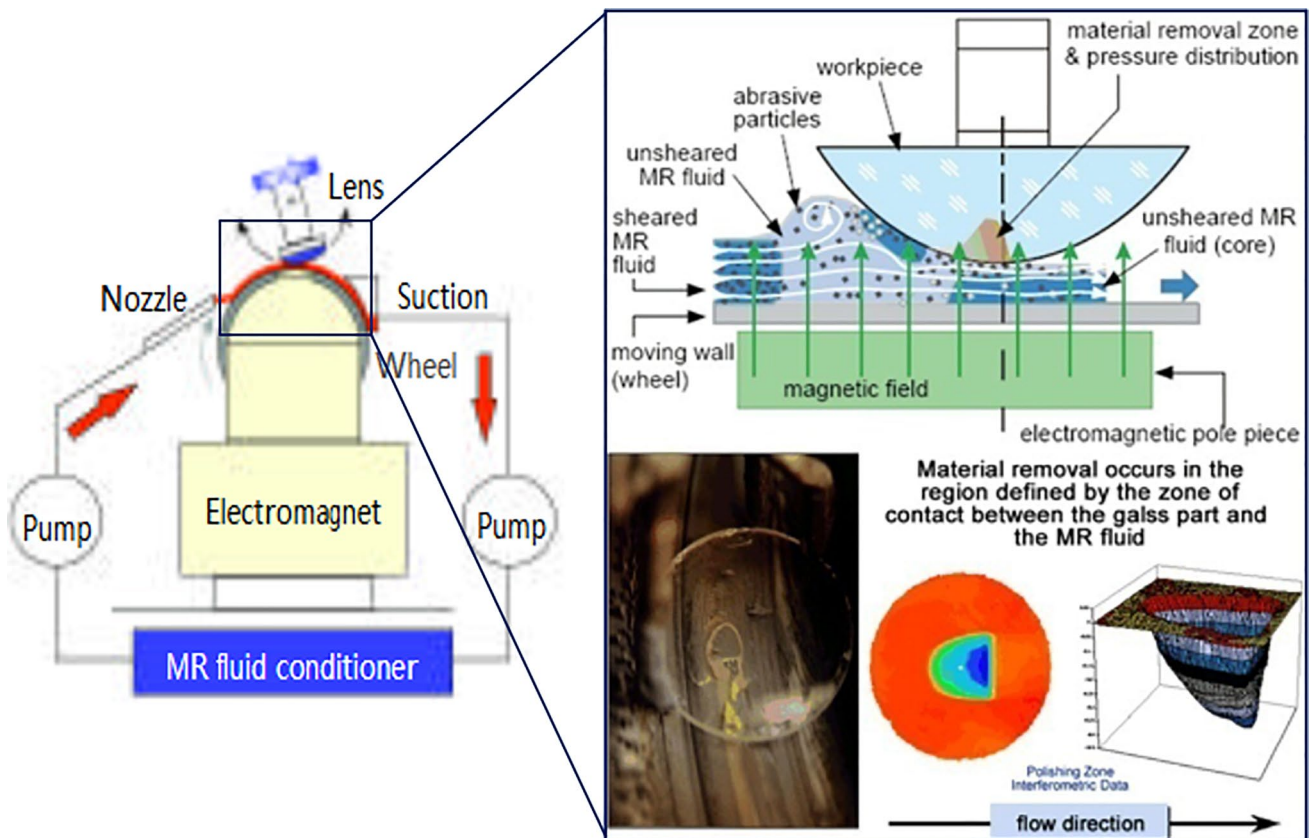


Fig. 17 Principle of MRF [131]

surface and stress subsurface layers are minimal, thus preventing sub-surface damage.

2. High precision of surface shape. Computer control allows for quantitative material removal, which simplifies the process of repairing the shape of optical components.
3. Easy computer control. Controlling the flexible polishing mold allows for efficient polishing, and when combined with computer control of the polishing trajectory and dwell time, it facilitates computer-controlled automatic manufacturing.
4. No tool wear. The circulation of magnetorheological fluid through a recirculation system eliminates tool wear, a common issue in CCOS.

4.3 Type of MRF

The classification of MRF types is primarily determined by the shape of the MRF tool, which includes wheel, disc, ball-end, and other configurations.

4.3.1 Wheel type

The polishing wheel rotates beneath the workpiece, forming an upright structure (as depicted in Fig. 18a). In contrast to

the upright wheel type, the Q22-2000F and KDMRF1000 machines are suitable for processing large- and medium-sized workpieces, with the polishing wheel situated above the workpiece (as illustrated in Fig. 18b), which are identified as inverted wheel type [132]. Yadav et al. [133] designed a magnetorheological gear profile finishing (MRGPF) (principle shown in Fig. 18c) machine, which significantly improved gear profile surface finishing, reducing the surface roughness from Ra 242 to 25.3 nm. Sato et al. [131] studied the rapid MRF process (illustrated in Fig. 18d) of the aerospace alloy Ti-6Al-4 V, employing a high-speed biaxial magnetorheological tool affixed to the spindle. They achieved mirror-quality finishing of challenging aerospace-grade materials that are difficult to machine. Li et al. [134, 135] implemented MRF using industrial robots (as depicted in Fig. 18e) and improved the face shape accuracy of a 1000 mm × 470 mm SiC off-axis aspherical mirror from 45.76 nm RMS to 22.78 nm RMS.

4.3.2 Disc type

In the pursuit of enhancing the material removal efficiency of MRF, Guan et al. [136, 143] conducted optimization

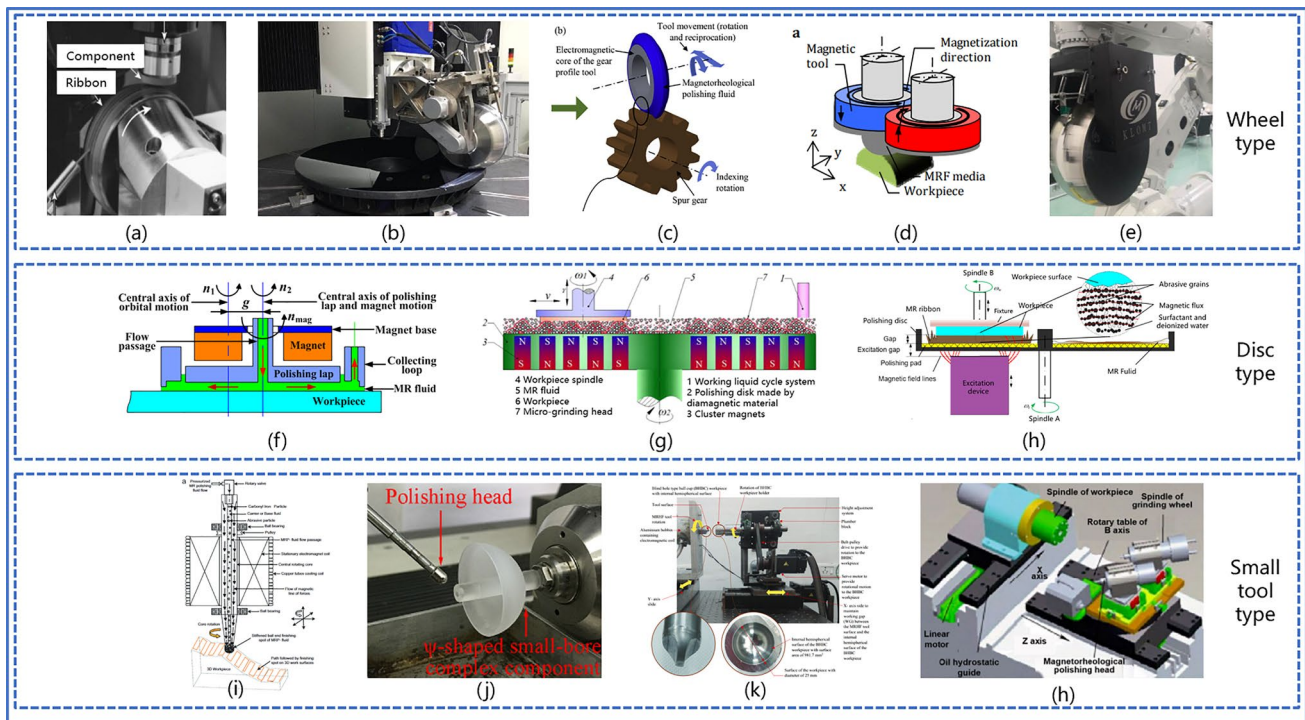


Fig. 18 Wheel type, disc type, and small tool type of MRF. **a** Wheel type with inverted structure [113]. **b** Wheel type with upright structure [132]. **c** Principle of magnetorheological gear profile finishing (MRGPF) machine [133]. **d** Principle of rapid MRF tech [131]. **e** Robot-assisted MRF device [135]. **f** Schematic diagram of lap MRF

[136]. **g** Schematic diagram of clustered MRF [137]. **h** MRF uses large polishing planes [138]. **i** Schematic diagram of BEMRF [139]. **j** Using BEMRF finishing hemispherical resonance gyroscope [140]. **k** Device of MRHF [141]. **l** Device of inclined-axis MRF technique [142]

of the excitation reset structure. They devised a lap-type MRF process (depicted in Fig. 18f). The surface shape error across the entire aperture range of $\Phi 350$ mm K9 glass was reduced from 25.236λ PV and 4.306λ RMS to 4.835λ PV and 0.683λ RMS. Yan et al. [137, 144] introduced a clustered MRF method, as illustrated in Fig. 18g. By utilizing optimized process parameters for a 30-min duration, they achieved a reduction in surface roughness: from Ra $0.34 \mu\text{m}$ to Ra 1.4 nm for K9 glass, from Ra 57.2 nm to Ra 4 nm for monocrystalline silicon, and from Ra 72.89 nm to Ra 1.92 nm for monocrystalline SiC. In all cases, nanoscale roughness surfaces were obtained. Yin et al. [138, 145] introduced a MRF technique utilizing large polishing mold planes, as depicted in Fig. 18h. After 60 min of polishing, the surface roughness of the K9 glass was reduced from Ra 127 nm to Ra 1 nm , while maintaining the face shape accuracy at PV 1 nm and achieving a surface roughness of Ra 0.6 nm .

The development of disc-type MRF primarily aims to improve polishing efficiency. Owing to the large size and flat shape of the polishing discs, this type of MRF is primarily employed for polishing flat components.

4.3.3 Small tool type

Singh et al. [139, 146] designed a ball-end magnetorheological finishing (BEMRF) device, depicted in Fig. 18i, capable of machining workpieces such as CNC ball-end milling cutters, particularly for grooves and complex surfaces, given the small size of the ball end. Zhang et al. [140] applied BEMRF technology to improve the surface roughness of the small-diameter complex structure of thin-walled parts in the hemispherical resonance gyroscope, as depicted in Fig. 18j. Aggarwal et al. [141] developed a novel electromagnetic-based magnetorheological hemispherical finishing (MRHF) tool, as shown in Fig. 18k, to achieve the fine-finishing requirements on the surface of the interior blind hole type ball cup (BHBC) workpiece. Subsequently, the roughness of the BHBC workpiece decreased from 0.310 to $0.070 \mu\text{m}$ after 80 min. Yin et al. [142, 147] introduced an inclined-axis MRF technique, as depicted in Fig. 18l, tailored for small-size components, and designed a compact aspherical ultra-precision composite machine tool. This machine tool achieved a shape accuracy of 221 nm and a roughness of 0.7 nm Ra for a $\Phi 6.6$ -mm aspheric carbide mold.

A variety of compact polishing tools can result in a smaller TIF, enhancing surface adaptability significantly, while concurrently reducing the efficiency of material removal. Due to the minimal size of the MRF tool, it is incapable of supporting a circulatory system for the magnetorheological fluids as efficiently as wheel or disc types.

Over prolonged use, this could cause the magnetorheological fluid to fail to precipitate, diminishing the predictability of the polishing process.

4.3.4 Other types

Ren et al. [148–150] introduced a belt-type MRF technology (shown in Fig. 19a) that utilizes a belt as a carrier for the magnetorheological fluid. They developed a specialized machine tool, named the belt MRF, which was used to process a 235-mm-diameter SiC planar mirror for 30 min, reducing the regional face shape error from PV = 0.396λ and RMS = 0.091λ to PV = 0.204λ and RMS = 0.020λ . Jain et al. [151, 152] introduced a rotational magnetorheological finishing (RMRF) process (as depicted in Fig. 19b) aimed at reducing the surface roughness of stainless steel components from Ra 260 to 110 nm and brass components from 240 to 50 nm . This was accomplished by employing a rotating magnetic field and hydraulic unit to induce a combined rotating and reciprocating motion of the polishing media. Liu et al. [153] introduced the magnetorheological precession finishing (MRPF) Technology (illustrated in Fig. 19c), which innovatively integrates MRF with bonnet precession polishing to produce a Gaussian-like TIF. This technology facilitated the uniform polishing of fused quartz surfaces, resulting in a significant reduction of Ra from $0.7 \mu\text{m}$ to 2.14 nm . Paswan et al. [154] devised an in situ rotary magnetorheological honing (RMRH) approach (as depicted in Fig. 17d) for the fine-finishing of the machined inner surfaces of cylindrical workpieces, resulting in a noteworthy reduction of the surface roughness from 510 to 60 nm .

The belt MRF replaces the polishing wheel with a belt and converts the D-type TIF to the T type, improving material removal efficiency for polishing large flat workpieces, although it exhibits poor adaptability on the polishing surface. MRPF applies the precession principle in BP to transform the D-shaped TIF into Gaussian-like TIF, overcoming the asymmetric problem of MRF. RMRF and RMRH are tailored for workpieces with hole characteristics and demonstrate effective polishing of commonly used industrial parts. However, considerations such as the circulation of MR fluid are still necessary.

4.4 Compound finishing methods

In the field of compound polishing technology, the use of electric or magnetic field assistance is dominant. Among these, MRF is often chosen as one of the compound polishing technologies due to its strong polishing determinacy, low tool requirements, high surface quality, and absence of SSD.

Zhang et al. [155–158] first proposed ultrasonic-magnetorheological compound finishing (UMRF) technology (illustrated in Fig. 20a). The method employs a rotating

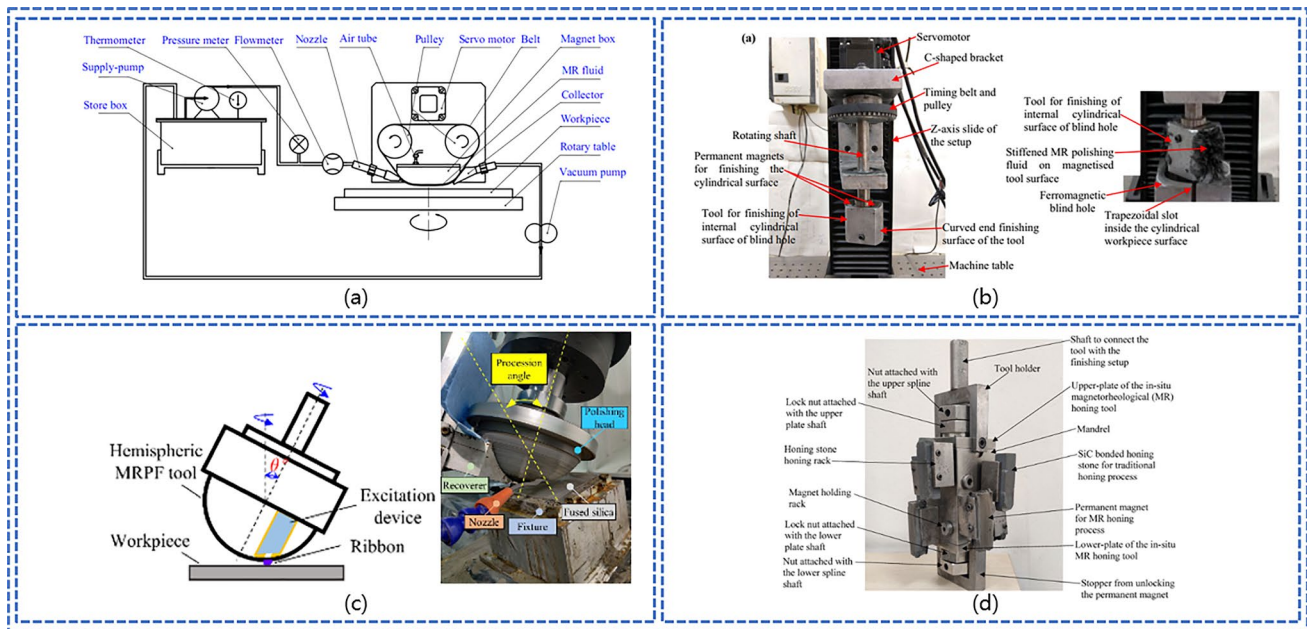


Fig. 19 Other MRF types. **a** Belt MRF principle [148]. **b** Equipment of R-MRAFF [152]. **c** Principle and machining process of MRPF [153]. **d** The device of RMRH [154]

small-diameter polishing tool head to machine concave, free-form optical elements with small curvature radius. By combining the advantages of MRF and ultrasonic polishing, the material removal distribution in a small area becomes more concentrated, thereby enhancing the polishing efficiency. In 2010, Jain et al. [159] introduced the chemo-mechanical MRF (CMMRF) technology (shown in Fig. 20b). Chemical–mechanical polishing (CMP) reactions are employed to enhance the polishing quality. Conversely, MRF fluids are utilized to manage the force magnitude on the workpiece, thus regulating the material removal rate (MRR) and mitigating surface integrity concerns. Ghai et al. [160] investigated the impact of process parameters on the CMMRF process, achieving a surface roughness reduction to Ra 0.597 nm. Liang et al. [161] conducted a study on cluster chemo-mechanical MRF applied to single-crystal SiC wafers, effectively controlling the surface roughness of the 2-in substrate to below Ra 0.1 nm. Tian et al. [162] introduced the electromagnetorheological finishing (ECMRF) method (illustrated in Fig. 20c) for polishing rigid-fragile materials. Experimental results corroborate that the synergistic application of electric and magnetic fields significantly enhances the effectiveness of the ECMRF technique compared to solely applying external electric or magnetic fields. Liu et al. [163] employed ECMRF for machining the 3D microstructure of hard-brittle materials. The machined microgroove exhibits an inverted trapezoidal shape, and the material removal mechanism observed in normal glass with this micromachining method

follows the plastic removal mode. Kordonski et al. [164] introduced the concept of magnetorheological jet polishing (MJP) and were responsible for the development of a fully functional five-axis MJP system. Zhang et al. [165, 166] built a MJP device and enhanced the W-shaped TIF to resemble a Gaussian shape during vertical polishing. Additionally, Cheng et al. proposed a weighted iterative algorithm and an extended surface to mitigate the influence of MSF error and edge effect in the existing process, resulting in an improvement of the surface PV from 0.220λ to 0.064λ , and a decrease in RMS from 0.047λ to 0.007λ [167, 168]. Sun et al. [169] utilized the magnetorheological shear thickening finishing (MRSTF) method (shown in Fig. 20e) with the designed finishing tool and developed MSTF media to finish a typical free-form surface (shown in Fig. 20d), specifically, the Sine surface. This resulted in the uniform removal of SUS304 material across the entire Sine surface, achieving over 87% improvement in surface roughness (Sa). Tian et al. [170] developed a material removal rate (MRR) model for the MRSTP process. This resulted in achieving a surface roughness (Sa) of 79.0 nm on aluminum 6061, representing a notable improvement of over 77%. Jha et al. [171] introduced the magnetorheological abrasive flow finishing (MRAFF) technology, which integrates MRF and AFM, and explained the mechanism. Subsequently, Jain et al. [151] introduced the rotational-magneto abrasive flow finishing (R-MRAFF) technique (shown in Fig. 20f). The R-MRAFF process achieved the best surface finish of 110 nm on stainless steel and 50 nm on brass workpieces.

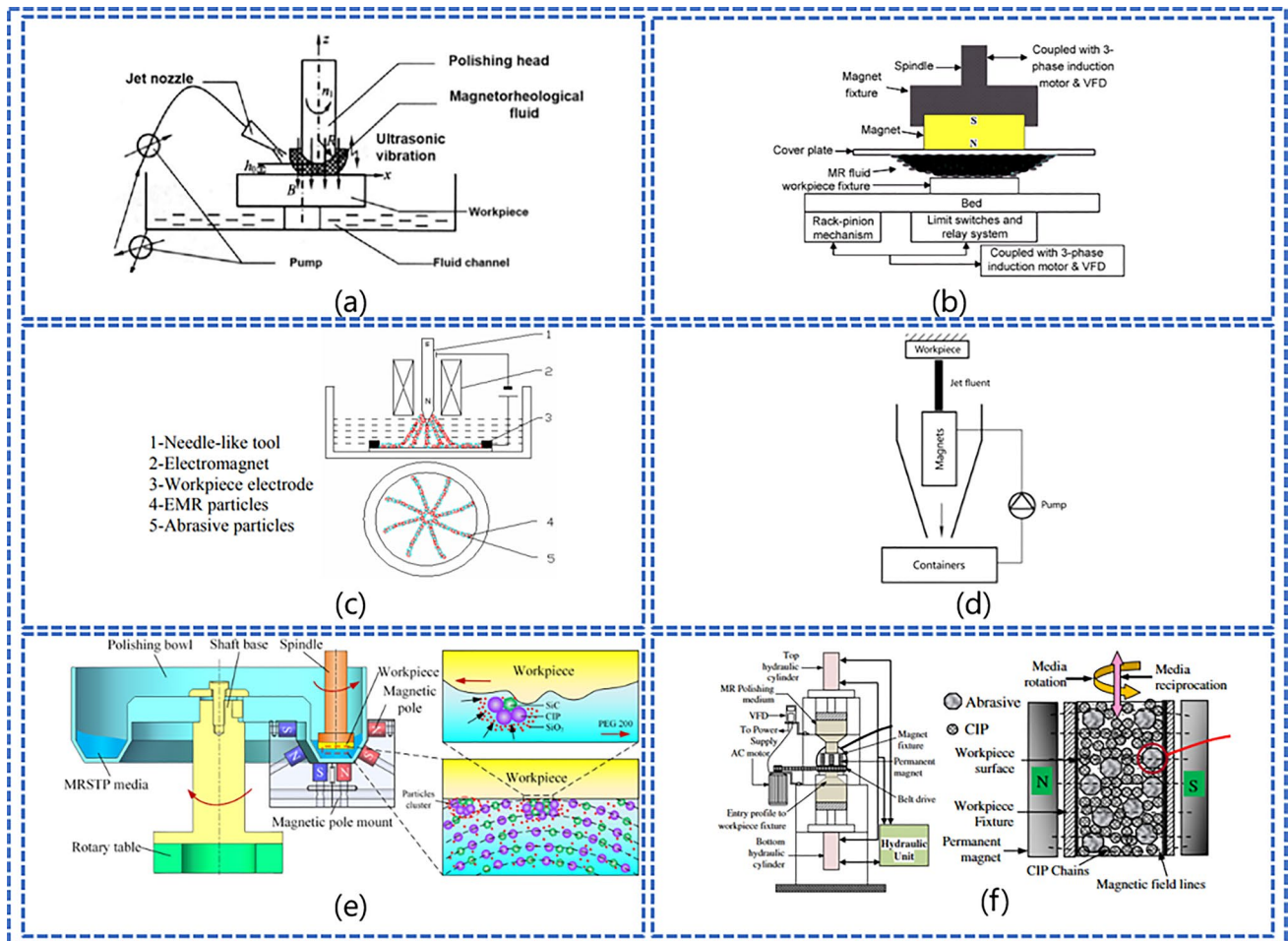


Fig. 20 Compound magnetorheological finishing methods. **a** Principle of UMRF [155]. **b** Principle of CMMRF [160]. **c** Principle of ECMRF [162]. **d** Principle of MJP method [165]. **e** Principle of MRSTF method [170]. **f** Device and principle of MRAFF technology [151]

4.5 Application of MRF

MRF technology exhibits low polishing efficiency but excels in trimming accuracy, making it a popular choice for shaping and refining optical components. The applications of MRF can be categorized into optical and non-optical domains, where optical applications encompass lenses, reflectors, and sensors, while non-optical applications span medical, semiconductor, and aerospace industries, as depicted in Fig. 21. In these domains, MRF is primarily employed for the final surface modification of components and for reducing surface roughness to ensure the components meet performance standards.

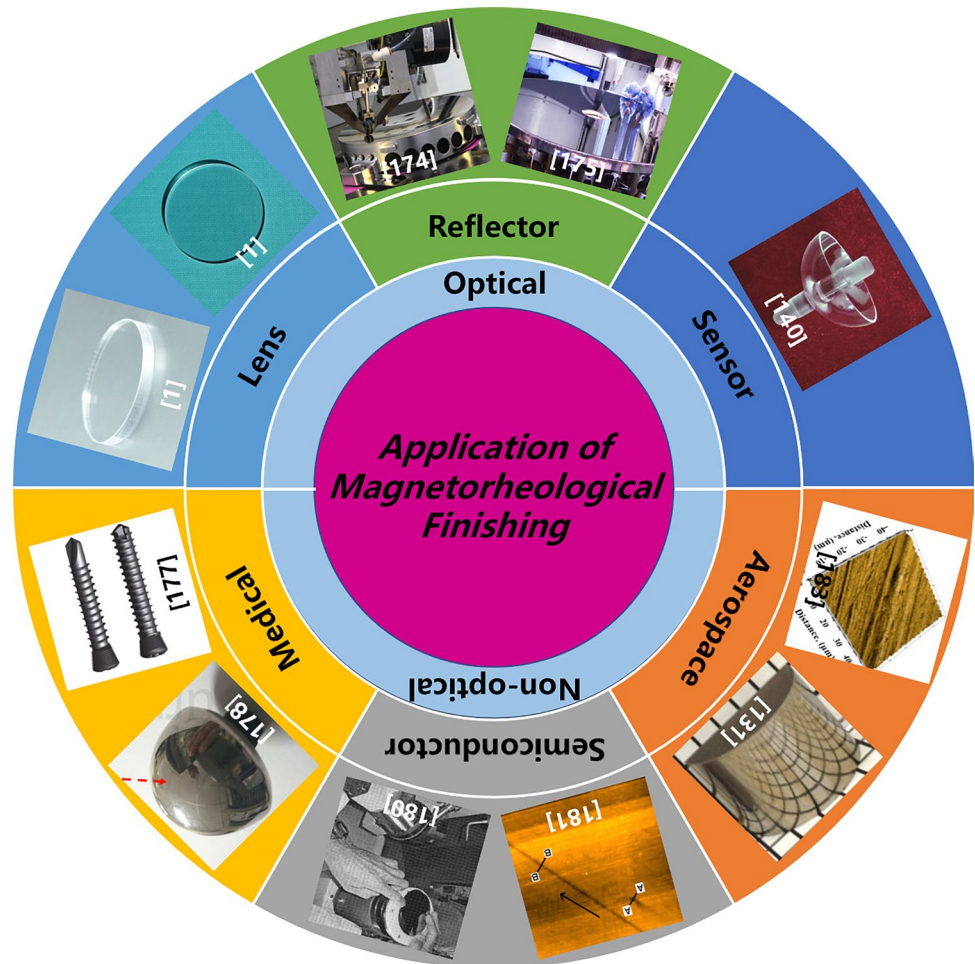
4.5.1 Optical

Guan [1] carried out lap MRF polishing experiments on the surface of $\Phi 350$ mm K9 glass. After a total of 3900 min of four iterations, the surface shape error in the entire aperture range converged from 25.236 λ PV, 4.306 λ RMS to 4.835 λ

PV, 0.683 λ RMS, which realized the rapid convergence of the LSF components of the surface shape error of K9 glass. Wang et al. [172] utilized the CMMRF method for processing sapphire glass, resulting in a significant polishing effect. The process achieved a maximum material removal rate of 4.63 mg/h, and the sapphire wafer was polished to achieve an ultra-smooth mirror state with an Ra of 0.3 nm.

In the realm of optical mirrors, in 2018, IOF [173] contributed to the upgrade of CRIRES in Chile. MRF technology was employed to rectify the shape of the aluminum mirror. Subsequently, CCOS smoothing was utilized to moderate the roughness to a range between RMS1 nm and RMS5 nm, ensuring shape deviation remained below RMS35 nm. IOF [174] utilized MRF for single-point diamond turning on the third mirror in the TMA system, achieving a shape deviation RMS of less than $\lambda/40$ nm. In 2018, the Changchun Institute of Optics, Fine Mechanics and Physics, Chinese Academy of Sciences, they made a substantial enhancement in the manufacturing accuracy and efficiency of the aspheric surface by employing the

Fig. 21 Application of MRF



combined processing technology of “stress disk” polishing and MRF. They successfully developed and received acceptance for the 4.03-m large-diameter silicon carbide mirror [175].

In addition to optical lenses, Chen et al. [176] applied the BEMRF method to refine the small-diameter complex structures of thin-walled parts in the hemispherical resonance gyroscope. This process successfully reduced the surface roughness from Ra 645.8 to Ra 18.7 nm, meeting the performance requirements of the workpiece.

4.5.2 Non-optical

MRF is frequently utilized for refining precision medical instruments. Ji et al. [177] introduced and developed a roller-type UMRF method and equipment, achieving a reduction in surface roughness of titanium alloy medical bone screws from 1.39 to 0.435 μm . Yan et al. [178] employed the cluster MRF technique to polish medical TC4 titanium alloy material, resulting in an ultra-smooth surface devoid of heterogeneous components. Prakash et al. [179] investigated the polishing

of medical β -phase Ti-Nb-Ta-Zr (β -TNTZ) alloy-based acetabular cups employing the magnetorheological fluid-assisted magnetic abrasive finishing (MRAF) technique, resulting in achieving a nearly Ra9nm smooth surface.

In the semiconductor industry, Arrasmith et al. [180] of COM initially applied the magnetorheological finishing technique on surface stress relief after grinding $\langle 1,1,1 \rangle$ silicon wafers with alumina abrasive, which effectively eliminated the residual stress on the surface of silicon wafers. Sidpara et al. [181] carried out a smooth and clean treatment on the surface of monocrystalline silicon blanks to reduce the surface roughness of silicon wafers from Ra 1600 nm to Ra 8 nm. Sun et al. [182] optimized the process parameters of the cluster magnetorheological technique to reduce the surface roughness of indium phosphide wafers to Ra 0.35 nm. They obtained a material removal rate of 2.5 $\mu\text{m}/\text{h}$.

For hard-to-cut metals, Sato et al. [131] employed a custom-made biaxial MRF testing apparatus to diminish the surface roughness of a 20 mm \times 20 mm flat component to approximately Ra 0.1 μm and a 25 mm \times 10 mm semi-cylindrical component to around Ra 0.2 μm . Parameswari

et al. [183] polished a disk-type Ti-6Al-4 V component with a diameter of $\phi 106.8$ mm employing a disk-based MRF method to reduce its surface roughness from an initial value of Ra 413 nm down to Ra 95 nm.

5 Key techniques of MRF

5.1 Modeling of TIF

Both the experimental and theoretical modeling methods assume that the radius of curvature of the workpiece is constant. Therefore, the TIF model becomes complex to represent the impact of curvature radius variations on the TIF [107]. Table 3 presents the TIFs studies conducted by various scholars on MRF.

Kordonski et al. [189, 190] pioneered the development of a mathematical model for the TIF in MRF, utilizing Preston’s equations to quantify the material removal rate and the applied shear force. Furthermore, the mathematical model accurately corresponds to the polishing spot profile obtained from polishing experiments. Shorey et al. [184] considered friction and shear forces in the finishing process, introduced the parameter C_p , modified Preston’s equation, and validated Golini and Kordonski’s concept that shear stress governs the removal rate of MRF material. Taking into account the incompressibility of the MR fluid, Zhang [24] omitted the impact of magnetostrictive pressure on the TIF stemming from the volume change in the magnetic field and developed a model for the TIF of MRF through the resolution of the fluid’s dynamic pressure and the magnetization pressure of the fluid. Peng [24, 191] posits that the MRF process is akin to bearing lubrication. Subsequently, a mathematical model for material removal in MRF was established based on Preston’s equation, which accounts for the positive pressure applied to the workpiece’s surface. Schinhaerl et al. [192]

devised an error-filtering algorithm for TIF measurements to mitigate the impact of measurement errors, yielding axially symmetric TIFs. Shi et al. [193] conducted theoretical analysis and numerical calculations to explore the nucleation state of the MR fluid within the polishing area under the influence of a gradient magnetic field. Additionally, they developed a three-dimensional mathematical model for material removal in MRF, focusing on the “shear as the primary factor and pressure as the secondary factor” mechanism. Schinhaerl et al. [185, 194] also developed a three-dimensional mathematical model of three different TIFs of magnetorheological finishing on concave (shown in Fig. 22a), convex, and planar workpieces. They explored the effects of various factors on the TIF of magnetorheological finishing. Song et al. [186] established a TIF prediction model for magnetorheological finishing. The TIF model efficiency coefficients are identified for different materials using the distribution of face shape errors before and after processing and the distribution of face shape residuals calculated by simulation. They then theoretically derived the calibration and prediction models for the magnetorheological finishing TIF and introduced the TIF efficiency coefficient to calibrate the TIF [195]. Ghosh et al. [187] investigated the effect of process parameters on the TIF in magnetorheological finishing of single-crystal silicon. The experimental results showed that the wheel speed contributes the most to the MRR and DDP of the TIF. Liu [188] proposed a new interactive regionalized modeling method of TIF for aspherical optical machining based on the regionalization of components and the solution of the nearest spherical radius, solving the problem that the TIF of aspherical and free-form surface components cannot be predicted accurately due to curvature effect. Subsequently, Liu [196] deeply analyzed the influence weights and mapping relationships of magnetorheological finishing process parameters on PRR, VRR, and polishing area, proposed the characteristic length coefficients as the evaluation indexes of

Table 3 Research on the MRF TIF

Author	TIF
Shorey et al. [184]	$\frac{dz}{dt} = C'_p \frac{\mu L}{A} \frac{ds}{dt} = C'_p \frac{F_D}{A} \frac{ds}{dt} = C'_p \tau \frac{ds}{dt}$
Peng et al. [24]	$r = k \cdot \left\{ \frac{3\phi\mu_0(\mu-\mu_0)}{\mu+2\mu_0} \int_0^H H dH + \frac{6\mu\mu_0\sqrt{2Rh_m}}{h_m^2} \left[\frac{\gamma_m}{2} + \frac{\sin 2\gamma_m}{4} - 1.22575 \times \left(\frac{3\gamma_m}{8} + \frac{3\pi}{16} + \frac{\sin 2\gamma_m}{4} + \frac{\sin 4\gamma_m}{32} + \frac{\pi}{4} \right) \right] \right\} \cdot v$
Schinhaerl et al. [185]	$RR(x, y) = \frac{1}{2} \cdot \left(\cos \left(\pi \cdot \frac{ y ^{knz}}{\frac{1}{2} \cdot \text{width}(x)} \right) + 1 \right) \cdot C_{XZ}(x) \cdot k_{RR}$
Song et al. [186]	$h(x, y) = \int_{\alpha} \int_{\beta} r(x - \alpha, y - \beta) \cdot d(\alpha, \beta) d\alpha d\beta + e(x, y)$
Ghosh et al. [187]	$MRR(\text{mm}^3/\text{min}) = 1.06085 - 0.000934N - 1.0975W - 0.00018NW + 0.00000073N^2 + 0.5192$
Liu et al. [188]	$dz(x, y) = K \cdot \left\{ \phi\mu_0\mu_f \frac{3(\mu_p-\mu_f)}{2(\mu_p+2\mu_f)} \left(\frac{\frac{B}{\mu_0}}{1+3\mu_f \frac{\mu_p-\mu_f}{\mu_p+2\mu_f}} \right)^2 + \frac{8R_1^2\eta_0 Vx(4y^2-B_p(x))}{(B_p(x)(2R_1h_0+x^2))^2} y \right\} \cdot V(x, y) \cdot dt$

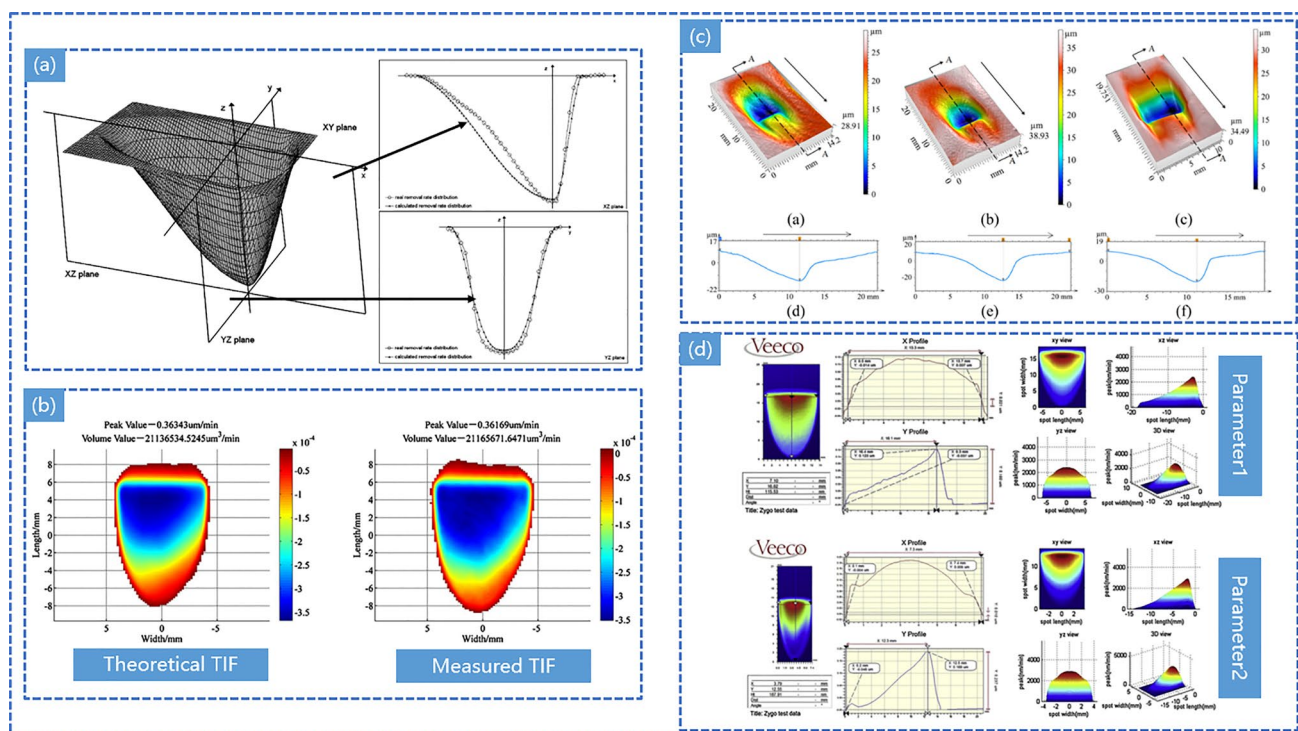


Fig. 22 **a** The three-dimensional and two-dimensional appearance of the MRF TIF [194]. **b** Comparison between theoretical TIF and measured TIF [195]. **c** Three-dimensional topography and the MRF

tool's cross-sectional shape influence the experiment parameters' function [187]. **d** Measured spots and theoretical spots in two different process parameters [188]

the removal characteristics, and verified the influence of the characteristic length coefficients and the processing trajectory on the uniform removal of the material.

When researchers established TIF theory and obtained TIF by experiments, they were based on the premise that the workpiece was a flat workpiece or a spherical element of equal curvature, and TIF could not reflect the influence of the workpiece curvature radius change on itself. Due to MRF's inferior surface adaptability compared to BP, it is essential to adjust the TIF of MRF based on varying curvature changes.

5.2 Optimization of magnetic field performance

The stability of the magnetic field dictates the stability of the magnetostrictive pressure, subsequently influencing the stability of the TIF. Additionally, the spatial distribution and excitation area of the magnetic field determine the volume of the TIF, consequently impacting the material removal rate.

In traditional wheel-type MRF research, Peng et al. analyzed the limitations of Zhang's [197] use of a permanent magnet magnetic circuit as a magnetic field generator for a MRF device. Zheng et al. [198] analyzed the impact of factors such as magnetic permeability of permeable material, saturation magnetic induction strength, air gap length, yoke cross-sectional area, pole shape, and others on the

distribution and strength of magnetic induction within the polished region. Regarding the excitation technology of the new MRF process, the primary objective is to enhance the excitation area in order to improve polishing efficiency. Nie et al. [199] examined the impact of magnet arrangement in the magnetic field generator on the polishing effect (shown in Fig. 23b), analyzed the correlation between magnet arrangement and flux density distribution, and optimized the magnetic field distribution in the polishing area by employing the six-way cross arrangement. Experimental verification demonstrated that small radius magnets yield improved flatness, whereas large radius magnets enhance polishing efficiency.

To enhance the material removal efficiency of MRF, it entails increasing the polishing area, enhancing the magnetic field intensity within the polishing area, and optimizing the magnetic field distribution. Guan et al. [135, 143] identified the optimal values for each key parameter of the permanent magnet unit. The magnetic field strength in the solid magnetic field area on the polishing disc surface reaches 0.35 T, enabling the MR fluid to form a stable ribbon (shown in Fig. 23a) that facilitates the removal of workpiece materials. The magnetic field strength in the center channel of the polishing disc's rotating axis and the weak magnetic field area on the disc's surface is less than 0.08 T, allowing the magnetorheological fluid to flow smoothly for cycle renewal.

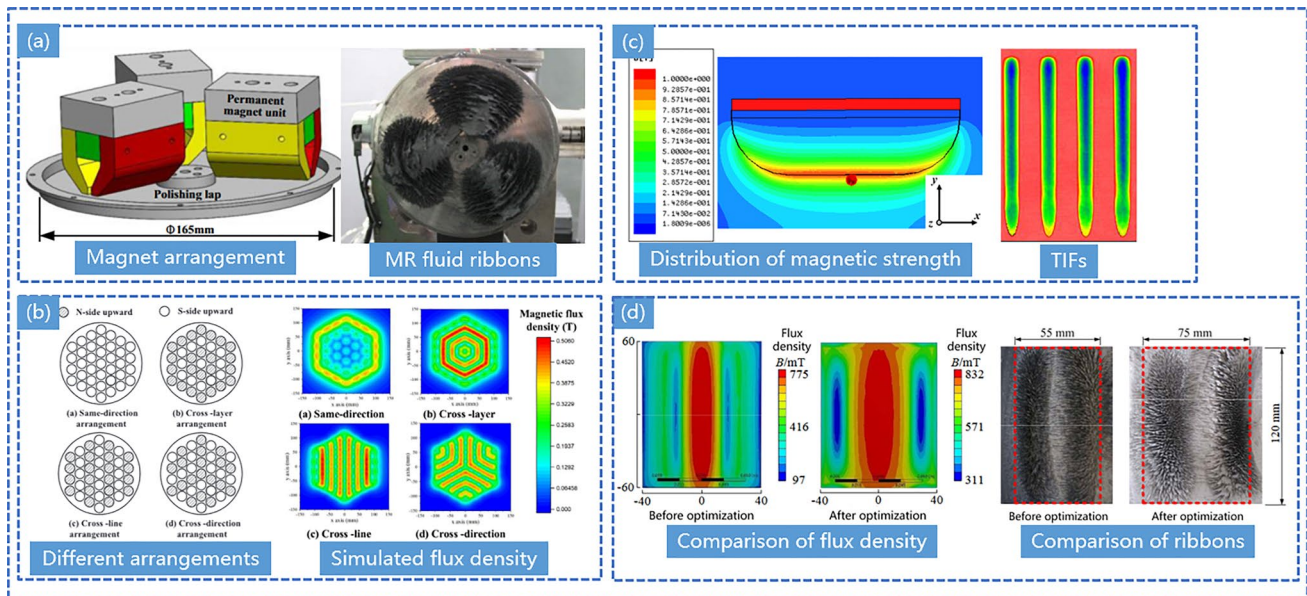


Fig. 23 Optimization of magnetic field performance in new type MRF. **a** Magnet arrangement and ribbons of lap MRF [143]. **b** Arrangements and simulated magnet flux density of cluster MRF

[199]. **c** Magnetic strength in belt MRF and its TIFs [150]. **d** Comparison of flux density and ribbons in MRF uses large polishing planes [172]

Lu et al. [200] designed four different types of magnetic field distribution in cluster MR fluid (MRF) and investigated their impact on material removal. The experimental results demonstrate that the axial magnetization isotropic arrangement and radial magnetization isotropic arrangement of the magnets can generate higher magnetic field strength and distribution. Wang et al. [150, 201] utilized boat-shaped permanent magnets made of strong magnetic material NdFe50 for the strip magnetorheological finishing (MRF) process, achieving an X-direction magnetic field strength exceeding 4000 Gauss (shown in Fig. 23c). Simulation and experimental verification confirmed the structural validity of the boat-shaped magnets, fulfilling the requirements for ribbon bump formation in MRF. As the magnetic flux density approaches and surpasses the saturation point, it disrupts the uniformity of magnetorheological shear stress distribution, resulting in inconsistent material removal. To address this issue, Wang [172] optimized and tested the permanent yoke excitation device, increasing the maximum flux density in the MR fluid by almost 60 mT and expanding the magnetic field by 22 mm (shown in Fig. 23d).

5.3 Fabrication of MR fluids

MR fluid has an essential influence on the efficiency and quality of MRF. MR fluid mainly comprises magnetic particles, base fluid, and additives. The magnetic particles mainly include γ -Fe₂O₃, Fe₂O₄, Fe₃O₄, Co Fe₂O₄, and Ni Fe₂O₄ alloy materials. The commonly used base fluids are mainly mineral oil, engine oil, synthetic oil, water, etc.; additives

include dispersants such as silicon dioxide and phosphate and anti-sedimentation agents such as polymer and hydrophilic silicone resin oligomer [132, 202].

An effective MR fluid should exhibit low viscosity at zero magnetic fields, excellent anti-settling stability, re-dispersion capability, high shear yield stress, rapid dynamic response, broad working range, and environmental friendliness [203]. The fabrication process of magnetorheological (MR) fluids is depicted in Fig. 24a. MR fluids are characterized by three primary properties: stability, magnetic properties, and rheological properties.

MR fluid stability primarily pertains to sedimentation stability, which involves the ability of MR fluid to resist settling and maintain uniform suspension within the fluid [205]. Particles in MR fluid tend to agglomerate after settling, significantly impacting the fluid's performance. Kordonski et al. [206] investigated the influence of magnet particle size and content on sedimentation stability. The sedimentation velocity of MR fluid shows a linear correlation with the size of magnet particles, with smaller particles leading to enhanced sedimentation stability. Han et al. [204] modified the material composition of the MR fluid by incorporating Fe₃O₄ particles and hexadecyl trimethyl ammonium bromide as surfactants. Additionally, they introduced SiO₂/Fe₃O₄ nanoparticles to produce MR fluid with improved sedimentation stability. Guo et al. [207] prepared MR fluids using carbonyl iron powder as magnetic particles and nano-silica particles with varying specific surface areas as thixotropic agents. Their study investigated the impact of varying the specific surface areas of silica on the rheological properties and

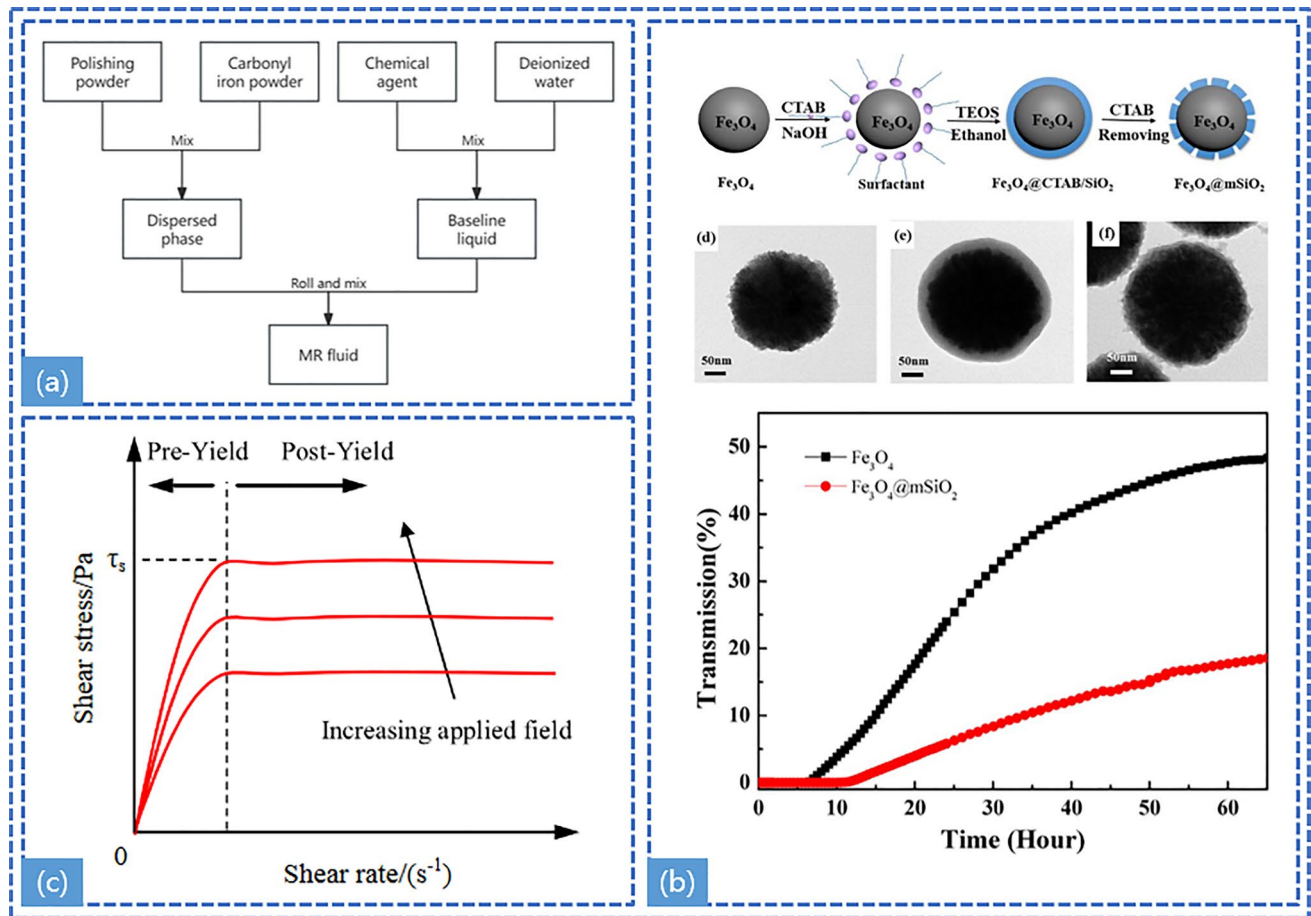


Fig. 24 **a** Fabrication process of MR fluid [203]. **b** Microstructure of SiO_2 and Fe_3O_4 nanoparticles and the sedimentation stability comparison [204]. **c** Rheological properties of magnetorheological fluids under shear action [203]

sedimentation stability of the MR fluids. It was observed that larger surface areas of silica molecules correspond to improved rheological properties and sedimentation stability.

The term “magnetic properties” denotes the phenomenon of magnetization exhibited by MR fluid in response to an external magnetic field, wherein the fluid’s magnetization varies with the applied magnetic field [25]. This factor significantly influences the properties of the flexible polishing mold in MRF. Kordonski et al. [208]. discovered that the magnetic susceptibility of MR fluid exhibits a linear rise with the increase in volume fraction and tends to increase with larger particle diameters. Lopez [209] observed that MR fluid can exhibit superparamagnetic behavior when the magnetic particle size is in the nano-scale range (8 to 10 nm). Achieving reversible control of material properties requires the particles to exhibit enhanced soft magnetic properties. This ensures that upon removal of the external magnetic field, the material’s mechanical properties revert to their original state without the influence of the magnetic field. This criterion significantly affects the stability and magnetic properties of

MR fluids, as particles would otherwise exert attractive forces within the liquid matrix [210, 211].

The rheology of magnetorheological fluid refers to the magnetorheological fluid that hardens under the action of a strong external magnetic field, which has properties similar to the “solid” state. Rheology is reversible, removes the external magnetic field and the magnetorheological fluid back to a liquid with good fluidity [25]. Currently, domestic and foreign researchers and scholars of magnetorheological fluids macroscopic description of the following models: the Bingham plasticity model, the generalized Bingham model, the Herschel-Bulkley rheological model, viscous model and Eyring model [176, 212], and the highest acceptance of the Bingham plasticity model. The controllability of the magnetorheological fluid is reflected in the controllability of the yield stress, which can be controlled by controlling the magnetic field strength B and the magnetorheological fluid temperature T to control the shear rate and, thus, the yield stress. When the shear rate is low, the shear stress of the magnetorheological fluid is less than its yield stress;

magnetorheological in the macroscopic pre-yield stage, yield stress with the increase in shear rate increases significantly magnetorheological fluid for a solid-like movement; when the shear rate to rise to a specific value, the shear stress exceeds the yield stress; the yield stress rate of change has become very slow, into the yielding stage, magnetorheological fluid with zero magnetic fields when the viscosity flow.

5.4 Control on edge effect

Due to the different rotation direction of the polishing wheel driving the magnetorheological fluid and the truncation of the magnetorheological fluid when flowing through the edge of the component, the distribution of fluid dynamic pressure at the edge of the workpiece is different from that in the non-edge region, and magnetorheological finishing also has specific edge effects, as shown in Fig. 25.

In the leading state, the TIF is partially missing because the workpiece truncates the front side of the ribbon; in the trailing state, the TIF is also missing because there is no element support under part of the ribbon [213].

Li et al. [214] compared the measured edge TIF to the ideal complete TIF and found that the trailing state does not cause the loss of MR fluid compared to the Leading state. The change in material removal rate is insignificant for the trailing state, whereas the leading state shows a significant change in material removal rate for MRF. The shape RMS has converged to 0.014λ by modifying the dwell time at edge position, which is shown in Fig. 26b. By conducting a thorough analysis of the stability of the MRF edge TIF and refining the edge algorithm to account for dwell time, Zhong et al. [215] introduced a novel approach to mitigate edge influence during MRF. Experimental findings demonstrate that the edge error zone can be effectively limited to less than 1.5 mm (shown in Fig. 26c). Jeon et al. [216] conducted an analysis of the edge TIF in the leading and trailing states. They integrated various edge TIFs with different truncation distances and polishing parameters, and introduced a novel mathematical model for forecasting the edge effects following MRFs. This model predicted edge effects with an error margin of 4–7% from the experimental actual value.

Comparison between the predicted edge and the measured edge in leading region and trailing edge is shown in Fig. 26d.

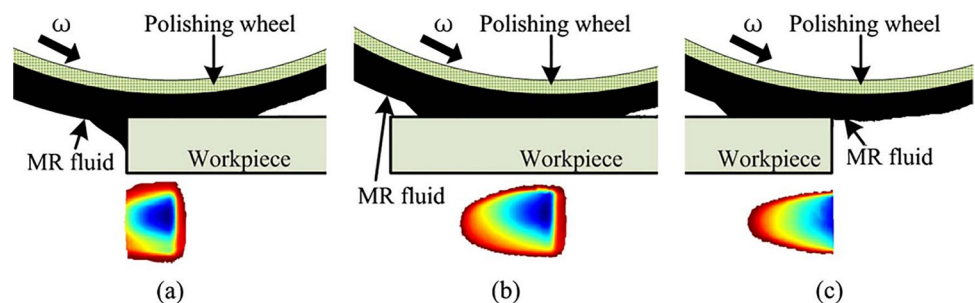
It is necessary to start from the essence of MRF, analyze in detail the formation mechanism and evolutionary law of edge effects, and establish effective methods and techniques for controlling edge effects. MRF employs similar methods to control edge effects, which share principles akin to the Tool-Lift method. Nevertheless, the non-central symmetry of MRF TIF requires consideration of its pose's impact on the edge effect during control. Additionally, optimizing the polishing path for distinct edge characteristics is imperative to explore their synergistic effects.

5.5 Control on MSF error

MSF errors in MRF primarily arise from the dwell time algorithm, while the surface shape error is minimized using a TIF in the edge region of the optical surface. This phenomenon is referred to as the ringing effect of MRF.

QED [217] proposed a multi-step polishing process, initially utilizing large-diameter MRF for material removal, eliminating the abrasive damage layer and mitigating the LSF error. Afterwards, CCOS small tool polishing is employed to rectify the middle and HSF errors along with the edge effects. Lastly, small-diameter MRF is utilized to refine the surface shape. Yang et al. [218] suggested randomizing the raster path step size as a means to mitigate the MSF. They substantiated the efficacy of this random line spacing approach in mitigating MSF errors in MRF through simulations. Li [214] employed the use of conformal extension to mitigate the MSF oscillation-ringing effect caused by the dwell time algorithm in MRF. This approach addresses the spatially periodic face shape error in the edge region of the optical surface, approximately in the size of the TIF. The RMS value was decreased from 6.4 to 1.46 nm through virtual machining of a ϕ 100-mm planar component, as shown in Fig. 27a. Hou et al. [219] conducted a theoretical analysis of the primary factors influencing the MSF error in raster path processing. They determined that, within the established TIF, the removal depth of a single scan and the finishing distance significantly impact the

Fig. 25 Schematic drawing of the MR fluid flow state [213]. **a** At the leading edge, **b** away from edges, and **c** at the trailing edge



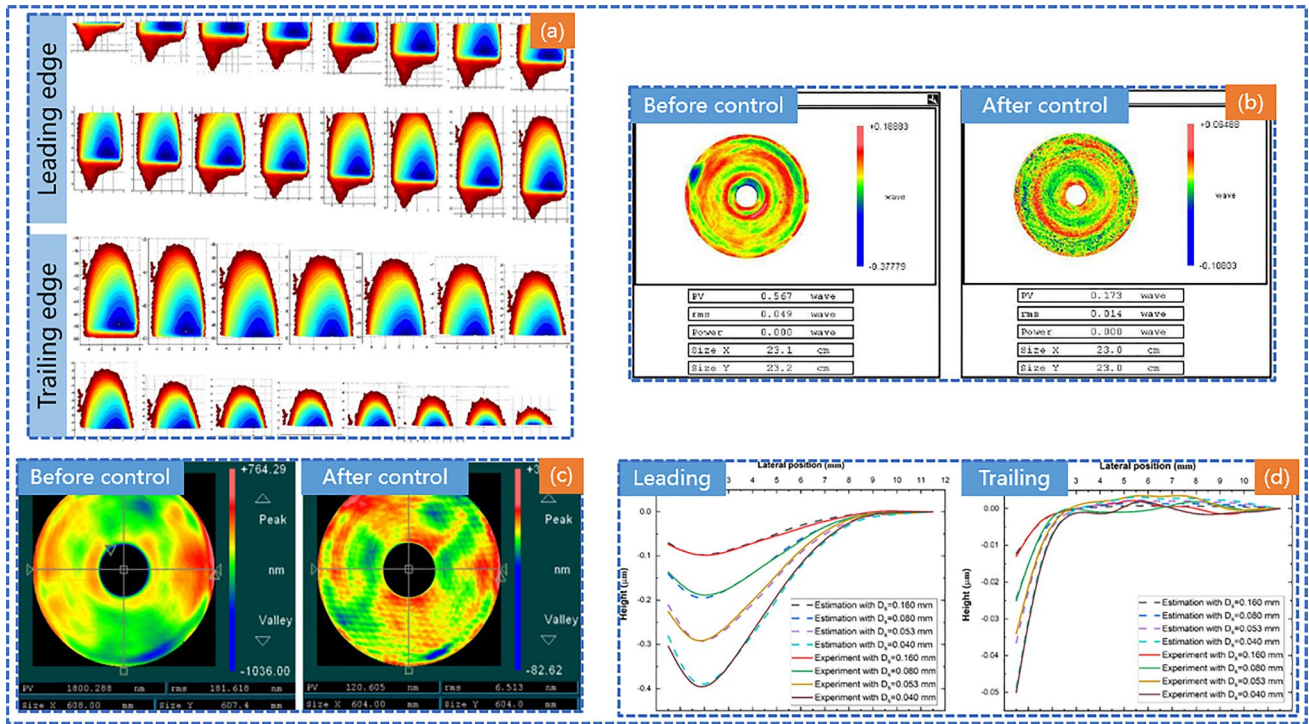


Fig. 26 Edge control results. **a** Ideal MRF TIFs at leading edge and trailing edge [213]. **b** Shape accuracy before edge control and after [214]. **c** Original surface error and residual error in edge controlling

experiment [215]. **d** Comparison between the predicted edge and the measured edge in leading region and trailing edge [216]

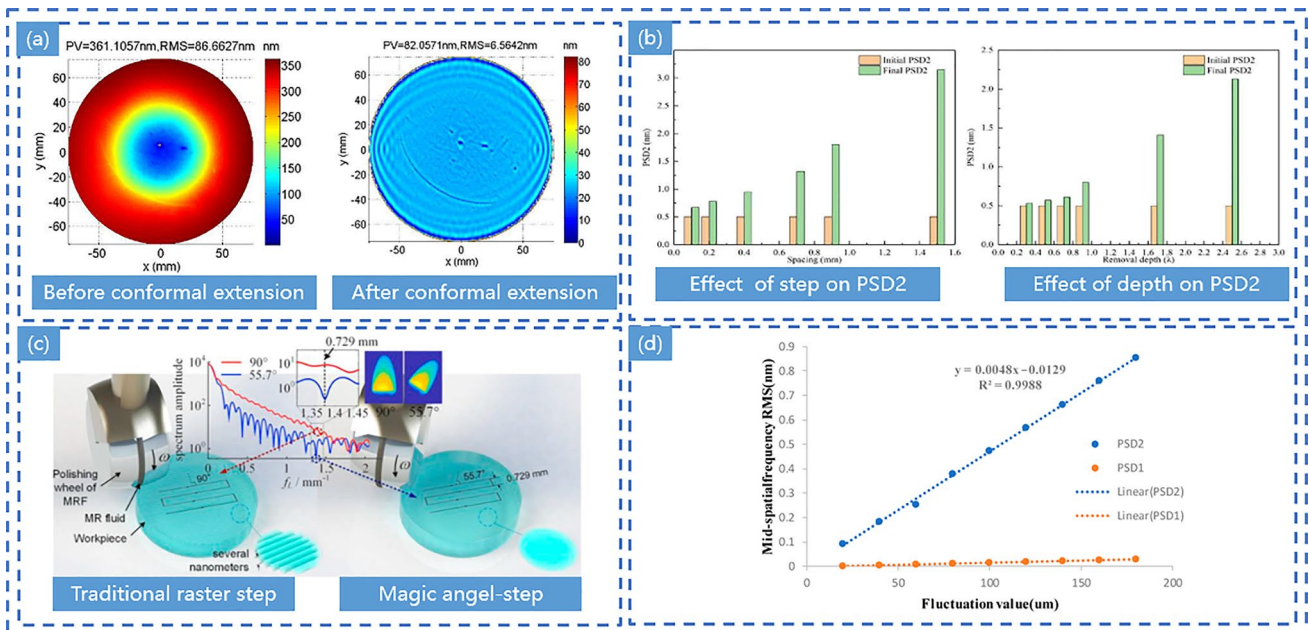


Fig. 27 **a** Comparison of surface error distribution before and after conformal extension [214]. **b** The influence curves of the removal depth and processing spacing on the PSD2 in a single scan [219]. **c** Schematic of a typical MRF processing mode in the traditional 90°

path and magic angle step MRF processing mode [220]. **d** Effects of different ribbon fluctuations on PSD1 and PSD2 in the MSF band [221]

finishing process. Subsequently, they derived the optimal parameters for the removal depth of a single scan and the processing distance under specific process conditions in the MRF process, utilizing a 1-nm MSF error as the evaluation criterion (shown in Fig. 27b). Wan et al. [220] modified the angle between the polishing wheel rotation and the raster path in MRF. While the traditional process employs a 90° angle, they implemented a “magic angle step state” of 55.7°–60.5° (illustrated in Fig. 27c), and conducted a series of process tests. The experimental results demonstrate effective suppression of the MSF error by the MRF tool, reducing it from 0.009λ to 0.006λ. Additionally, the power spectral density curve corresponding to the magic angle step state no longer exhibits significant oscillations. Wang et al. [221, 222] explored the impact of magnetorheological ribbon fluctuations in MRF on the MSF error of machined components, and the potential for mitigating the MSF error on the component surface by manipulating the rotation angle of the TIF and the ribbon fluctuations. The experimental findings demonstrate that changes in the magnetorheological flow, induced by the rotation of the centrifugal pump in the MR fluid circulation system, lead to ribbon fluctuations. As ribbon fluctuation increases, the RMS value of the spatial frequency PSD2 on the machined surface progressively rises (shown in Fig. 27d). Moreover, optimal surface accuracy with PV 2.791 nm and RMS 0.355 nm is achieved with the TIF rotated by 74°, a raster step size of 0.5 mm, and a moving speed of 300 mm/min.

5.6 Path planning

Because BP and MRF both belong to CCOS, their trajectory planning principles are identical. Notably, in the use of BP for figuring, the precession process is commonly employed, resulting in an approximately centrally symmetrical Gaussian-shaped TIF, while the TIF of MRF is asymmetrical and D-shaped. Consequently, during MRF trajectory planning, one should take into account the rotation angle of MRF TIF on the component, such as the “magic angle step” mentioned in the preceding section.

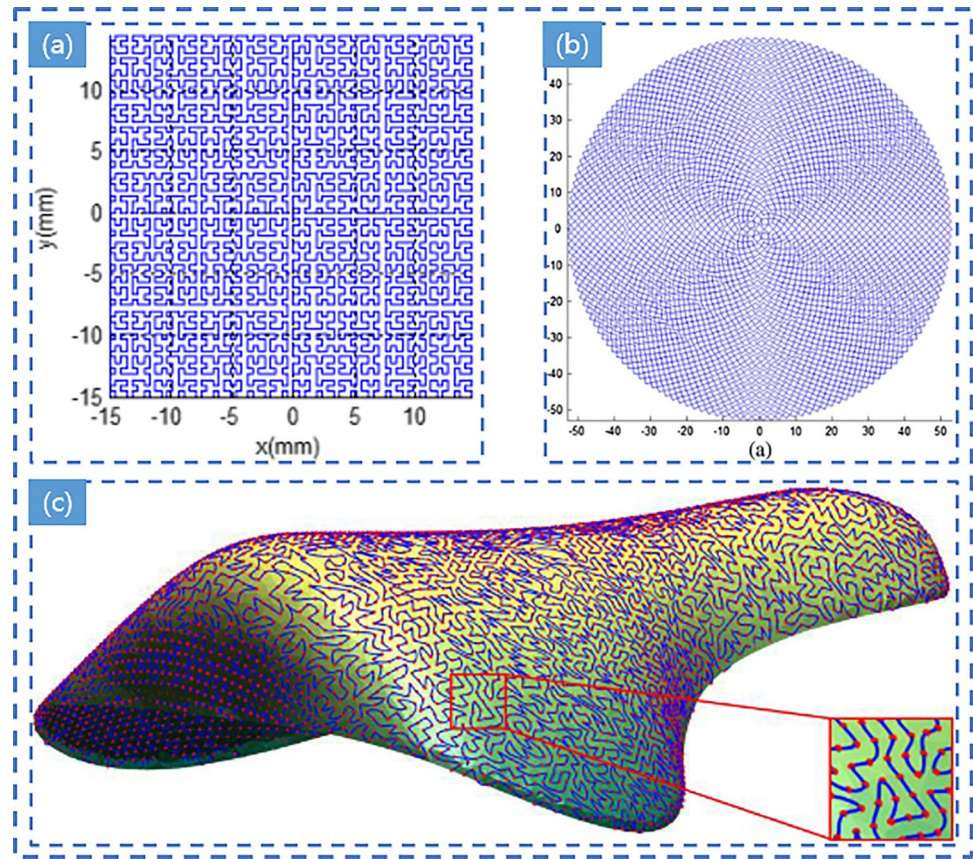
Dai et al. [223] devised a random polishing path utilizing the maximum entropy method. The experimental findings demonstrated significantly lower MSF error in the partially randomized region compared to the area employing a conventional grating path. Subsequent to one MRF iteration lasting 7.46 min, the PV measures 0.062λ, and the RMS value amounts to 0.010λ, and the amplitude and smoothness of the PSD curve have been significantly improved. Yu et al. [224] devised a tool path algorithm rooted in fractal geometry (shown in Fig. 28a), utilizing the mesh’s intersection points as directly connected endpoints of the polyline. The dwell time of each segment is denoted by the average dwell times of the two endpoints. Subsequently, a comprehensive set of

surface error data was simulated with precise parameters, applying both spiral and fractal paths with an equal number of nodes. The comparative analysis demonstrates that the majority of error results favor the fractal path over the spiral path. Hon et al. [99] proposed the construction of Peano paths (shown in Fig. 28b) to achieve uniform coverage of aspherical elements, which is well suited to the MRF process. These paths are comprised of evenly distributed short line segments and arcs across the entire surface, with each path segment being orthogonal to its neighboring line segments. The trajectory was employed for polishing Φ 100-mm BK7 glass using MRF, resulting in convergence of PV and RMS from 0.386λ and 0.056λ to 0.097λ and 0.011λ, respectively (shown in Fig. 28b). Supranowitz et al. [225] from QED introduced a novel spiral polishing trajectory designed for polishing surfaces including inclined planes, wedge-shaped (non-centered) spherical surfaces, off-axis parabolas, free-form surfaces, and other surfaces characterized by circular features but lacking rotational symmetry. Wang et al. [226] introduced a mesh surface pseudo-random path planning method utilizing the matrix angle-based flattening (MABF) algorithm to mitigate the MSF and HSF errors during the polishing of free-form surfaces (shown in Fig. 28c). The method comprises pseudo-random path planning in the parameterized plane, path inverse mapping, and NURBS smoothing processing.

6 Summary and prospect

Upon review of existing literature, it is apparent that previous examinations of BP and MRF predominantly focus on outlining the fundamental principles, equipment, and applications, lacking a comprehensive review of the key technologies corresponding to these methods. Therefore, it is imperative to systematically summarize various aspects encompassing the technology’s origins, principles, equipment, applications, TIF modeling, suppression of edge effects, alleviation of MSF errors, and path planning. This paper aims to initially expound upon the irreplaceable advantages offered by both compliant polishing methods—BP and MRF. Notably, these methods are capable of efficient sub-surface damage removal with high confidence and precise component modification, making them well suited for mass production due to their cost-effectiveness. Subsequent to this, a foundational overview of both techniques is presented, covering their development history, principles, equipment, and applications. This is followed by an examination of the progress in key technologies associated with BP and MRF, facilitating rapid comprehension and mastery of the theoretical underpinnings and current research status. Furthermore, this review serves as a valuable resource for guiding researchers in identifying potential areas for further exploration in more detailed studies:

Fig. 28 **a** Schematic diagram of fractal path [224]. **b** Peano-like MRF path [99]. **c** The pseudo-random path based MABF on a bicycle seat after NURBS smoothing [226]



1. Further in-depth study of the material removal mechanism of BP. Mainstream research on the material removal mechanism of BP has mainly focused on macroscopic aspects, such as the TIF, while overlooking microscopic aspects. Although some scholars have begun examining the interaction between individual abrasive grains and various minute forces on the materials, the corrosive impact of the cerium oxide polishing solution on the components has been disregarded. Hence, there is a need to explore the synergistic interplay between the mechanical removal of abrasive grains and the chemical corrosion induced by the polishing solution on material removal, in order to develop a profound understanding of the material removal process and its governing principles.
2. Further in-depth study of the suppression method of the edge effect of BP. The conventional deterministic polishing dwell time algorithms exhibit lower precision at component edges. Additionally, BP, which relies on material removal via normal pressure of abrasive grains, alters the stress state of the component at the edges, leading to increased pressure in both normal and tangential directions and distortion of the TIF. Consequently, rectifying dwell time determination at the element edge and optimizing the machining process at the edge are essential. This approach aims to synergistically mitigate the edge effect on the dwell time and TIF.
3. The polishing pad on the bonnet tool head's surface is prone to wear, leading to decreased stability of its TIF, hindering its ability to rectify MSF error residuals, and complicating the control process. Therefore, there is a need to develop and investigate trimming tools and processes for the bonnet tool head to ensure robust stability of the TIF. Moreover, the potential use of polishing media like non-Newtonian fluids in BP technology warrants exploration to achieve long-lasting wear resistance of the polishing tools.
4. Further in-depth study of methods to improve the material removal rate of MRF. MRF relies on lower fluid shear stress for material removal, so its material removal rate is lower than other sub-aperture polishing techniques. Hence, it is essential to investigate the modulation mechanism of mechanical, physical, and chemical interactions at the surface interface of the magnetorheological polished workpiece to elucidate the material removal mechanism of MRF. Furthermore, integrating the multi-field-assisted polishing theory is imperative to modify the polishing behavior mechanism while ensuring the stability of the TIF, thus improving the material removal rate comprehensively.

5. Further in-depth study of MRF in MSF error suppression methods. The existing evidence demonstrates that MRF is proficient in effectively mitigating or rectifying the residual IF error from prior processes. However, as MRF is commonly employed as the final polishing process for the component, its distinctive D-shaped TIF in the grating and helix paths after iteration tends to introduce a narrower spatial band of IF error residuals. Therefore, there is a need to investigate the mechanism underlying the IF error in the MRF process, and its progression to enhance the existing IF error dwell time algorithm, processing path planning strategy, and control process.
6. The currently available MR fluid in the market exhibits significantly inferior performance compared to QED's production, yet an optimal magnetorheological TIF necessitates a high-performance MR fluid as its foundation. Hence, there is a need to prepare and optimize MR fluid with low zero-field viscosity and superior anti-settling and rheological properties to enhance the comprehensive performance of MRF.
7. More extensive industrial production attempts have been carried out. Within the realm of CCOS, STP, IBF, and FJP are prevalent. The joint promotion of efficient and rapid material removal in BP with the high-precision figuring in MRF should be encouraged to broaden and enhance the cost-effectiveness of engineering applications.

Author contribution All authors contributed to the review conception and design. The first and final draft of the manuscript was written by Huiming Feng. Yunfeng Peng reviewed the manuscript critically, and all authors commented on previous versions of the manuscript. All authors read and approved the final manuscript.

Funding This work was supported by the National Natural Science Foundation of China (No. 52075463), Shenzhen Science & Technology Program (No. JCYJ20210324122001003), Fujian Provincial Science and Technology Program (No.2021H6008), and Hunan Province Key Research and Development Program (No. 2023GK2069).

Declarations

Conflict of interest The authors declare no competing interests.

References

1. Guan F (2018) Research on key techniques of lap magnetorheological finishing. Dissertation, National University of Defense Technology, Changsha, China (In Chinese)
2. Moses EI (2003) The National Ignition Facility: the world's largest laser. In: Proceedings of the 20th IEEE/NPSS Symposium on Fusion Engineering 2003. IEEE, Piscataway, pp 413–418. <https://doi.org/10.1109/FUSION.2003.1426672>
3. Moses EI (2010) Advances in inertial confinement fusion at the National Ignition Facility (NIF). *Fusion Eng Des* 85(7):983–986. <https://doi.org/10.1016/j.fusengdes.2009.11.006>
4. Campbell J, Hawley-Fedder R, Stolz C, Menapace J, Borden M, Whitman P, Yu J, Runkel M, Riley M, Feit M, Hackel R (2004) NIF optical materials and fabrication technologies: an overview. *Proc SPIE* 5341:84–101. <https://doi.org/10.1117/12.538471>
5. Miller G, Moses E, Wuest C (2004) The National Ignition Facility: enabling fusion ignition for the 21st century. *Nucl Fusion* 44(12):S228–S238. <https://doi.org/10.1088/0029-5515/44/12/S14>
6. Cao C (2004) Study on ultra-precision continuous polishing of large aperture optical components. Dissertation, Sichuan University, Chengdu, China (In Chinese)
7. Zheng WG, Wei XF, Zhu QH, Jing F, Hu DX, Zhang XM, Su JQ, Zheng KX, Wang CC, Yuan XD, Zhou H, Chen B, Wang J, Xu Q, Yang LM, Dai WJ, Zhou W, Wang F, Xu DP, Xie XD, Feng B, Peng ZT, Guo LF, Chen YB, Zhang XJ, Liu LQ, Lin DH, Dang Z, Xiang Y, Chen XD, Zhang WY (2016) SG-III laser facility has successfully achieved 60 TW/180 kJ ultraviolet laser (351 nm) output. *High Power Laser Part Beams* 28(1):019901. <https://doi.org/10.11884/HPLPB201628.019901>. (In Chinese)
8. Extremely Large Telescope (2024). <http://www.eelt.org.uk/>. Accessed 24 Feb 2024
9. Ramsay S, Odorico SD, Casali M, González JC, Hubin N, Kasper M, Käuff HU, Kissler-Patig M, Marchetti E, Paufigue J, Pasquini L, Siebenmorgen R, Richichi A, Vernet J, Zerbi FM (2010) An overview of the E-ELT instrumentation programme. *Proc SPIE* 7735:773524. <https://doi.org/10.1117/12.857037>
10. Webb Space Telescope (2024). <http://jwst.nasa.gov/>. Accessed 24 Feb 2024
11. Clampin M (2014) Recent progress with the JWST Observatory. *Proc SPIE* 9143:914302. <https://doi.org/10.1117/12.2057537>
12. Lowisch M, Kuerz P, Conradi O, Wittich G, Seitz W, Kaiser W (2013) Optics for ASML's NXE:3300B platform. *Proc SPIE* 8679:86791H. <https://doi.org/10.1117/12.2012158>
13. Kurz P, Mann HJ, Antoni M, Singer W, Muhlbeier M, Melzer F, Dinger U, Weiser M, Stacklies S, Seitz G, Haidl F, Sohmen E, Kaiser W (2000) Optics for EUV lithography. In: Proceedings of the 2000 International Microprocesses and Nanotechnology Conference. IEEE, Piscataway, p 264. <https://doi.org/10.1109/IMNC.2000.872750>
14. Cheng H, Dong Z, Ye X, Tam HY (2014) Subsurface damages of fused silica developed during deterministic small tool polishing. *Opt Express* 22(15):18588–18603. <https://doi.org/10.1364/OE.22.018588>
15. Liu HT (2014) Kev technique computer controlled active lap in fabrication of large aspherics. Dissertation, Institute of Optics And Electronics, Chinese Academy of Sciences, Chengdu, China (In Chinese)
16. Peng XQ, Yang C, Hu H, Dai YF (2017) Measurement and algorithm for localization of aspheric lens in magnetorheological finishing. *Int J Adv Manuf Technol* 88(9):2889–2897. <https://doi.org/10.1007/s00170-016-9001-x>
17. Beaucamp A, Katsuura T, Kawara Z (2017) A novel ultrasonic cavitation assisted fluid jet polishing system. *CIRP Ann Manuf Technol* 66(1):301–304. <https://doi.org/10.1016/j.cirp.2017.04.083>
18. Wang CJ, Cheung CF, Ho LT, Liu MY, Lee WB (2017) A novel multi-jet polishing process and tool for high-efficiency polishing. *Int J Mach Tools Manuf* 115:60–73. <https://doi.org/10.1016/j.ijmactools.2016.12.006>
19. Bauer J, Frost F, Arnold T (2017) Reactive ion beam figuring of optical aluminium surfaces. *J Phys D Appl Phys* 50(8):085101. <https://doi.org/10.1088/1361-6463/50/8/085101>
20. Wang CJ (2015) Research on high efficiency polishing on large size optics using a semirigid bonnet. Dissertation, Xiamen University, Xiamen, China (In Chinese)

21. Pan R (2014) Research on high efficiency and controllable bonnet polishing technology for large aspheric surface. Dissertation, Xiamen University, Xiamen, China (In Chinese)
22. Jiang T (2015) Research on the mid spatial frequency error control technology of large-diameter high-efficiency bonnet polishing. Dissertation, Xiamen University, Xiamen, China (In Chinese)
23. Zhang F, Zhang XJ, Yu JC, Wang QD, Guo PJ (2000) Foundation of mathematics model of magnetorheological finishing. *Opt Tech* 26(2):190–192. <https://doi.org/10.13741/j.cnki.11-1879/o4.2000.02.032>. (In Chinese)
24. Peng XQ, Dai YF, Li SY (2004) Material removal model of magnetorheological finishing. *J Mech Eng* 40(4):67–70. <https://doi.org/10.3321/j.issn:0577-6686.2004.04.013>. (In Chinese)
25. Zhang F (2000) Study on technique of magnetorheological finishing. Dissertation, Changchun Institute of Optics, Fine Mechanics and Physics, Chinese Academy of Sciences, Changchun, China (In Chinese)
26. Peng XQ (2004) Study on the key techniques of deterministic magnetorheological finishing. Dissertation, National University of Defense Technology, Changsha, China (In Chinese)
27. Zhu WL, Beaucamp A (2020) Compliant grinding and polishing: a review. *Int J Mach Tools Manuf* 158:103634. <https://doi.org/10.1016/j.ijmactools.2020.103634>
28. Peng Y, Shen B, Wang Z, Yang P, Yang W, Bi G (2021) Review on polishing technology of small-scale aspheric optics. *Int J Adv Manuf Technol* 115(4):965–987. <https://doi.org/10.1007/s00170-021-07202-3>
29. Wu Z, Shen J, Peng Y, Wu X (2022) Review on ultra-precision bonnet polishing technology. *Int J Adv Manuf Technol* 121(5):2901–2921. <https://doi.org/10.1007/s00170-022-09501-9>
30. Wang W, Ji S, Zhao J (2023) Review of magnetorheological finishing on components with complex surfaces. *Int J Adv Manuf Technol*. <https://doi.org/10.1007/s00170-023-11611-x>
31. Bingham R, Walker D, Kim DH, Brooks D, Freeman R, Riley D (2000) Novel automated process for aspheric surfaces. *Proc SPIE* 4093:445–450. <https://doi.org/10.1117/12.405237>
32. Walker D, Brooks D, Freeman R, King A, Mccavana G, Morton R, Riley D, Simms J (2001) First aspheric form and texture results from a production machine embodying the precession process. *Proc SPIE* 4451:267–276. <https://doi.org/10.1117/12.453652>
33. Walker D, Freeman R, Mccavana G, Morton R, Riley D, Simms J, Brooks D, Kim E, King A (2002) Zeeko/UCL process for polishing large lenses and prisms. *Proc SPIE* 4411:106–111. <https://doi.org/10.1117/12.454877>
34. Walker DD, Brooks D, King A, Freeman R, Morton R, Mccavana G, Kim SW (2003) The ‘Precessions’ tooling for polishing and figuring flat, spherical and aspheric surfaces. *Opt Express* 11(8):958–964. <https://doi.org/10.1364/OE.11.000958>
35. Walker D, Yu G, Li H, Messelink W, Evans R, Beaucamp A (2012) Edges in CNC polishing: from mirror-segments towards semiconductors, paper 1: edges on processing the global surface. *Opt Express* 20(18):19787–19798. <https://doi.org/10.1364/OE.20.019787>
36. Li H, Walker D, Yu G, Sayle A, Messelink W, Evans R, Beaucamp A (2013) Edge control in CNC polishing, paper 2: simulation and validation of tool influence functions on edges. *Opt Express* 21(1):370–381. <https://doi.org/10.1364/OE.21.000370>
37. Charlton P (2011) The application of Zeeko polishing technology to freeform femoral knee replacement component manufacture. Dissertation, University of Huddersfield, Huddersfield
38. Zeng S, Blunt L (2014) An experimental study on the correlation of polishing force and material removal for bonnet polishing of cobalt chrome alloy. *Int J Adv Manuf Technol* 73(1):185–193. <https://doi.org/10.1007/s00170-014-5801-z>
39. Gao B, Xie DG, Yao YX, Yuan ZJ (2004) New technology of ballonet tool for polishing. *Opt Tech* 30(3):333–336. <https://doi.org/10.3321/j.issn:1002-1582.2004.03.002>. (In Chinese)
40. Song JF (2009) Research on the optimization of the process parameters and its correlative technology in bonnet polishing the curved optical parts. Dissertation, Harbin Institute of Technology, Harbin, China (In Chinese)
41. Beaucamp A, Namba Y (2013) Super-smooth finishing of diamond turned hard X-ray molding dies by combined fluid jet and bonnet polishing. *CIRP Ann* 62(1):315–318. <https://doi.org/10.1016/j.cirp.2013.03.010>
42. Su X, Ji P, Jin Y, Li D, Walker D, Yu G, Li H, Wang B (2019) Simulation and experimental study on form-preserving capability of bonnet polishing for complex freeform surfaces. *Precis Eng* 60:54–62. <https://doi.org/10.1016/j.precisioneng.2019.07.010>
43. Zhang W, Li HY, Yu GY (2009) Current situation of ultra-precision bonnet polishing key technology of optical elements. *Acta Opt Sin* 29(1):27–34. <https://doi.org/10.3788/aos20092901.0027>. (In Chinese)
44. Walker D, Beaucamp A, Bingham R, Brooks D, Freeman R, Kim S, King A, Mccavana G, Morton R, Riley D, Simms J (2003) Precessions process for efficient production of aspheric optics for large telescopes and their instrumentation. *Proc SPIE* 4842:73–84. <https://doi.org/10.1117/12.456677>
45. Gao B, Yao YX, Xie DG, Yuan ZJ (2006) Movement modeling and simulation of precession mechanisms for bonnet tool polishing. *J Mech Eng* 42(2):101–104. <https://doi.org/10.3321/j.issn:0577-6686.2006.02.019>. (In Chinese)
46. Ji SM, Ao HP, Jin MS, Zhang L, Zeng X, Ding JJ (2012) Experiment research of mould curved surface of gasbag polishing based on optimizing the contact characteristics. *J Mech Electr Eng* 29(12):1367–1370, 1375 (In Chinese)
47. Guo YB, Peng YF, Wang ZZ, Bi G, Yang W, Yang P (2018) Development and application of precision grinding/polishing and measurement equipment for large-size optical components. *Aeronaut Manuf Technol* 61(6):26–35. <https://doi.org/10.16080/j.issn1671-833x.2018.06.026>. (In Chinese)
48. He JK (2023) Research on key technologies of magnetorheological precession polishing processing. Dissertation, Xiamen University, Xiamen, China (In Chinese)
49. Walker D, Beaucamp ATH, Doubrovski V, Dunn C, Freeman R, Mccavana G, Morton R, Riley D, Simms J, Wei X (2005) New results extending the Precessions process to smoothing ground aspheres and producing freeform parts. *Proc SPIE* 5869:58690E. <https://doi.org/10.1117/12.617067>
50. Gao B, Yao YX, Xie DG, Yuan ZJ, Liu Y (2004) Development and property test of bonnet polishing tool. *Mod Manuf Eng* 27(10):52–54. <https://doi.org/10.16731/j.cnki.1671-3133.2004.10.023>. (In Chinese)
51. Jin MS (2009) Gasbag polishing mechanism and process on free-form surface mould. Dissertation, Zhejiang University of Technology, Hangzhou, China (In Chinese)
52. Yu G, Li H, Walker D (2011) Removal of mid spatial-frequency features in mirror segments. *J Eur Opt Soc-Rapid Publ* 6:11044. <https://doi.org/10.2971/jeos.2011.11044>
53. Yu G, Walker D, Li H (2012) Implementing a grolishing process in Zeeko IRP machines. *Appl Opt* 51(27):6637–6640. <https://doi.org/10.1364/AO.51.006637>
54. Beaucamp A, Namba Y, Combrinck H, Charlton P, Freeman R (2014) Shape adaptive grinding of CVD silicon carbide. *CIRP Ann* 63(1):317–320. <https://doi.org/10.1016/j.cirp.2014.03.019>
55. Beaucamp A, Simon P, Charlton P, King C, Matsubara A, Wegener K (2017) Brittle-ductile transition in shape adaptive grinding (SAG) of SiC aspheric optics. *Int J Mach Tools Manuf* 115:29–37. <https://doi.org/10.1016/j.ijmactools.2016.11.006>

56. Wang C, Wang Z, Wang Q, Ke X, Zhong B, Guo Y, Xu Q (2017) Improved semirigid bonnet tool for high-efficiency polishing on large aspheric optics. *Int J Adv Manuf Technol* 88(5):1607–1617. <https://doi.org/10.1007/s00170-016-8901-0>
57. Wang C, Yang W, Wang Z, Yang X, Sun Z, Zhong B, Pan R, Yang P, Guo Y, Xu Q (2014) Highly efficient deterministic polishing using a semirigid bonnet. *Opt Eng* 53(9):095102. <https://doi.org/10.1117/1.OE.53.9.095102>
58. Kong L (2016) Technology research on silicone bonnet elastic polishing. Dissertation, Changchun University of Science and Technology, Changchun, China (In Chinese)
59. Zhu WL, Beaucamp A (2020) Non-Newtonian fluid based contactless sub-aperture polishing. *CIRP Ann* 69(1):293–296. <https://doi.org/10.1016/j.cirp.2020.04.093>
60. Huang X, Wang Z, Li L (2023) Study on the impact of positioning errors on the process performance of robotic bonnet polishing. *Int J Precis Eng Manuf* 24(9):1587–1598. <https://doi.org/10.1007/s12541-023-00882-9>
61. Pan R, Hu C, Xie Y, Fan J, Wang Z, Liu Z (2024) Study on optimization of process parameters in dressing of bonnet polishing tool. *Proc Inst Mech Eng Part B J Eng Manuf* 238(1–2):187–198. <https://doi.org/10.1177/09544054221150663>
62. Walker D, Beaucamp A, Brooks D, Doubrovski V, Cassie M, Dunn C, Freeman R, King A, Libert M, Mccavana G, Morton R, Riley D, Simms J (2004) New results from the Precessions polishing process scaled to larger sizes. *Proc SPIE* 5494:71–80. <https://doi.org/10.1117/12.553044>
63. Beaucamp A, Namba Y, Inasaki I, Combrinck H, Freeman R (2011) Finishing of optical moulds to $\lambda/20$ by automated corrective polishing. *CIRP Ann* 60(1):375–378. <https://doi.org/10.1016/j.cirp.2011.03.110>
64. Cheung CF, Kong LB, Ho LT, To S (2011) Modelling and simulation of structure surface generation using computer controlled ultra-precision polishing. *Precis Eng* 35(4):574–590. <https://doi.org/10.1016/j.precisioneng.2011.04.001>
65. Walker D, Beaucamp A, Dunn C, Freeman R, Marek A, Mccavana G, Morton R, Riley D (2004) First results on free-form polishing using the Precessions process. In: *Proceedings of ASPE Winter Topical Meeting: Freeform Optics, Design, Fabrication, Metrology, Assembly*. ASPE, Raleigh, pp 29–34
66. Beaucamp A, Namba Y, Charlton P (2014) Corrective finishing of extreme ultraviolet photomask blanks by precessed bonnet polisher. *Appl Opt* 53(14):3075–3080. <https://doi.org/10.1364/AO.53.003075>
67. Zhu WL, Anthony B (2020) Investigation of critical material removal transitions in compliant machining of brittle ceramics. *Mater Des* 185:108258. <https://doi.org/10.1016/j.matdes.2019.108258>
68. Yuan JL, Wu Z, Lv BH, Ruan DN, Lu HZ, Zhao P (2012) Review on ultra-precision polishing technology of aspheric surface. *J Mech Eng* 48(23):167–177. <https://doi.org/10.3901/jme.2012.23.167>. (In Chinese)
69. Li C, Piao Y, Zhang F, Zhang Y, Hu Y, Wang Y (2023) Understand anisotropy dependence of damage evolution and material removal during nanoscratch of MgF_2 single crystals. *Int J Extreme Manuf* 5(1):015101. <https://doi.org/10.1088/2631-7990/ac9eed>
70. Li C, Piao Y, Meng B, Hu Y, Li L, Zhang F (2022) Phase transition and plastic deformation mechanisms induced by self-rotating grinding of GaN single crystals. *Int J Mach Tools Manuf* 172:103827. <https://doi.org/10.1016/j.ijmactools.2021.103827>
71. Kim DW, Kim SW (2005) Static tool influence function for fabrication simulation of hexagonal mirror segments for extremely large telescopes. *Opt Express* 13(3):910–917. <https://doi.org/10.1364/OPEX.13.000910>
72. Cao ZC, Cheung CF (2016) Multi-scale modeling and simulation of material removal characteristics in computer-controlled bonnet polishing. *Int J Mech Sci* 106:147–156. <https://doi.org/10.1016/j.ijmecs.2015.12.011>
73. Pan R, Zhong B, Chen D, Wang Z, Fan J, Zhang C, Wei S (2018) Modification of tool influence function of bonnet polishing based on interfacial friction coefficient. *Int J Mach Tools Manuf* 124:43–52. <https://doi.org/10.1016/j.ijmactools.2017.09.003>
74. Shi C, Peng Y, Hou L, Wang Z, Guo Y (2018) Micro-analysis model for material removal mechanisms of bonnet polishing. *Appl Opt* 57(11):2861–2872. <https://doi.org/10.1364/AO.57.002861>
75. Walker D, Beaucamp A, Bingham R, Brooks D, Freeman R, Kim S, King A, Mccavana G, Morton R, Riley D, Simms J (2004) Precessions aspheric polishing: new results from the development program. *Proc SPIE* 5180:15–28. <https://doi.org/10.1117/12.507462>
76. Walker D, Beaucamp A, Brooks D, Doubrovski V, Cassie M, Dunn C, Freeman R, King A, Libert M, Mccavana G, Morton R, Riley D, Simms J (2004) Recent developments of Precessions polishing for larger components and free-form surfaces. *Proc SPIE* 5523:281–289. <https://doi.org/10.1117/12.559531>
77. Kim DW, Kim SW, Burge JH (2009) Non-sequential optimization technique for a computer controlled optical surfacing process using multiple tool influence functions. *Opt Express* 17(24):21850–21866. <https://doi.org/10.1364/OE.17.021850>
78. Jin M, Ji S, Zhang L, Yuan Q, Zhang X, Zhang Y (2008) Material removal model and contact control of robotic gasbag polishing technique. In: *Proceedings of the 2008 IEEE Conference on Robotics, Automation and Mechatronics*. IEEE, Piscataway, pp 879–883
79. Wang C, Wang Z, Yang X, Sun Z, Peng Y, Guo Y, Xu Q (2014) Modeling of the static tool influence function of bonnet polishing based on FEA. *Int J Adv Manuf Technol* 74(1):341–349. <https://doi.org/10.1007/s00170-014-6004-3>
80. Wang CJ, Guo YB, Wang ZZ, Pan R, Xie YH (2013) Dynamic removal function modeling of bonnet tool polishing on optics elements. *J Mech Eng* 49(17):19–25. <https://doi.org/10.3901/jme.2013.17.019>. (In Chinese)
81. Wan S, He X, Zhang X, Xu M (2016) Effect of feed velocity change on amount of material removal for free abrasive polishing with sub-aperture pad. *Proc SPIE* 10154:1015401. <https://doi.org/10.1117/12.2243430>
82. Zhong B, Wang C, Chen X, Wang J (2019) Time-varying tool influence function model of bonnet polishing for aspheric surfaces. *Appl Opt* 58(4):1101–1109. <https://doi.org/10.1364/AO.58.001101>
83. Han Y, Zhu WL, Zhang L, Beaucamp A (2020) Region adaptive scheduling for time-dependent processes with optimal use of machine dynamics. *Int J Mach Tools Manuf* 156:103589. <https://doi.org/10.1016/j.ijmactools.2020.103589>
84. Yang L (2001) *Advanced optical fabrication technologies*. Science Press, Beijing, China (In Chinese)
85. Li H, Zhang W, Walker D, Yu G (2014) Active edge control in the precessions polishing process for manufacturing large mirror segments. *Proc SPIE* 9280:928007. <https://doi.org/10.1117/12.2069790>
86. Walker D, Beaucamp A, Dunn C, Evans R, Freeman R, Morton R, Wei S, Yu G (2008) Active control of edges and global microstructure on segmented mirrors. *Proc SPIE* 7018:701812. <https://doi.org/10.1117/12.787930>
87. Wang W, Xu M, Yu G (2010) Research on edge control in the process of polishing using ultra precise bonnet on optical elements. *Proc SPIE* 7654:76540N. <https://doi.org/10.1117/12.866699>

88. Ke X, Qiu L, Wang C, Wang Z (2020) Tentative investigations on reducing the edge effects in pre-polishing the optics. *Appl Sci* 10(15):5286. <https://doi.org/10.3390/app10155286>
89. Yin L, Hu H, Guan C, Dai Y, Li Z (2021) Edge control in the computer-controlled optical surface. *Micromachines* 12(10):1154. <https://doi.org/10.3390/mi12101154>
90. Walker D, Baldwin A, Evans R, Freeman R, Hamidi S, Shore P, Tonnellier X, Wei S, Williams C, Yu G (2007) A quantitative comparison of three grolishing techniques for the Precessions process. *Proc SPIE* 6671:66711H. <https://doi.org/10.1117/12.735488>
91. Zhong B, Chen XH, Li J, Wen ZJ (2018) Effect of precession mode on the surface error of optical components in bonnet polishing. *Proc SPIE* 10847:1084707. <https://doi.org/10.1117/12.2503980>
92. Huang WR, Tsai TY, Lin YJ, Kuo CH, Yu ZR, Ho CF, Hsu WY, Young HT (2020) Experimental investigation of mid-spatial frequency surface textures on fused silica after computer numerical control bonnet polishing. *Int J Adv Manuf Technol* 108(5):1367–1380. <https://doi.org/10.1007/s00170-020-05388-6>
93. Rao M, Zhang Y, Wang H, Ming H, Zhao Y, Zhu J (2023) Towards modeling and restraining surface ripples during bonnet polishing based on frequency domain characteristic control. *CIRP Ann* 72(1):493–496. <https://doi.org/10.1016/j.cirp.2023.04.079>
94. Zhang L, Han Y, Fan C, Tang Y, Song X (2017) Polishing path planning for physically uniform overlap of polishing ribbons on freeform surface. *Int J Adv Manuf Technol* 92(9):4525–4541. <https://doi.org/10.1007/s00170-017-0466-z>
95. Cho U, Eom D, Lee D, Park J (1992) A flexible polishing robot system for die and mould. In: *Proceedings of the 23rd International Symposium on Industrial Robots*. pp 449–456
96. Pessoles X, Tournier C (2009) Automatic polishing process of plastic injection molds on a 5-axis milling center. *J Mater Process Technol* 209(7):3665–3673. <https://doi.org/10.1016/j.jmatprotec.2008.08.034>
97. Tsai MJ, Huang JF (2006) Efficient automatic polishing process with a new compliant abrasive tool. *Int J Adv Manuf Technol* 30(9):817–827. <https://doi.org/10.1007/s00170-005-0126-6>
98. Mizugaki Y, Sakamoto M, Sata T (1992) Fractal path generation for a metal-mold polishing robot system and its evaluation by the operability. *CIRP Ann* 41(1):531–534. [https://doi.org/10.1016/S0007-8506\(07\)61261-X](https://doi.org/10.1016/S0007-8506(07)61261-X)
99. Tam HY, Cheng H, Dong Z (2013) Peano-like paths for sub-aperture polishing of optical aspherical surfaces. *Appl Opt* 52(15):3624–3636. <https://doi.org/10.1364/AO.52.003624>
100. Dong Z, Cheng H, Tam HY (2014) Further investigations on fixed abrasive diamond pellets used for diminishing mid-spatial frequency errors of optical mirrors. *Appl Opt* 53(3):327–334. <https://doi.org/10.1364/AO.53.000327>
101. Dunn CR, Walker DD (2008) Pseudo-random tool paths for CNC sub-aperture polishing and other applications. *Opt Express* 16(23):18942–18949. <https://doi.org/10.1364/OE.16.018942>
102. Takizawa K, Beaucamp A (2017) Comparison of tool feed influence in CNC polishing between a novel circular-random path and other pseudo-random paths. *Opt Express* 25(19):22411–22424. <https://doi.org/10.1364/OE.25.022411>
103. Zhao Q, Zhang L, Fan C (2019) Six-directional pseudorandom consecutive unicursal polishing path for suppressing mid-spatial frequency error and realizing consecutive uniform coverage. *Appl Opt* 58(31):8529–8541. <https://doi.org/10.1364/AO.58.008529>
104. Dunn C, Walker DD, Beaucamp A, Kelchner J, Freeman R (2008) Improving surface PSD using a random tool path. In: *Optical Fabrication and Testing 2008*. Optica Publishing Group, Washington, DC, p OThB5
105. Zhang LP, Yang H, Bao LX, Li J (2014) Optimization of dwell time algorithm for precession bonnet polishing. *Opt Precis Eng* 22(12):3303–3309. <https://doi.org/10.3788/ope.20142212.3303>. (In Chinese)
106. Wang W (2020) Study on removal function and algorithm of bonnet figuring for X-ray focusing mirror mold. Dissertation, Harbin Institute of Technology, Harbin, China (In Chinese)
107. Li QS, Cheng Y, Cai FZ, Feng ZJ, Zhang BP (1999) Dwell time algorithm in computer controlled optical surfacing. *Opt Tech* 25(3):57–60, 63. <https://doi.org/10.3321/j.issn:1002-1582.1999.03.004> (In Chinese)
108. Han Y, Wu F, Wan YJ (2009) Dwell time algorithms for computer controlled optical surfacing technology. In: *Proceedings of the 2009 Advanced Optical Technology and Its Applications Symposium*. Photoelectronic Technology Professional Committee, Chinese Society Astronautics, Beijing, pp 73–76 (In Chinese)
109. Wang C, Yang W, Wang Z, Yang X, Hu C, Zhong B, Guo Y, Xu Q (2014) Dwell-time algorithm for polishing large optics. *Appl Opt* 53(21):4752–4760. <https://doi.org/10.1364/AO.53.004752>
110. Zhang YF, Wang Y, Wang YJ, He JG, Ji F (2010) Dwell time algorithm based on optimization theory for magnetorheological finishing. *J Appl Opt* 31(4):657–662. <https://doi.org/10.3969/j.issn.1002-2082.2010.04.031>. (In Chinese)
111. Lee S (2018) Modeling and experimental investigation for the removal function of silicon-based material related on the temperature effect using APPP (Atmospheric pressure plasma polishing). Dissertation, Harbin Institute of Technology, Harbin, China (In Chinese)
112. Zhang L, Zhao Q, Fan C (2021) Dwell time algorithm in deterministic polishing of a free-form surface based on the continuous tool influence function. *Appl Opt* 60(9):2704–2715. <https://doi.org/10.1364/AO.418409>
113. Su YT, Hung TC, Horng CC (2000) An experimental study on tool wear of hydrodynamic polishing process. *Wear* 246(1):117–129. [https://doi.org/10.1016/S0043-1648\(00\)00497-X](https://doi.org/10.1016/S0043-1648(00)00497-X)
114. Park K, Oh J, Jeong H (2008) Pad characterization and experimental analysis of pad wear effect on material removal uniformity in chemical mechanical polishing. *Jpn J Appl Phys* 47(10):7812–7817. <https://doi.org/10.1143/JJAP.47.7812>
115. Belkhir N, Bouzid D, Herold V (2012) Morphological behavior and wear of polyurethane pads used in glass polishing process. *Precis Eng* 36(4):641–649. <https://doi.org/10.1016/j.precisioneng.2012.05.006>
116. Quinsat Y, Guiot A, Tournier C (2015) Tool wear modelling for constant removal rate in two-bodies automated polishing. *Int J Abras Technol* 7(2):73–89. <https://doi.org/10.1504/IJAT.2015.073803>
117. Zhong B, Chen X, Pan R, Wang J, Huang H, Deng W, Wang Z, Xie R, Liao D (2017) The effect of tool wear on the removal characteristics in high-efficiency bonnet polishing. *Int J Adv Manuf Technol* 91(9):3653–3662. <https://doi.org/10.1007/s00170-017-0015-9>
118. Pan R, Zhong B, Wang Z, Ji S, Chen D, Fan J (2018) Influencing mechanism of the key parameters during bonnet polishing process. *Int J Adv Manuf Technol* 94(1):643–653. <https://doi.org/10.1007/s00170-017-0870-4>
119. Shi C, Peng Y, Hou L, Wang Z, Guo Y (2018) Improved analysis model for material removal mechanisms of bonnet polishing incorporating the pad wear effect. *Appl Opt* 57(25):7172–7186. <https://doi.org/10.1364/AO.57.007172>
120. Zhang Y, Feng J, Zhao Y, Rao M, Yin Y (2023) Towards understanding and restraining the mechanical relaxation effect in polishing silicon carbide with a detachable bonnet tool. *Int J Mech Sci* 246:107962. <https://doi.org/10.1016/j.ijmecsci.2022.107962>
121. Zhong B (2018) Material removal stability of the sub-aperture polishing for large aspheric surface. Dissertation, University of

- Electronic Science and Technology of China, Chengdu, China (In Chinese)
122. Wang Z, Wang Q, Yang X, Chen S, Zhuang X, Peng Y (2017) Dressing scheme and process parameters analysis for bonnet tool in bonnet polishing. *Proc Inst Mech Eng Part C J Mech Eng Sci* 231(19):3569–3578. <https://doi.org/10.1177/0954406216647754>
 123. Kordonski WI, Jacobs SD (1996) Magnetorheological finishing. *Int J Mod Phys B* 10(23–24):2837–2848. <https://doi.org/10.1142/S0217979296001288>
 124. Harris D (2011) History of magnetorheological finishing. *Proc SPIE* 8016:80160N. <https://doi.org/10.1117/12.882557>
 125. Jacobs S, Golini D, Hsu Y, Puchebner B, Strafford D, Kordonski W, Prokhorov I, Fess E, Pietrowski D, Kordonski V (1995) Magnetorheological finishing: a deterministic process for optics manufacturing. *Proc SPIE* 2576:372–382. <https://doi.org/10.1117/12.215617>
 126. Golini D, Kordonski W, Dumas P, Hogan S (1999) Magnetorheological finishing (MRF) in commercial precision optics manufacturing. *Proc SPIE* 3782:80–91. <https://doi.org/10.1117/12.369174>
 127. Jacobs S, Yang F, Fess E, Feingold J, Gillman B, Kordonski W, Edwards H, Golini D (1997) Magnetorheological finishing of IR materials. *Proc SPIE* 3134:258–269. <https://doi.org/10.1117/12.295132>
 128. Arrasmith S, Kozhinova I, Gregg L, Shorey A, Romanofsky H, Jacobs S, Golini D, Kordonski W, Hogan S, Dumas P (1999) Details of the polishing spot in magnetorheological finishing (MRF). *Proc SPIE* 3782:92–100. <https://doi.org/10.1117/12.369175>
 129. Shi F, Qiao S, Deng M, Song C, Tie G, Tian Y, Hao Q, Wang S, Zhou H, Chen J, Sun G, Shen X (2022) Small-scale cluster damage mitigation and detection on fused silica surface. *Infrared Laser Eng* 51(9):20220539. [https://doi.org/10.3788/irla20220539\(InChinese\)](https://doi.org/10.3788/irla20220539(InChinese))
 130. Song C (2012) Study on the key techniques of magnetorheological finishing for off-axis aspheric optical elements. Dissertation, National University of Defense Technology, Changsha, China (In Chinese)
 131. Sato T, Kum CW, Venkatesh VC (2013) Rapid magneto-rheological finishing of Ti-6Al-4V for aerospace components. *Int J Nanomanuf* 9(5–6):431–445. <https://doi.org/10.1504/IJNM.2013.057590>
 132. Ashtiani M, Hashemabadi SH, Ghaffari A (2015) A review on the magnetorheological fluid preparation and stabilization. *J Magn Magn Mater* 374:716–730. <https://doi.org/10.1016/j.jmmm.2014.09.020>
 133. Yadav RD, Singh AK (2019) A novel magnetorheological gear profile finishing with high shape accuracy. *Int J Mach Tools Manuf* 139:75–92. <https://doi.org/10.1016/j.ijmactools.2019.02.001>
 134. Zhang X, Li L, Xue D, Song C, Ai B (2019) Development and application of MRF based on robot arm. *EPJ Web Conf* 215:06001. <https://doi.org/10.1051/epjconf/201921506001>
 135. Li L, Zhang J, Song C, Zhang X, Yin X, Xue D (2019) New generation magnetorheological finishing polishing machines using robot arm. *Proc SPIE* 11341:1134118. <https://doi.org/10.1117/12.2544325>
 136. Guan F, Hu H, Li S, Peng X, Shi F (2018) Analysis of material removal rate and stability in lap-magnetorheological finishing. *Opt Eng* 57(5):055107. <https://doi.org/10.1117/1.OE.57.5.055107>
 137. Pan JS, Yan QS, Lu JB, Xu XP, Chen SK (2014) Cluster magnetorheological effect plane polishing technology. *J Mech Eng* 50(1):205–212. <https://doi.org/10.3901/JME.2014.01.205>. (In Chinese)
 138. Wang YQ, Yin SH, Huang H, Chen FJ, Deng GJ (2015) Magnetorheological polishing using a permanent magnetic yoke with straight air gap for ultra-smooth surface planarization. *Precis Eng* 40:309–317. <https://doi.org/10.1016/j.precisioneng.2014.11.001>
 139. Singh AK, Jha S, Pandey PM (2011) Design and development of nanofinishing process for 3D surfaces using ball end MR finishing tool. *Int J Mach Tools Manuf* 51(2):142–151. <https://doi.org/10.1016/j.ijmactools.2010.10.002>
 140. Zhang J, Chen MJ, Li D, Liu HN, Wang TZ (2017) Magnetorheological polishing method and application of complex structure of thin-walled parts with small diameter permanent magnetic ball. *Aviat Precis Manuf Technol* 53(4):16–19. <https://doi.org/10.3969/j.issn.1003-5451.2017.04.005>. (In Chinese)
 141. Aggarwal A, Singh AK (2023) Magnetorheological finishing of ball-cup surface using new tool to enhance ball-transfer-unit performance. *Mater Manuf Process* 38(10):1226–1242. <https://doi.org/10.1080/10426914.2022.2089889>
 142. Yin SH, Gong S, He BW, Chen FJ, Yin ZQ, Cao CG (2018) Development on synergistic process and machine tools integrated inclined axis grinding and magnetorheological polishing for small aspheric surface. *J Mech Eng* 54(21):205–211. <https://doi.org/10.3901/jme.2018.21.205>. (In Chinese)
 143. Guan F, Hu H, Li S, Liu Z, Peng X, Shi F (2018) A novel Lap-MRF method for large aperture mirrors. *Int J Adv Manuf Technol* 95(9):4645–4657. <https://doi.org/10.1007/s00170-017-1498-0>
 144. Pan J, Yan Q (2015) Material removal mechanism of cluster magnetorheological effect in plane polishing. *Int J Adv Manuf Technol* 81(9):2017–2026. <https://doi.org/10.1007/s00170-015-7332-7>
 145. Luo H, Guo M, Yin S, Chen F, Huang S, Lu A, Guo Y (2018) An atomic-scale and high efficiency finishing method of zirconia ceramics by using magnetorheological finishing. *Appl Surf Sci* 444:569–577. <https://doi.org/10.1016/j.apsusc.2018.03.091>
 146. Singh AK, Jha S, Pandey PM (2012) Nanofinishing of a typical 3D ferromagnetic workpiece using ball end magnetorheological finishing process. *Int J Mach Tools Manuf* 63:21–31. <https://doi.org/10.1016/j.ijmactools.2012.07.002>
 147. Yin SH, Xu ZQ, Chen FJ, Yu JW (2013) Inclined axis magnetorheological finishing technology for small aspherical surface. *J Mech Eng* 49(17):33–38. <https://doi.org/10.3901/jme.2013.17.033>. (In Chinese)
 148. Ren K, Luo X, Zheng L, Bai Y, Li L, Hu H, Zhang X (2014) Belt-MRF for large aperture mirrors. *Opt Express* 22(16):19262–19276. <https://doi.org/10.1364/OE.22.019262>
 149. Ren K (2014) Belt-MRF for large aperture mirrors. Dissertation, Changchun Institute of Optics, Fine Mechanics and Physics, Chinese Academy of Sciences, Changchun, China (In Chinese)
 150. Wang DK (2018) Study on the key technologies of belt magnetorheological finishing. Dissertation, Changchun Institute of Optics, Fine Mechanics and Physics, Chinese Academy of Sciences, Changchun, China (In Chinese)
 151. Das M, Jain VK, Ghoshdastidar PS (2012) Nanofinishing of flat workpieces using rotational-magnetorheological abrasive flow finishing (R-MRAFF) process. *Int J Adv Manuf Technol* 62(1):405–420. <https://doi.org/10.1007/s00170-011-3808-2>
 152. Grover V, Singh AK (2018) Modelling of surface roughness in a new magnetorheological honing process for internal finishing of cylindrical workpieces. *Int J Mech Sci* 144:679–695. <https://doi.org/10.1016/j.ijmecsci.2018.05.058>
 153. Liu J, He J, Peng Y (2023) Development analysis of magnetorheological precession finishing (MRPF) technology. *Opt Express* 31(26):43535–43549. <https://doi.org/10.1364/OE.502933>
 154. Paswan SK, Singh AK (2022) Development of a new in-situ rotating magnetorheological honing technique for fine finishing

- the inner cylindrical surfaces. *Mach Sci Technol* 26(4):665–699. <https://doi.org/10.1080/10910344.2022.2129990>
155. Zhang FH, Wang HJ, Luan DR (2007) Research on machining mechanics and experiment of ultrasonic-magnetorheological compound finishing. *Int J Comput Appl Technol* 29(2–4):252–256. <https://doi.org/10.1504/IJCAT.2007.015275>
 156. Zhang FH, Wang HJ, Liu JF, Luan DR, Zhang Y (2009) Study on the surface quality of optical glass in ultrasonic-magnetorheological compound finishing. *Key Eng Mater* 389–390:181–186. <https://doi.org/10.4028/www.scientific.net/KEM.389-390.181>
 157. Wang HJ (2007) Research on the key technologies of ultrasonic-magnetorheological compound finishing. Dissertation, Harbin Institute of Technology, Harbin, China (In Chinese)
 158. Yu XB (2014) Research on key technologies of figure error correction of ultrasonic-magnetorheological compound finishing. Dissertation, Harbin Institute of Technology, Harbin, China (In Chinese)
 159. Jain VK, Ranjan P, Suri VK, Komanduri R (2010) Chemo-mechanical magneto-rheological finishing (CMMRF) of silicon for microelectronics applications. *CIRP Ann* 59(1):323–328. <https://doi.org/10.1016/j.cirp.2010.03.106>
 160. Ghai V, Ranjan P, Batish A, Singh H (2018) Atomic-level finishing of aluminum alloy by chemo-mechanical magneto-rheological finishing (CMMRF) for optical applications. *J Manuf Process* 32:635–643. <https://doi.org/10.1016/j.jmappro.2018.03.032>
 161. Liang HZ (2019) Study on chemical magnetorheological compound finishing mechanism of single crystal SiC. Dissertation, Guangdong University of Technology, Guangzhou, China (In Chinese)
 162. Tian H, Yan Q, Lu J, Yu J (2007) Foundational study on micro machining with instantaneous tiny grinding wheel based on electro-magneto-rheological effect. *Proc SPIE* 6724:67240P. <https://doi.org/10.1117/12.782682>
 163. Liu Y, Yan QS, Lu JB, Gao WQ, Yang Y (2009) Micro machining of three-dimensional microstructure with the tiny-grinding wheel based on the electro-magneto-rheological effect. *Key Eng Mater* 407–408:363–367. <https://doi.org/10.4028/www.scientific.net/KEM.407-408.363>
 164. Kordonski W, Shorey A, Sekeres A (2003) New magnetically assisted finishing method: material removal with magnetorheological fluid jet. *Proc SPIE* 5180:107–114. <https://doi.org/10.1117/12.506280>
 165. Dai YF, Zhang XC, Li SY, Peng XQ (2009) Deterministic magnetorheological jet polishing technology. *J Mech Eng* 45(5):171–176. <https://doi.org/10.3901/jme.2009.05.171>. (In Chinese)
 166. Zhang XC, Dai YF, Li SY, Peng XQ (2007) Study on magnetorheological jet polishing technology. *Mach Des Manuf* 45(12):114–116. <https://doi.org/10.3969/j.issn.1001-3997.2007.12.048>. (In Chinese)
 167. Wang T, Cheng H, Zhang W, Yang H, Wu W (2016) Restraint of path effect on optical surface in magnetorheological jet polishing. *Appl Opt* 55(4):935–942. <https://doi.org/10.1364/AO.55.000935>
 168. Wang T, Cheng H, Yang H, Wu W, Tam H (2015) Controlling mid-spatial frequency errors in magnetorheological jet polishing with a simple vertical model. *Appl Opt* 54(21):6433–6440. <https://doi.org/10.1364/AO.54.006433>
 169. Sun Z, Fan Z, Tian Y, Qian C, Ma Z (2022) Investigation on magnetorheological shear thickening finishing (MSTF) with radially slotted magnetic pole for free-form surface. *Int J Adv Manuf Technol* 123(9):3313–3327. <https://doi.org/10.1007/s00170-022-10313-0>
 170. Ma Z, Tian Y, Qian C, Ahmad S, Fan Z, Sun Z (2023) Modeling and simulation of material removal characteristics in magnetorheological shear thickening polishing. *Int J Adv Manuf Technol* 128(5):2319–2331. <https://doi.org/10.1007/s00170-023-12093-7>
 171. Jha S, Jain VK (2004) Design and development of the magnetorheological abrasive flow finishing (MRAFF) process. *Int J Mach Tools Manuf* 44(10):1019–1029. <https://doi.org/10.1016/j.ijmactools.2004.03.007>
 172. Wang YQ (2016) Study on magnetorheological finishing using large polishing tool for ultra-smooth flat surface. Dissertation, Hunan University, Changsha, China (In Chinese)
 173. Kinast J, Schlegel R, Kleinbauer K, Steinkopf R, Follert R, Dorn R, Lizon JL, Hatzes A, Tünnermann A (2018) Manufacturing of aluminum mirrors for cryogenic applications. *Proc SPIE* 10706:107063G. <https://doi.org/10.1117/12.2313126>
 174. Beier M, Scheiding S, Gebhardt A, Loose R, Risse S, Eberhardt R, Tünnermann A (2013) Fabrication of high precision metallic freeform mirrors with magnetorheological finishing (MRF). *Proc SPIE* 8884:88840S. <https://doi.org/10.1117/12.2035986>
 175. Institute of Semiconductors, Chinese Academy of Sciences (2018) 4.03 meters of “big eyes”! The world’s largest aperture single silicon carbide reflector successfully developed. http://semi.cas.cn/kxcb/kpwz/201809/t20180906_5065092.html. Accessed 24 February 2024
 176. Liu H, Cheng J, Wang T, Chen M (2019) Magnetorheological finishing of an irregular-shaped small-bore complex component using a small ball-end permanent-magnet polishing head. *Nanotechnol Precis Eng* 2(3):125–129. <https://doi.org/10.1016/j.npe.2019.10.001>
 177. Ji AX, Wang HY, Bi C, Xu AQ (2022) Design of ultrasonic magnetorheological finishing excitation device for medical bone screw. *Opt Precis Eng* 30(18):2219–2231. <https://doi.org/10.37188/ope.20223018.2219>. (In Chinese)
 178. Yan QS, Zhao Y, Liang ZB, Chen JX, Pan JS (2021) Study on cluster magnetorheological finishing of medical titanium alloy with dynamic magnetic fields. *Surf Technol* 50(9):322–332, 378. <https://doi.org/10.16490/j.cnki.issn.1001-3660.2021.09.034>. (In Chinese)
 179. Prakash C, Singh S, Pramanik A, Basak A, Królczyk G, Bogdan-Chudy M, Wu YL, Zheng HY (2021) Experimental investigation into nano-finishing of β -TNTZ alloy using magnetorheological fluid magnetic abrasive finishing process for orthopedic applications. *J Mater Res Technol* 11:600–617. <https://doi.org/10.1016/j.jmrt.2021.01.046>
 180. Arrasmith S, Jacobs S, Lambropoulos J, Maltsev A, Golini D, Kordonski W (2001) Use of magnetorheological finishing (MRF) to relieve residual stress and subsurface damage on lapped semiconductor silicon wafers. *Proc SPIE* 4451:286–294. <https://doi.org/10.1117/12.453627>
 181. Sidpara A, Jain VK (2012) Nano-level finishing of single crystal silicon blank using magnetorheological finishing process. *Tribol Int* 47:159–166. <https://doi.org/10.1016/j.triboint.2011.10.008>
 182. Sun SK, Lu JB, Yan QS (2021) Technological experiment of cluster magnetorheological finishing of InP wafer with dynamic magnetic fields. *Lubr Eng* 46(11):40–45. <https://doi.org/10.3969/j.issn.0254-0150.2021.11.007>. (In Chinese)
 183. Parameswari G, Jain VK, Ramkumar J, Nagdeve L (2019) Experimental investigations into nanofinishing of Ti6Al4V flat disc using magnetorheological finishing process. *Int J Adv Manuf Technol* 100(5):1055–1065. <https://doi.org/10.1007/s00170-017-1191-3>
 184. Shorey AB, Jacobs SD, Kordonski WI, Gans RF (2000) Understanding the mechanism of glass removal in magnetorheological finishing. *LLE Rev* 83:157–172
 185. Schinhaerl M, Smith G, Stamp R, Rascher R, Smith L, Pitschke E, Sperber P, Geiss A (2008) Mathematical modelling of influence functions in computer-controlled polishing: part I. *Appl Math Model* 32(12):2888–2906. <https://doi.org/10.1016/j.apm.2007.10.013>
 186. Song C, Peng XQ, Dai YF, Shi F (2009) Research on process optimization of magnetorheological finishing basing on

- predictive model of removal function. *J Natl Univ Def Technol* 31(4):20–24. <https://doi.org/10.3969/j.issn.1001-2486.2009.04.005>. (In Chinese)
187. Ghosh G, Dalabehera RK, Sidpara A (2019) Parametric study on influence function in magnetorheological finishing of single crystal silicon. *Int J Adv Manuf Technol* 100(5):1043–1054. <https://doi.org/10.1007/s00170-018-2330-1>
 188. Liu S, Wang H, Zhang Q, Hou J, Zhong B, Chen X (2020) Regionalized modeling approach of tool influence function in magnetorheological finishing process for aspherical optics. *Optik* 206:164368. <https://doi.org/10.1016/j.ijleo.2020.164368>
 189. Golini D, Jacobs S, Kordonski W, Dumas P (1997) Precision optics fabrication using magnetorheological finishing. *Proc SPIE* 10289:102890H. <https://doi.org/10.1117/12.279809>
 190. Kordonski W, Golini D, Dumas P, Hogan S, Jacobs S (1998) Magnetorheological-suspension-based finishing technology. *Proc SPIE* 3326:527–535. <https://doi.org/10.1117/12.310670>
 191. Peng XQ, You WW, Shi F (2006) A micro-mechanic-hydrodynamic model for yield stress of magnetorheological fluids. *J Natl Univ Def Technol* 04:110–114. <https://doi.org/10.3969/j.issn.1001-2486.2006.04.023>. (In Chinese)
 192. Schinhaerl M, Rascher R, Stamp R, Smith G, Smith L, Pitschke E, Sperber P (2007) Filter algorithm for influence functions in the computer controlled polishing of high-quality optical lenses. *Int J Mach Tools Manuf* 47(1):107–111. <https://doi.org/10.1016/j.ijmactools.2006.02.005>
 193. Shi F, Dai YF, Peng XQ, Song C (2009) Three-dimensional material removal model of magnetorheological finishing (MRF). *China Mech Eng* 20(6):644–648. <https://doi.org/10.3321/j.issn:1004-132X.2009.06.004>. (In Chinese)
 194. Schinhaerl M, Smith G, Stamp R, Rascher R, Smith L, Pitschke E, Sperber P, Geiss A (2008) Mathematical modelling of influence functions in computer-controlled polishing: part II. *Appl Math Model* 32(12):2907–2924. <https://doi.org/10.1016/j.apm.2007.10.012>
 195. Dai Y, Song C, Peng X, Shi F (2010) Calibration and prediction of removal function in magnetorheological finishing. *Appl Opt* 49(3):298–306. <https://doi.org/10.1364/AO.49.000298>
 196. Liu S, Wang H, Hou J, Zhang Q, Zhong B, Chen X, Zhang M (2022) Morphology characterization of polishing spot and process parameters optimization in magnetorheological finishing. *J Manuf Process* 80:259–272. <https://doi.org/10.1016/j.jmapro.2022.06.008>
 197. Zhang F, Yu JC, Zhang XJ, Tan QC (2001) Analysis of magnetic field used in magnetorheological finishing. *Chin J Sci Instrum* 22(1):42–44, 48. <https://doi.org/10.19650/j.cnki.cjsi.2001.01.012> (In Chinese)
 198. Zheng YC, Wen H, He JG (2015) Influence of circuit structure and material parameters on the magnetic field in magneto-rheological finishing (MRF) area. *J Magn Mater Devices* 46(6):50–53. <https://doi.org/10.3969/j.issn.1001-3830.2015.06.013>. (In Chinese)
 199. Nie M, Cao J, Li J, Fu M (2019) Magnet arrangements in a magnetic field generator for magnetorheological finishing. *Int J Mech Sci* 161–162:105018. <https://doi.org/10.1016/j.ijmecsci.2019.105018>
 200. Lu JB, Bin SM, Yan QS, Huang YL, Xiong Q (2020) Effect of magnetic field distribution on material removal in magnetorheological finishing with multiple polishing heads. *Lubr Eng* 45(4):20–26. <https://doi.org/10.3969/j.issn.0254-0150.2020.04.004>. (In Chinese)
 201. Wang D, Hu H, Li L, Bai Y, Luo X, Xue D, Zhang X (2017) Effects of the gap slope on the distribution of removal rate in Belt-MRF. *Opt Express* 25(22):26600–26614. <https://doi.org/10.1364/OE.25.026600>
 202. Jiang ZQ, Liu P, Fang JH (2018) Research review on magnetorheological fluids. *Synth Lubr* 45(2):27–30. <https://doi.org/10.3969/j.issn.1672-4364.2018.02.010>. (In Chinese)
 203. Bai Y (2015) Preparation of MR polishing fluid and study on the stability of removal function. Dissertation, Changchun Institute of Optics, Fine Mechanics and Physics, Chinese Academy of Sciences, Changchun, China (In Chinese)
 204. Han WJ, Piao SH, Choi HJ, Seo Y (2017) Core-shell structured mesoporous magnetic nanoparticles and their magnetorheological response. *Colloids Surf A Physicochem Eng Asp* 524:79–86. <https://doi.org/10.1016/j.colsurfa.2017.04.016>
 205. Shen ZS, Pan JS, Yan QS (2023) A review of research on the factors influencing the stability of magnetorheological fluids. *J Funct Mater* 54(4):4073–4086. <https://doi.org/10.3969/j.issn.1001-9731.2023.04.010>. (In Chinese)
 206. Kordonski WI, Gorodkin SR, Novikova ZA (1998) The influence of ferroparticle concentration and size on MR fluid properties. In: *Proceedings of the 6th International Conference on Electrorheological Fluids, Magnetorheological Suspensions, and Their Applications*. World Scientific, Singapore, pp 535–542
 207. Guo QY, Wang J, Ouyang Q (2018) Effect of SiO₂ with different specific surface areas on rheological properties and sedimentation stability of magnetorheological fluid. *Mater Mech Eng* 42(10):8–12. <https://doi.org/10.11973/jxgccl201810002>. (In Chinese)
 208. Kordonski WI, Golini D (1999) Fundamentals of magnetorheological fluid utilization in high precision finishing. *J Intell Mater Syst Struct* 10(9):683–689. <https://doi.org/10.1106/011M-CJ25-64QC-F3A6>
 209. López-López MT, Gómez-Ramírez A, Rodríguez-Arco L, Durán JDG, Iskakova L, Zubarev A (2012) Colloids on the frontier of ferrofluids. *Rheological Prop Langmuir* 28(15):6232–6245. <https://doi.org/10.1021/la204112w>
 210. Ginder JM, Davis LC (1994) Shear stresses in magnetorheological fluids: role of magnetic saturation. *Appl Phys Lett* 65(26):3410–3412. <https://doi.org/10.1063/1.112408>
 211. Yang JJ, Yan H, Dai J, Zhang HS (2017) A review on magnetorheological fluid: properties and applications. *Chem Ind Eng Prog* 36(1):247–260. <https://doi.org/10.16085/j.issn.1000-6613.2017.01.031>. (In Chinese)
 212. Li HT, Peng XH, He GT (2010) Research status of mechanism and behavior description of magnetorheological fluids. *Mater Rep* 24(3):121–124 (In Chinese)
 213. Hu H, Dai Y, Peng X, Wang J (2011) Research on reducing the edge effect in magnetorheological finishing. *Appl Opt* 50(9):1220–1226. <https://doi.org/10.1364/AO.50.001220>
 214. Li LX (2016) Study on the key techniques of magnetorheological finishing for large aspheric optics. Dissertation, Changchun Institute of Optics, Fine Mechanics and Physics, Chinese Academy of Sciences, Changchun, China (In Chinese)
 215. Zhong X, Fan B, Wu F (2020) Reducing edge error based on further analyzing the stability of edge TIF and correcting the post-edge algorithm in MRF process. *Opt Rev* 27(1):14–22. <https://doi.org/10.1007/s10043-019-00555-x>
 216. Jeon M, Jeong SK, Kang JG, Yeo WJ, Choi HJ, Lee W (2022) Prediction model for edge effects in magnetorheological finishing based on edge tool influence function. *Int J Precis Eng Manuf* 23(11):1275–1289. <https://doi.org/10.1007/s12541-022-00722-2>
 217. Jia Y (2016) Process algorithms and strategies for mid spatial frequency error control based on magnetorheological polishing. Dissertation, China Academy of Engineering Physics, Mianyang, China (In Chinese)
 218. Yang SF, Chang PY, Yan HS (2012) Rejection of medium-high frequency error in magnetorheological polishing by stochastic

- transverse step method. *Aviat Precis Manuf Technol* 49(2):1–5, 16. <https://doi.org/10.3969/j.issn.1003-5451.2012.02.001>. (In Chinese)
219. Hou J, Chen XH, Liu SW, Zheng N, Zhong B, Deng WH (2020) Effects of magnetorheological processing parameters on the mid-spatial frequency errors of optics. *Proc SPIE* 11427:114272P. <https://doi.org/10.1117/12.2552472>
220. Wan S, Wei C, Hu C, Situ G, Shao Y, Shao J (2021) Novel magic angle-step state and mechanism for restraining the path ripple of magnetorheological finishing. *Int J Mach Tools Manuf* 161:103673. <https://doi.org/10.1016/j.ijmactools.2020.103673>
221. Wang B, Shi F, Tie G, Zhang W, Song C, Tian Y, Shen Y (2022) The cause of ribbon fluctuation in magnetorheological finishing and its influence on surface mid-spatial frequency error. *Micromachines* 13(5):697. <https://doi.org/10.3390/mi13050697>
222. Wang B, Shi F, Zhang W, Tie G, Song C, Guo S (2022) Key technology research on magnetorheological finishing based on suppression of surface mid-spatial frequency ripple errors. *Opt Mater Express* 12(8):3213–3224. <https://doi.org/10.1364/OME.466310>
223. Dai Y, Shi F, Peng X, Li S (2009) Restraint of mid-spatial frequency error in magneto-rheological finishing (MRF) process by maximum entropy method. *Sci China Ser E Technol Sci* 52(10):3092–3097. <https://doi.org/10.1007/s11431-009-0316-9>
224. Yu XB, Zhang FH, Zhang Y, Fu PQ (2010) Planning and Implementation of tool path computer controlled polishing optical surfaces. *Proc SPIE* 7655:765510. <https://doi.org/10.1117/12.867919>
225. Hall C, Jones A, Messner B, Hallock B (2007) Magnetorheological finishing of freeform optics. *Proc SPIE* 10316:103160J. <https://doi.org/10.1117/12.719886>
226. Wang W, Gong R, Ji S, Zhao J, Li X (2024) A mid-high spatial frequency error suppression method based on the pseudo-random path with space MABF mapping for complex surface. *Int J Adv Manuf Technol* 130(5):2443–2456. <https://doi.org/10.1007/s00170-023-12801-3>

Publisher's Note Springer Nature remains neutral with regard to jurisdictional claims in published maps and institutional affiliations.

Springer Nature or its licensor (e.g. a society or other partner) holds exclusive rights to this article under a publishing agreement with the author(s) or other rightsholder(s); author self-archiving of the accepted manuscript version of this article is solely governed by the terms of such publishing agreement and applicable law.